

SPIE. FIELD
GUIDE

Field Guide to

Displacement Measuring Interferometry

Jonathan D. Ellis

SPIE Terms of Use: This SPIE eBook is DRM-free for your convenience. You may install this eBook on any device you own, but not post it publicly or transmit it to others. SPIE eBooks are for personal use only. For details, see the SPIE [Terms of Use](#). To order a print version, [visit SPIE](#).

SPIE.

Field Guide to

Displacement Measuring Interferometry

Jonathan D. Ellis

SPIE Field Guides
Volume FG30

John E. Greivenkamp, Series Editor

SPIE PRESS
Bellingham, Washington USA

Library of Congress Cataloging-in-Publication Data

Ellis, Jonathan D. (Jonathan David)

Field guide to displacement measuring interferometry /
Jonathan D. Ellis.

pages cm. – (The field guide series)

Includes bibliographical references and index.

ISBN 978-0-8194-9799-4 (print : alk. paper) –

ISBN 978-0-8194-9800-7 (ebook : alk. paper) –

ISBN (invalid) 978-0-8194-9801-4 (epub : alk. paper)

1. Interferometry. 2. Optical measurements. I. Title.

II. Title: Displacement measuring interferometry.

QC415.E45 2014

535/.470287–dc23

2013030249

Published by

SPIE

P.O. Box 10

Bellingham, Washington 98227-0010 USA

Phone: +360.676.3290

Fax: +360.647.1445

Email: books@spie.org

www.spie.org

Copyright © 2014 Society of Photo-Optical Instrumentation
Engineers (SPIE)

All rights reserved. No part of this publication may be
reproduced or distributed in any form or by any means
without written permission of the publisher.

The content of this book reflects the thought of the author(s).
Every effort has been made to publish reliable and accurate
information herein, but the publisher is not responsible for
the validity of the information or for any outcomes resulting
from reliance thereon.

Printed in the United States of America.

First printing

Introduction to the Series

Welcome to the *SPIE Field Guides*—a series of publications written directly for the practicing engineer or scientist. Many textbooks and professional reference books cover optical principles and techniques in depth. The aim of the *SPIE Field Guides* is to distill this information, providing readers with a handy desk or briefcase reference that provides basic, essential information about optical principles, techniques, or phenomena, including definitions and descriptions, key equations, illustrations, application examples, design considerations, and additional resources. A significant effort will be made to provide a consistent notation and style between volumes in the series.

Each *SPIE Field Guide* addresses a major field of optical science and technology. The concept of these *Field Guides* is a format-intensive presentation based on figures and equations supplemented by concise explanations. In most cases, this modular approach places a single topic on a page, and provides full coverage of that topic on that page. Highlights, insights, and rules of thumb are displayed in sidebars to the main text. The appendices at the end of each *Field Guide* provide additional information such as related material outside the main scope of the volume, key mathematical relationships, and alternative methods. While complete in their coverage, the concise presentation may not be appropriate for those new to the field.

The *SPIE Field Guides* are intended to be living documents. The modular page-based presentation format allows them to be updated and expanded. We are interested in your suggestions for new *Field Guide* topics as well as what material should be added to an individual volume to make these *Field Guides* more useful to you. Please contact us at fieldguides@SPIE.org.

John E. Greivenkamp, *Series Editor*
College of Optical Sciences
The University of Arizona

The Field Guide Series

Keep information at your fingertips with all of the titles in the *Field Guide* Series:

- Adaptive Optics*, Second Edition, Robert Tyson & Benjamin Frazier
- Atmospheric Optics*, Larry Andrews
- Binoculars and Scopes*, Paul Yoder, Jr. & Daniel Vukobratovich
- Diffraction Optics*, Yakov Soskind
- Displacement Measuring Interferometry*, Jonathan D. Ellis
- Geometrical Optics*, John Greivenkamp
- Illumination*, Angelo Arecchi, Tahar Messadi, & John Koshel
- Image Processing*, Khan M. Iftekharruddin & Abdul Awwal
- Infrared Systems, Detectors, and FPAs*, Second Edition, Arnold Daniels
- Interferometric Optical Testing*, Eric Goodwin & Jim Wyant
- Laser Pulse Generation*, Rüdiger Paschotta
- Lasers*, Rüdiger Paschotta
- Lens Design*, Julie Bentley & Craig Olson
- Microscopy*, Tomasz Tkaczyk
- Nonlinear Optics*, Peter Powers
- Optical Fabrication*, Ray Williamson
- Optical Fiber Technology*, Rüdiger Paschotta
- Optical Lithography*, Chris Mack
- Optical Thin Films*, Ronald Willey
- Optomechanical Design and Analysis*, Katie Schwertz & James Burge
- Physical Optics*, Daniel Smith
- Polarization*, Edward Collett
- Probability, Random Processes, and Random Data Analysis*, Larry Andrews
- Radiometry*, Barbara Grant
- Special Functions for Engineers*, Larry Andrews
- Spectroscopy*, David Ball
- Terahertz Sources, Detectors, and Optics*, Créidhe O'Sullivan & J. Anthony Murphy
- Visual and Ophthalmic Optics*, Jim Schwiegerling

Introduction

This *Field Guide to Displacement Measuring Interferometry* delves into a subfield of optical metrology that is prevalent in many precision systems. Precision systems that require accurate positioning knowledge use displacement measuring interferometry either through direct measurement or calibration of alternative metrology systems. Displacement measuring interferometry offers high-accuracy measurements with a wide bandwidth and direct traceability to international length standards.

The aim of this *Field Guide* is to provide a practical treatment of the fundamental theory of displacement interferometry along with examples of interferometry systems and uses, to outline alignment techniques for optical components, and to discuss measurement uncertainty with a practical example.

For practicing engineers, this will serve as a refresher manual for error sources and uncertainty budgets. For researchers, this will hopefully bring new insight to ways in which this technology can be useful in their field. For new engineers, researchers, and students, this *Field Guide* will serve as an introduction to basic alignment techniques for breadboard-based optical systems.

I would like to thank Vivek Badami for his helpful insight and for being a great mentor and friend. I am grateful for a thorough review of this manuscript by Steven Gillmer. I am indebted to many professors for training me in precision engineering and metrology, especially Stuart T. Smith, Robert J. Hocken, and the other faculty members of the Center for Precision Metrology at UNC Charlotte.

This *Field Guide* is dedicated to Kate Medicus for reducing my uncertainty budget in life.

Jonathan D. Ellis

*Institute of Optics
University of Rochester*

Table of Contents

Glossary of Terms and Acronyms	xi
Fundamentals of Light and Interference	1
Basic Assumptions	1
Degrees of Freedom	2
The Meter	3
Electromagnetic Radiation	4
Electric Field	5
Polarization States	6
Complex Polarization	7
Superposition	8
Interference	9
Irradiance	10
Polarization Overlap	11
Fringe Contrast	12
Interferometer Components and Notation	13
More Interferometer Components	14
Polarization-Based Components	15
Waveplates	16
Ghosts, Absorption, and Scatter	17
Michelson's Interferometer	18
Temporal Coherence	19
Displacement from Phase Change	20
Unwrapping and Folding	21
Basic Interferometry Systems	22
Interferometry Systems	22
Homodyne Interferometer	23
Retroreflector Homodyne Interferometer	24
Homodyne Optical Power Efficiency	25
Polarization-Sensitive Homodyne Interferometer	26
Directional Sensitivity	27
Direction-Sensitive Homodyne Interferometer	28
Homodyne Laser Encoder	29
Heterodyne Interferometry Systems	30
Basic Heterodyne Interferometer	31
Heterodyne Directional Sensitivity	32
Homodyne and Heterodyne Comparison	33

Table of Contents

Interferometry System Characteristics	35
Unequal Plane Mirror Interferometer	35
Plane Mirror Interferometer (PMI)	36
PMI Variants	37
Beam Walkoff	38
Doppler Velocity	39
Dynamic Range and Acceleration Limitations	40
Laser Sources	41
Optical Power and Laser Modes	42
Zeeman-Stabilized Laser	43
Two-Mode Intensity-Balanced Laser	44
Heterodyne Frequency Generation	45
Phase Measurements	46
Interference Detection	47
Detection Bandwidth	48
Phase Quadrature Measurements	49
Time Interval Analysis	50
Lock-In Detection	51
Discrete Fourier Transform	52
 Special Interferometer Configurations	 53
Special Interferometer Configurations	53
Quad-Pass Interferometer	54
Differential Interferometer	55
Coaxial Differential Interferometer	56
Angle Interferometer	57
Straightness Interferometer	58
Refractometry	59
Wavelength Tracking	60
Refractive Index Tracker	61
Multiaxis Systems	62
Multi-DOF Interferometers	63
X-Y-Theta System	64
Tip-Tilt-Z System	65
 Interferometer Alignment	 66
Setup and Alignment Techniques	66
Commercial Interferometer Alignment	67
Vector Alignment and Breadboard Alignment	68

Table of Contents

Beam Fly Height	69
Grid Alignment	70
Normal Mirror Alignment	71
45-deg Mirror Alignment	72
Mirror Steering	73
Beamsplitter Alignment	74
Polarizer Alignment	75
45-deg HWP Alignment	76
45-deg QWP Alignment	77
Polarization Flipping	78
In-line Beam Steering	79
Cosine Error	80
Cosine Mirror Alignment	81
Mixing and Periodic Error	82
Lissajous Figure	82
Source Mixing	83
Beam Leakage	84
Periodic Error	85
Assessing Periodic Error	86
Quantifying Periodic Error	87
Spatial Fourier Analysis	88
Measurement Errors and Uncertainty	89
Measurement Uncertainty	89
Probability Distributions	90
Combined Uncertainty	91
Uncertainty Sources	92
DMI Measurement Model	93
Source Vacuum Wavelength	94
Refractive Index Uncertainty	95
Cosine Error: Retroreflector Target	96
Cosine Error: Plane Mirror Target	97
Phase Change Uncertainty	98
Abbé Uncertainty	99
Measurement Axis Location	100
Interferometer Thermal Drift	101
Deadpath Uncertainty	102
Periodic Error Uncertainty	103

Table of Contents

Surface Figure Error	104
Data Age Uncertainty	105
Error Corrections	106
Air Refractive Index Compensation	107
Error Budget	108
Measurement Uncertainty Example	109
Stage Measurement Uncertainty Example	109
Example Uncertainty Parameters	110
Example Uncertainty Propagation	111
Example Combined Uncertainty	115
Equation Summary	116
Bibliography	125
Index	129

Glossary of Terms and Acronyms

$^{\circ}\text{C}$	degrees Celsius
%RH	percent relative humidity
A	amps
A_1	first-order periodic error amplitude
A_2	second-order periodic error amplitude
A_D	photodetector area
ADC	analog-to-digital conversion/converter
AOM	acousto-optic modulator
BS	beamsplitter
c	speed of light
C	capacitance
CCD	charged-coupled device [camera]
CLK	clock
CO_2	carbon dioxide
CSY	a coordinate system
C_T	thermal drift coefficient
CTE	coefficient of thermal expansion
d	displacement interferometer output estimate
d_A	Abbé offset
$d_{A,x}$	Abbé offset along X axis
$d_{A,y}$	Abbé offset along Y axis
dB	decibels
DC	direct current
deg	degree (angle)
DFT	discrete Fourier transform
d_i	displacement error contribution
DMI	displacement measuring interferometry/ interferometer
DOF	degree of freedom
d_{SF}	surface figure error
DSP	digital signal processor
d_{TD}	thermal drift error
d_{ψ}	cosine error
E	electric field vector
E_0	electric field amplitude
E_1	electric field of beam 1
E_2	electric field of beam 2
e_A	Abbé offset error

Glossary

E_{net}	net electric field of two-beam interference
f	optical frequency
F	farads
f_0	optical frequency of iodine-stabilized laser
f_1	first optical frequency
f_2	second optical frequency
f_{clk}	DFT clock frequency
f_{D}	Doppler frequency shift
FPGA	field-programmable gate array
f_{s}	heterodyne (split) frequency (or frequency difference)
FSR	free spectral range
G	transimpedance amplifier gain
GHz	gigahertz (10^9 Hz)
H	humidity
HeNe	helium-neon laser
HPF	high-pass filter
HWP	half waveplate
Hz	hertz
i	complex number ($= \sqrt{-1}$)
i	incident beam direction
I_{amp}	amplitude of the interference signal
I_{D}	detected irradiance
I_{FC}	interference fringe contrast
I_{i}	input irradiance
I_{m}	measurement irradiance
I_{max}	maximum interference signal
I_{mean}	average interference signal
I_{min}	minimum interference signal
I_{o}	output irradiance
i-V	current-to-voltage amplifier
k	uncertainty coverage factor
K	Kelvin
K_{H}	air refractive index sensitivity from humidity
km	kilometer (10^3 m)
K_{P}	air refractive index sensitivity from pressure
K_{T}	air refractive index sensitivity from temperature
l_{c}	laser cavity length
L_{c}	long coherence length

Glossary

L_D	distance between interferometers
LHC	left-hand circular (polarization)
L_{offset}	offset length for cosine error
LPF	low-pass filter
L_{range}	target displacement range
L_{RR}	length between retroreflectors for angle optics
LSB	least significant bit
m	meters
m	number of observations
M	1D or 2D cosine uncertainty parameter
MHz	megahertz
mm	millimeters (10^{-3} m)
mrاد	milliradians (10^{-3} rad)
n	refractive index
N	interferometer fold constant
N	mirror normal
n_{air}	air refractive index
n_f	final refractive index (during a measurement)
n_i	initial refractive index (during a measurement)
n_i	refractive index of medium i
NIST	National Institute of Standards and Technology
nm	nanometers (10^{-9} m)
n_o	refractive index of medium o
nrad	nanoradians (10^{-9} rad)
n_{RR}	retroreflector refractive index
ns	nanoseconds (10^{-9} s)
nW	nanowatts (10^{-9} W)
OPD	optical path difference
OPL	optical path length
O_{pmi}	PMI axis offset
P	optical power
P	pressure
Pa	Pascals
PBS	polarizing beamsplitter
PD	photodiode
PD_m	measurement photodiode
PD_r	reference photodiode
PLL	phase-locked loop
pm	picometers (10^{-12} m)

Glossary

PMI	plane mirror interferometer
PSD	position-sensitive detector
QWP	quarter waveplate
R	resistance
r_1	amplitude of beam 1
r_2	amplitude of beam 2
rad	radians
RH	relative humidity
RHC	right-hand circular (polarization)
r_{net}	amplitude of two-beam interference
RR	retroreflector
RR_h	retroreflector height
s	seconds
t	time
T	temperature
THz	terahertz (10^{12} Hz)
TIR	total internal reflection
U	expanded uncertainty
$u(A_1)$	uncertainty in first-order periodic error
$u(A_2)$	uncertainty in second-second periodic error
$u(C_T)$	uncertainty in thermal drift
$u(d_A)$	uncertainty in Abbé offset
$u(d_{A,x})$	uncertainty in Abbé offset along X axis
$u(d_{A,y})$	uncertainty in Abbé offset along Y axis
$u(d_{\text{SF}})$	uncertainty in surface figure
$u(H)$	uncertainty in relative humidity
$u(n)$	uncertainty in refractive index
$u(n_{\text{air}})$	uncertainty in air refractive index
$u(P)$	uncertainty in pressure
$u(T)$	uncertainty in temperature
$u(x_i)$	uncertainty in input estimates
$u(z_{\text{DP}})$	uncertainty in deadpath distance
$u(\alpha_A)$	uncertainty in Abbé angle
$u(\alpha_{\text{cosine}})$	uncertainty in cosine angle
$u(\alpha_N)$	uncertainty in beam normality angle
$u(\Delta n/n_f)$	uncertainty in fractional refractive index change
$u(\Delta\theta)$	uncertainty in phase change
$u(\Delta\lambda/\lambda_i)$	uncertainty in fractional wavelength change
$u(\lambda)$	uncertainty in wavelength

Glossary

$u(\lambda_{\text{nom}})$	uncertainty in nominal wavelength
$u(\lambda_{\text{stab}})$	uncertainty in wavelength stability
$u(\tau_{\text{DA}})$	uncertainty in data age
$u(\varphi_x)$	uncertainty in target angle error about X axis
$u(\varphi_y)$	uncertainty in target angle error about Y axis
$u(\psi)$	uncertainty in cosine error
$u_{\text{A}}(d)$	displacement uncertainty from Abbé errors
$u_{\text{c}}(d)$	combined displacement uncertainty
$u_{\text{DA}}(d)$	displacement uncertainty from data age
$u_{\text{DP}}(d)$	displacement uncertainty from deadpath errors
u_{Edlen}	uncertainty in the Edlén equation
u_i	standard uncertainty
$u_{\text{n}}(d)$	displacement uncertainty from refractive index
$u_{\text{PE}}(d)$	displacement uncertainty from periodic error
$u_{\text{SF}}(d)$	displacement uncertainty from surface figure
$u_{\text{TD}}(d)$	displacement uncertainty from thermal drift
$u_{\Delta\theta}(d)$	displacement uncertainty from phase change
$u_{\lambda}(d)$	displacement uncertainty from wavelength
$u_{\psi}(d)$	displacement uncertainty from cosine error
V	volts
V_i	interference signal converted to volts
W	watts
y	output estimate
Y	measurand
z	actual displacement
\mathbf{z}	direction of target motion
ZCD	zero-crossing detector
z_{DP}	deadpath distance
$z_{\text{i,m}}$	initial measurement arm length
$z_{\text{i,r}}$	initial reference arm length
z_{m}	measured displacement
z_{o}	optical path length
z_{p}	physical path length
α_{A}	Abbé angle
α_{cosine}	angle between target and interferometer axes
α_{N}	target normal beam angle
α_{p}	polarizer angle
α_{s}	Wollaston prism angle

Glossary

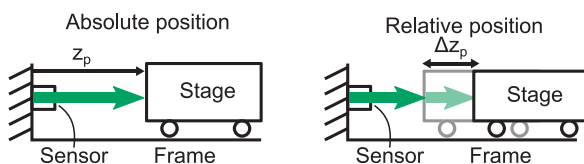
α_{σ}	probability distribution half-width
$\alpha_{\sigma,H}$	humidity probability distribution half-width
$\alpha_{\sigma,P}$	pressure probability distribution half-width
$\alpha_{\sigma,T}$	temperature probability distribution half-width
β	Bragg angle
γ_1	first-order mixing amplitude
γ_2	second-order mixing amplitude
Γ_1	interference signal Fourier magnitude
Γ_2	first-order mixing Fourier magnitude
Γ_3	second-order mixing Fourier magnitude
ΔH	change in humidity
ΔI_f	change in optical power between laser modes
Δl_c	change in laser cavity length
Δn	change in refractive index
ΔP	change in pressure
ΔR_{φ}	walkoff between beams
ΔT	change in temperature
Δx	straightness error in X direction
Δy	straightness error in Y direction
$\Delta \theta$	change in phase
$\Delta \lambda$	change in wavelength
$\Delta \lambda_{\text{stab}}$	change in wavelength from stability
$\Delta \varphi$	change in target angle
$\Delta \varphi_x$	change in target angle about X axis pitch (along path)
$\Delta \varphi_y$	change in target angle about Y axis yaw (along path)
$\Delta \varphi_z$	roll (along path)
ϵ_0	vacuum permittivity
ϵ_{medium}	permittivity of propagation medium
ϵ_r	relative permittivity
η_{633}	silicon responsivity at 633 nm
θ_1	phase of beam 1
θ_2	phase of beam 2
θ_m	measured phase
θ_m	phase of the reference beam
θ_{net}	phase of two-beam interference
λ	wavelength
λ_0	wavelength of iodine laser

Glossary

λ_f	final wavelength (during a measurement)
λ_i	initial wavelength (during a measurement)
λ_{nom}	nominal wavelength
λ_{stab}	wavelength stability
μ_0	vacuum permeability
μm	micrometers (10^{-6} m)
μ_{medium}	permeability of propagation medium
μ_r	relative permeability
μrad	microradians (10^{-6} rad)
μs	microseconds (10^{-6} s)
μW	microwatts (10^{-6} W)
v	velocity of light
v	target velocity
v_D	Doppler velocity
v_o	voltage output
τ_{DA}	measurement data age
φ	target angle
φ_x	target angle error about X axis
φ_y	target angle error about Y axis
φ_z	target angle error about Z axis
ψ	displacement scale error
ψ_i	angle of incidence from medium i
ψ_o	angle of refraction into medium o
ω	optical frequency in angular units

Basic Assumptions

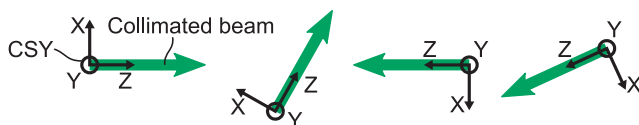
Displacement measuring interferometry is widely used for measuring the position change of a target object. As the name suggests, displacement measuring interferometry is only used to measure the **relative position** of a target as opposed to the **absolute position**.



Displacement measuring interferometers (DMIs) use the principle of **interference** between two optical beams to measure the relative position of a target. One beam, designated the **reference arm**, travels in a nominally fixed path in the interferometer. The other beam, the **measurement arm**, travels in a path that reflects off of the moving target or object to be measured. Eventually, these two beams are guided to overlap and interfere. Detection and subsequent signal processing is then used to determine the target displacement.

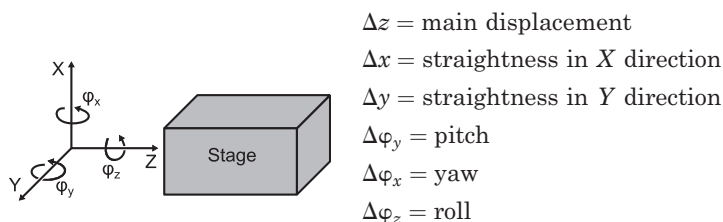
The following conventions are used throughout this *Field Guide*:

- Optical beams are considered to be perfectly collimated.
- The Z axis is always coaxial with the instantaneous, nominal **optical path** in the direction of propagation.
- The optical coordinate system (CSY) is Cartesian and follows the optical path using the right-hand rule.
- The X axis is orthogonal to the Z axis and resides in the plane of the page (based on the instantaneous optical path).
- The Y axis is orthogonal to both the X and Z axes and is normal to the surface of the page (also based on the instantaneous optical path).



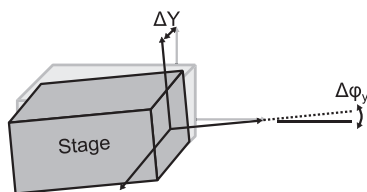
Degrees of Freedom

DMIs are typically used for measuring a single linear **degree of freedom** (DOF). Each body can move in six DOFs, three translational and three rotational, unless constrained. Suppose that a stage were to have straight, rotation-free motion in the Z direction. Then, motions in the unwanted directions can cause an error in the position of the stage/target. The two linear error motions in the X and Y directions are called **straightness errors** (or **straightness** for short). The three rotational errors are called **roll**, **pitch**, and **yaw** and result from motions about the Z , Y , and X axes, respectively.



For a target object moving in the Z direction, this *Field Guide* will assume pure linear motion unless otherwise stated.

Error motions such as straightness, pitch, and yaw can be measured using displacement interferometry systems with specific interferometer and target configurations. This enables error



correction for precision positioning systems for, e.g., machine tools and coordinate measuring machines. Configurations to measure these errors will be discussed in Special Interferometer Configurations (p. 65), and the influence of these errors will be discussed in Uncertainty Sources (p. 104).

The Meter

The **meter** is defined as the path length of light in vacuum traveled collinearly with the propagation direction in $1/299,792,458^{\text{th}}$ of a second. This cannot be directly observed; thus, a **practical standard** is used to realize the meter.

The meter can be realized at a 633-nm wavelength using a helium-neon (HeNe) laser stabilized on the R(127) 11-5 hyperfine absorption line of an $^{127}\text{I}_2$ absorption cell. A nominal 633-nm wavelength is used for most traditional DMI applications.

Iodine-stabilized laser properties include:

Optical frequency: $f_0 = 473,612,353,604 (10) \text{ kHz}$

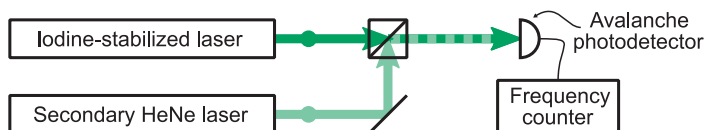
Vacuum wavelength: $\lambda_0 = 632,991,212,579 (13) \text{ fm}$

Fractional uncertainty: $u(f_0)/f_0 = 2.1 \times 10^{-11}$

Typical output power: $P_0 \cong 100 \mu\text{W}$

Iodine-stabilized lasers typically have a frequency modulation of $\pm 3 \text{ MHz}$ and are highly susceptible to **optical feedback destabilization**, limiting their direct application for DMI.

Traceability is established for DMI lasers through a **traceability chain** by measuring the interference beat frequency between an iodine-stabilized laser (or other reference laser) and the secondary laser.



An avalanche photodiode and frequency counter are used to detect and track the interference frequency with gigahertz bandwidth. The absolute frequency of the DMI laser can be determined from the known frequency of the iodine-stabilized laser and the measured frequency difference.

Electromagnetic Radiation

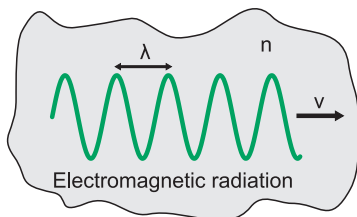
Visible light is a part of the **electromagnetic radiation** spectrum that can be seen by the human eye. The color observed is representative of the energy associated with the radiation. Red light contains the lowest energy in the spectrum and corresponds to a maximum wavelength of ~ 750 nm, which is ~ 400 THz. Violet light is on the opposite end of the spectrum and has a minimum wavelength of ~ 380 nm (or ~ 770 THz). Light travels at a constant, defined speed in vacuum. When light propagates in any other medium, its velocity v is reduced by the **refractive index** of the propagation medium.

Speed of light c :

$$c \doteq 299,792,458 \text{ [m} \cdot \text{s}^{-1}\text{]}$$

Refractive index n :

$$n = \frac{c}{v}$$



The **vacuum wavelength** λ and frequency f of light are related by the propagation velocity:

$$f = \frac{c}{n\lambda} = \frac{v}{\lambda}$$

Vacuum permeability: $\mu_0 \doteq 4\pi \times 10^{-7} \text{ [V} \cdot \text{s} \cdot \text{A}^{-1} \cdot \text{m}^{-1}\text{]}$

Vacuum permittivity: $\epsilon_0 \cong 8.854 \times 10^{-12} \text{ [A}^2 \cdot \text{s}^4 \cdot \text{kg}^{-1} \cdot \text{m}^{-3}\text{]}$

The speed of light, refractive index, permeability, and permittivity are all related for the propagation medium:

Vacuum

$$c = \frac{1}{\sqrt{\epsilon_0 \mu_0}}$$

$$\epsilon_0 \doteq \frac{1}{\mu_0 c^2}$$

$$n \doteq 1$$

Nonvacuum

$$n = \sqrt{\epsilon_r \mu_r} \quad v = \frac{c}{n} = \frac{c}{\sqrt{\epsilon_r \mu_r}}$$

$$\mu_r = \frac{\mu_{\text{medium}}}{\mu_0} \quad \epsilon_r = \frac{\epsilon_{\text{medium}}}{\epsilon_0}$$

Electric Field

Laser light is a transverse electromagnetic wave, where the oscillation is perpendicular to the propagation direction. The **electric field vector** \mathbf{E} is typically represented with complex notation:

$$\mathbf{E} = E_0 e^{i2\pi\left(ft \pm \frac{\mathbf{z}_p n}{\lambda}\right)} = E_0 e^{i[\omega t \pm \varphi(\mathbf{z}_p)]}$$

$$E_0 = \sqrt{\frac{2P_0}{\epsilon v A}}$$

$$\omega = 2\pi f$$

$$\varphi(\mathbf{z}_p) = \frac{2\pi \mathbf{z}_p n}{\lambda}$$

P_0 is optical power of the beam.

A is area of the beam.

ω is the optical angular frequency.

f is the optical frequency (in hertz).

\mathbf{z}_p is physical path length traveled.

n is the refractive index along the path.

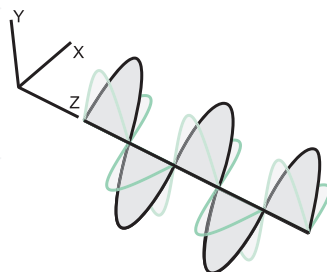
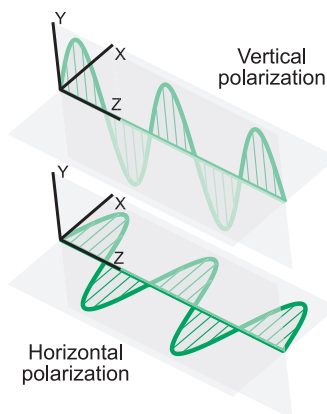
λ is the vacuum wavelength of light.

The transverse electromagnetic wave oscillates at the radiation frequency in angular units, and the instantaneous phase is proportional to the distance traveled along the optical path.

The transverse direction of the electric field specifies the **polarization state**. Conventionally, light is assumed to be polarized along the X or Y axes, or some combination of both.

$$\mathbf{E} = E_0 e^{i(\omega t \pm \varphi)} (\tilde{x}_i \hat{\mathbf{i}} + \tilde{y}_i \hat{\mathbf{j}})$$

\tilde{x}_i and \tilde{y}_i are the polarization states and are generally complex. When \tilde{x}_i and \tilde{y}_i are not complex, the polarization state is linear at an arbitrary axis.



Polarization States

There are two independent, orthogonal linear **polarization states** for a beam of light propagating along the Z axis. For convenience, the **azimuthal** direction is oriented to assume that the orthogonal polarization states coincide with the X and Y axes.

Knowing the polarization states is critical for DMI because two overlapping beams with orthogonally polarized states do not interfere. Ultimately, measurement cannot occur without interference.

$\mathbf{E} = E_0 e^{i(\omega t \pm \varphi)} (\tilde{x}_i \mathbf{i} + \tilde{y}_i \mathbf{j})$ The electric field vector, including polarization states, can be written in matrix form using so-called **Jones matrices** to specify the polarization orientation. Jones matrices are used to follow the amplitude and phase of the electric field vectors in a system to specify the polarization state.

Single beam:

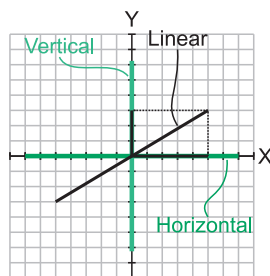
$$\mathbf{E} = E_0 e^{i(\omega t \pm \varphi)} \begin{bmatrix} \tilde{x}_i \\ \tilde{y}_i \end{bmatrix}$$

General form:

$$\mathbf{E} = \begin{bmatrix} E_{01} e^{i(\omega_1 t \pm \varphi_1)} \tilde{x}_i \\ E_{02} e^{i(\omega_2 t \pm \varphi_2)} \tilde{y}_i \end{bmatrix}$$

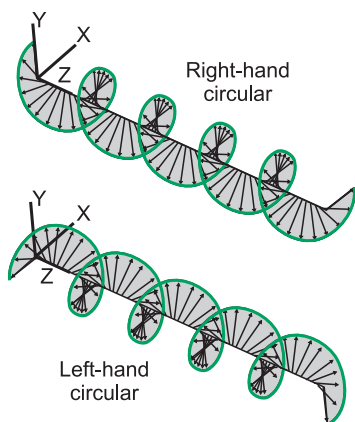
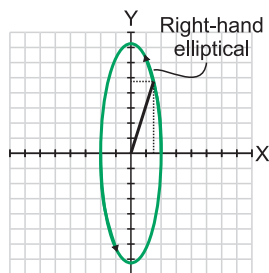
The polarization state of an optical beam can be represented on a **polarization diagram**, which is used to convert polarization states specified in one orientation to another orientation about the azimuthal direction.

The vertical and horizontal polarization states are the primary polarization states of an interferometer. Linearly polarized light contains parts of both vertically and horizontally polarized light. When the polarization is complex, the polarization is elliptical.



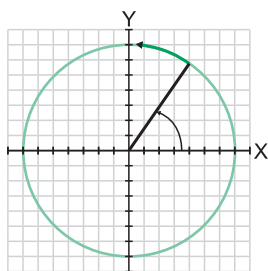
Complex Polarization

Complex polarization coefficients describe an elliptical polarization state. When a beam's polarization is elliptical, the polarization rotates between vertical and horizontal polarization states. A specific (and common) case is when the beam has equal amplitudes between vertical and horizontal polarization states with a 90-deg phase lag. This is called **circular polarization**. There are two orthogonal circular polarization states, **right-hand circular** (RHC) and **left-hand circular** (LHC). In these instances, the difference between \tilde{x}_i and \tilde{y}_i is i , and its sign determines whether it is right- or left-hand circularly polarized.

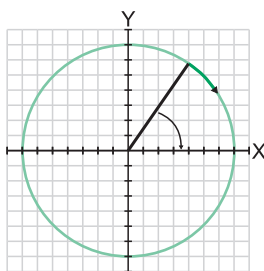


$$\mathbf{E}_{\text{RHC}} = \frac{E_0 e^{i(\omega t \pm \varphi)}}{\sqrt{2}} \begin{bmatrix} 1 \\ -i \end{bmatrix}$$

$$\mathbf{E}_{\text{LHC}} = \frac{E_0 e^{i(\omega t \pm \varphi)}}{\sqrt{2}} \begin{bmatrix} 1 \\ i \end{bmatrix}$$



Right-hand circular

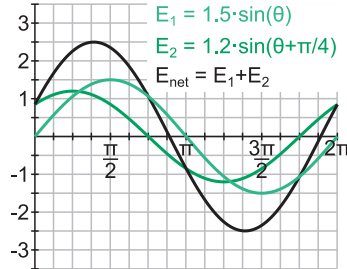


Left-hand circular

Superposition

Optical **interference** is determined by the net electric field as seen by a photodetector. The net electric field is determined by the **superposition principle**.

This *Field Guide* assumes that light behaves as a classical wave. Thus, the net electric field from two overlapping waves of light with the same polarization state is the algebraic sum of each individual electric field wave.



Electric fields are expressed in **complex notation**, where $i = \sqrt{-1}$, and a complex number comprises real and imaginary parts: $\tilde{z} = x + iy$.

In **polar coordinates** (r, θ) ,

$$x = r \cos(\theta) \quad y = r \sin(\theta) \quad \tilde{z} = r [\cos(\theta) + i \sin(\theta)] = r e^{i\theta}$$

$$\tilde{z}^* = r e^{-i\theta}$$

$$r = |\tilde{z}| = \sqrt{\tilde{z} \tilde{z}^*} = \sqrt{x^2 + y^2}$$

Euler's formula is

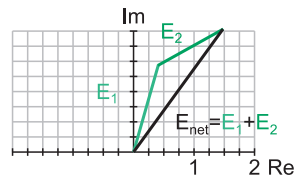
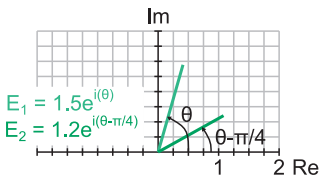
$$e^{i\theta} = \cos(\theta) + i \sin(\theta)$$

$$\cos(\theta) = \frac{e^{i\theta} + e^{-i\theta}}{2}$$

$$e^{-i\theta} = \cos(\theta) - i \sin(\theta)$$

$$\sin(\theta) = \frac{e^{i\theta} - e^{-i\theta}}{2i}$$

Superposition in polar form using complex notation can be visualized using a **phasor diagram**.



Interference

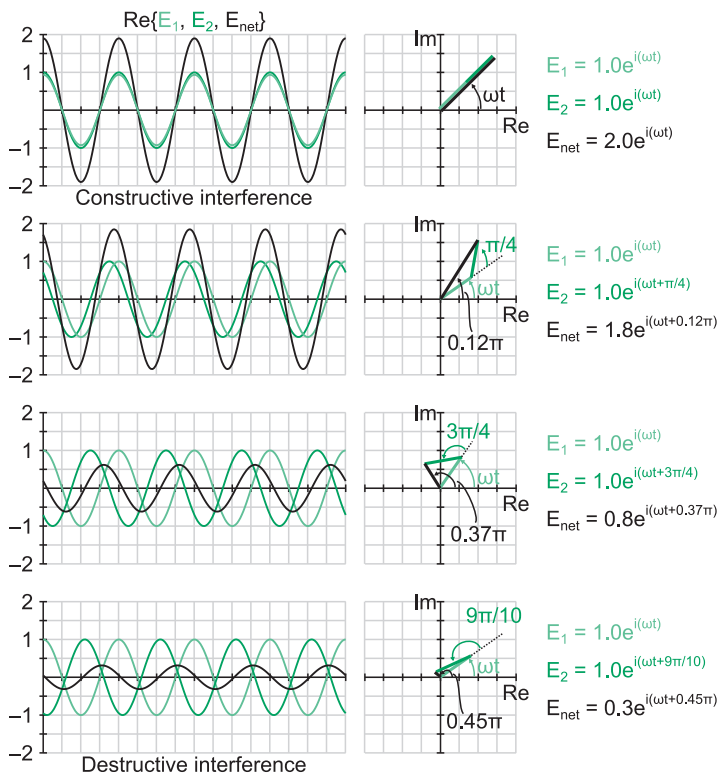
Interference between two optical beams enables displacement measuring interferometry signals to be detected. When the two beams are in phase, the net electric field created by the optical beams generates **constructive interference**. As the two beams shift out of phase with respect to each other, the net electric field is reduced. When the two beams are 180 deg out of phase, no electric field is generated due to **destructive interference**.

$$E_{\text{net}} = r_{\text{net}} e^{i(\omega t + \theta_{\text{net}})}$$

$$E_1 = r_1 e^{i(\omega t + \theta_1)}$$

$$E_2 = r_2 e^{i(\omega t + \theta_2)} \rightarrow r_{\text{net}}^2 = (r_1 \cos \theta_1 + r_2 \cos \theta_2)^2 + (r_1 \sin \theta_1 + r_2 \sin \theta_2)^2$$

$$\theta_{\text{net}} = \arctan \left(\frac{r_1 \sin \theta_1 + r_2 \sin \theta_2}{r_1 \cos \theta_1 + r_2 \cos \theta_2} \right)$$



Irradiance

Interference is detected by measuring the total **irradiance** of the electric fields integrated over the photodetector area A_D . The irradiance I is proportional to the square of the net electric field amplitude of interfering beams.

Interference between two beams \mathbf{E}_1 and \mathbf{E}_2 is

$$\mathbf{E}_1 = E_{01}e^{i(\omega_1 t + \theta_1)}, \quad \mathbf{E}_2 = E_{02}e^{i(\omega_2 t + \theta_2)}, \quad \mathbf{E}_{\text{net}} = \mathbf{E}_1 + \mathbf{E}_2$$

Irradiance is
$$I = \frac{c\epsilon_0}{2} \mathbf{E}_{\text{net}}^2 = \frac{c\epsilon_0}{2} (|\mathbf{E}_1|^2 + |\mathbf{E}_2|^2 + 2\mathbf{E}_1 \cdot \mathbf{E}_2)$$

$\epsilon_0 \cong 8.85 \times 10^{-12}$ F/m is the vacuum permittivity.

Detected irradiance is
$$I_D = \int_{A_D} I \, dA_D$$

The detected voltage V_D on a photodetector is the detected irradiance times a sensitivity factor based on detector properties. The sensitivity factor is the wavelength-dependent optical power to electrical current efficiency η_λ times the transimpedance amplifier gain G . For **plane waves**, which have a flat wavefront with uniformly distributed optical power, $V_D = \eta_\lambda G I A_D$.

For displacement interferometry, the irradiance simplifies to two DC-level terms ($|\mathbf{E}_1|^2$ and $|\mathbf{E}_2|^2$) and a dot product term ($\mathbf{E}_1 \cdot \mathbf{E}_2$) that is the **interference term**. These terms have the following form:

$$2 \cos A \cos B = \cos(A + B) + \cos(A - B)$$

Both electric fields have optical frequencies that are too fast to detect, given the practical limitations of detection electronics. In the interference term, the additive term is too fast to detect, meaning that only the difference is considered, leaving a signal of the form

$$I \propto V_i = A \cos(\omega t + \theta) + B$$

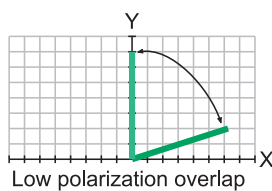
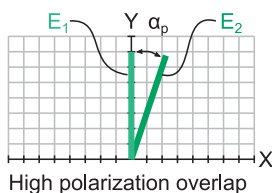
Polarization Overlap

Measuring high-quality interference signals is critical for displacement interferometry. The detected irradiance determines a measure of the average optical power incident on a photodetector, assuming no interference. When interference occurs, the optical power shifts, changing the amount of detected signal. Constructive interference leads to higher levels of detected irradiance, whereas destructive interference leads to lower levels of detected irradiance.

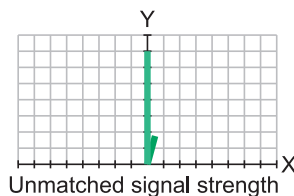
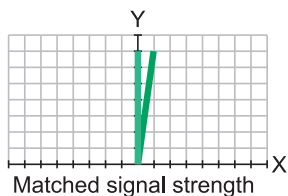
The detected interference signal quality is largely determined by the alignment, **polarization overlap**, and ratio of electric field **signal strengths**. When the beams have the same relative polarization orientation α_p , the detectable interference (due to polarization) is maximal. As the angle between the beams' relative polarizations increases, the detectable interference reduces. Because of the dot product relationship in the interference, beams with orthogonal polarization states do not interfere.

Interference term

$$\mathbf{E}_1 \cdot \mathbf{E}_2 = |\mathbf{E}_1| |\mathbf{E}_2| \cos \alpha_p$$

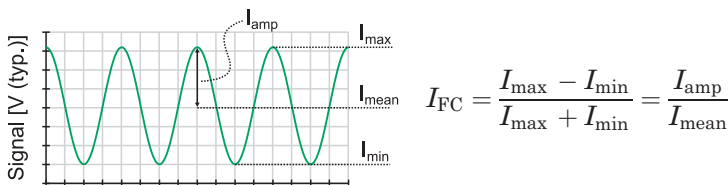


Complete polarization overlap and electric fields with equal amplitudes result in the maximum amount of **fringe contrast** in the interference signal. Electric fields with different amplitudes reduce the fringe contrast. The unequal amplitudes lead to a greater DC-level signal with a smaller superimposed interference signal.

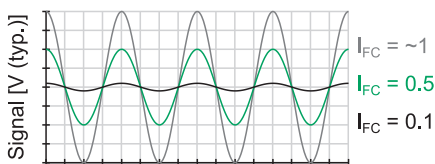


Fringe Contrast

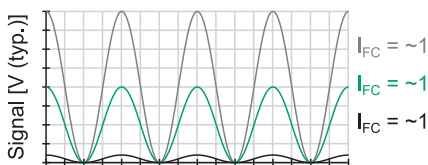
Fringe contrast is a measure of the interference quality. Good fringe contrast is needed to accurately measure interference signals. When the contrast is too low, the signal-to-noise ratio decreases. Fringe contrast is scaled 0 to 1, where 0 is no fringe contrast, and 1 is perfect fringe contrast.



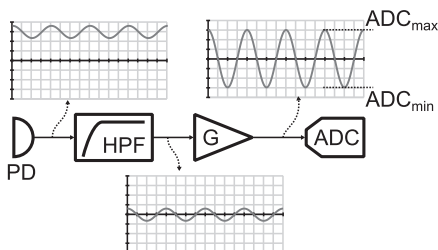
Be sure to use a DC-coupled detector when measuring fringe contrast. Adjust the interferometer alignment to maximize the fringe contrast in the optical signal. Then, use electronic filtering and amplification to maximize the signal for analog-to-digital conversion.



High DC offset leads to varying fringe contrast for different signal amplitudes.








If the signal mean is half of the amplitude, then the maximum fringe contrast is observed.



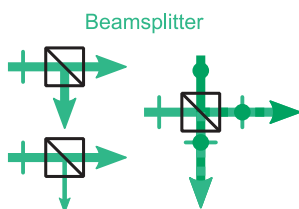
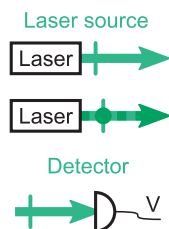
Use a high-pass filter (HPF) and an amplifier (G) to maximize the signal amplitude for analog-to-digital conversion (ADC).

Interferometer Components and Notation

-  Linearly polarized beam with optical frequency f_1 . Polarized parallel to the X axis.
-  Linearly polarized beam with optical frequency f_2 . Polarized parallel to the Y axis.
-  Two coaxial, orthogonally polarized beams with frequencies f_1 and f_2 .
-  Right-hand circularly polarized optical beam with frequency f_1 .
-  Left-hand circularly polarized optical beam with frequency f_2 .

Typically, outputs are either one linearly polarized beam or two orthogonally polarized heterodyne beams.

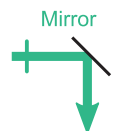
Photodetectors (PDs) are used for converting optical signals to voltage signals.



Beamsplitter

Beamsplitters (BSs) combine or split optical beams, irrespective of beam polarization. Also, BSs can split beams equally or with different transmission and reflection ratios.

Mirrors (M) are used for steering the beam in free space. Mirrors oriented normal to the beam direction can be used to direct the beam back down the same path.

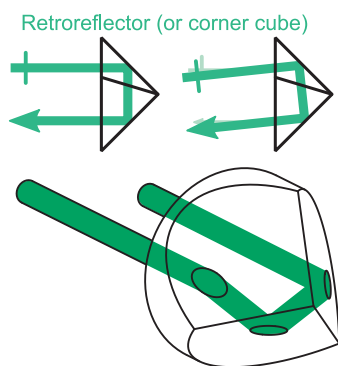
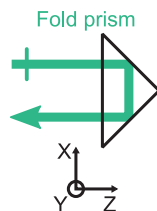


Right angle prisms can also be used to steer optical beams, typically to turn the beam 90 deg. These prisms are commonly used instead of a mirror to maintain a specific path length in glass or because the prism can be directly mounted to other optical components.



More Interferometer Components

A **fold prism** is the same shape as a right angle prism, but the beam enters and exits from the same surface. The line symmetry in the fold prism means that the output beam is directed back at the same in-plane angle φ_y as the input beam. Out-of-plane rotations φ_x of the prism cause an angular misalignment.

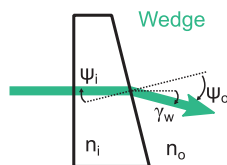
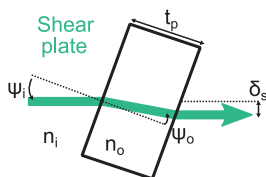


A **retroreflector** (RR) reflects an optical beam back in the same direction from which the beam entered the component. An RR consists of three orthogonal surfaces. When a beam enters, it reflects off of all three surfaces, making the output beam parallel to the input beam, even if the component is rotated about φ_x or φ_y .

Shear plates are used to laterally displace (or shear) the beam by tilting an optical flat. The amount of shear depends on the tilt angle, refractive indices, and plate thickness t_p . **Snell's law** dictates the angles of refraction:

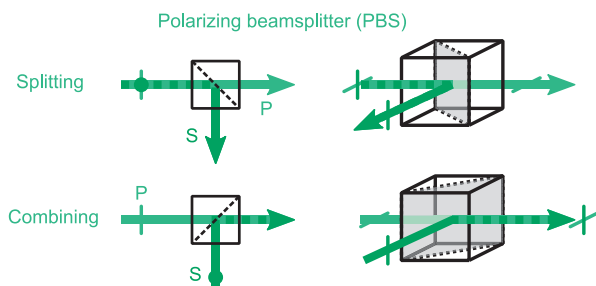
$$n_i \sin(\psi_i) = n_o(\psi_o)$$

Wedge optics are used to change the beam propagation angle, typically for small angles where mirrors are less desirable. Snell's law also dictates the refraction at the exiting surface.

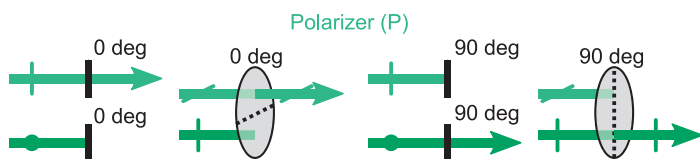


Polarization-Based Components

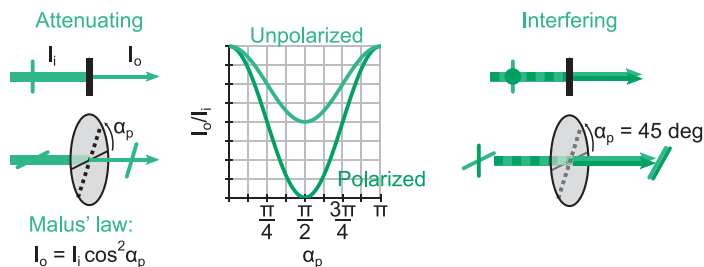
Polarizing beamsplitters (PBSs) split and combine optical beams based on their polarization state. Typically, **p-polarized light** transmits, and **s-polarized light** reflects. A PBS is used with other polarization manipulation techniques to make compact DMIs.



Polarizers filter light based on the linear polarization. Light with polarization components aligned to the **fast axis** are transmitted, while components not aligned to that axis are attenuated.

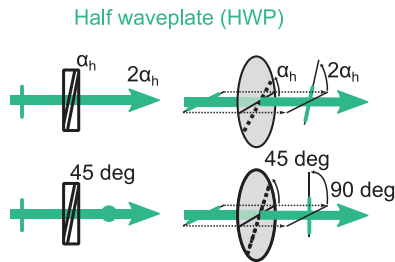


Following **Malus' law**, polarizers can attenuate optical beams. A special case uses a polarizer to make two orthogonally polarized optical beams interfere. Each beam is attenuated by $1/\sqrt{2}$, but their polarizations are aligned to enable interference detection.

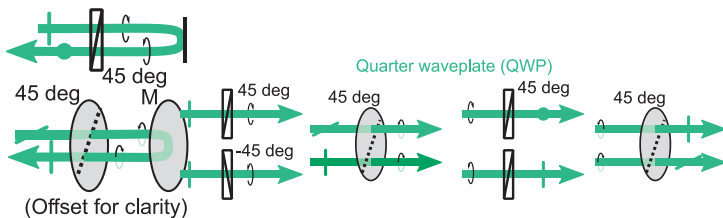


Waveplates

Half waveplates are used for rotating the polarization axis of an optical beam. The beam rotates twice the angle of rotation α_h between the HWP fast axis and the beam's input polarization state.



Quarter waveplates are used for changing a linearly polarized optical beam to become circularly polarized (and vice versa). When a QWP's fast axis is aligned to 45 deg with respect to a linearly polarized input beam, the output is circular. Similarly, when the input is circular, the output is linear. When the QWP's fast axis is not aligned to 45 deg, the output beam is elliptical.



DMIs commonly pass a linearly polarized beam through a QWP aligned at 45 deg. Then, a mirror is used to reflect the beam back down the same path, reversing the polarization **handedness**. When the beam passes through the QWP for a second time, the output polarization is 90 deg with respect to the input.

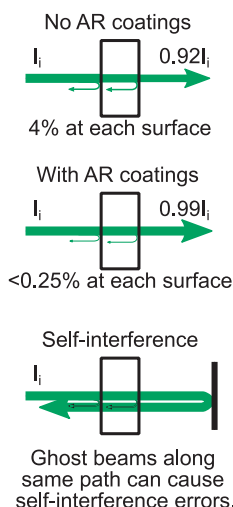
The terms *half* and *quarter* waveplate refer to the amount of phase retardation at the specified wavelength (633 nm for DMI). Unlike other optical components that can often be used at multiple wavelengths, waveplates must be used at their design wavelength; otherwise, the output will be elliptical.

Ghosts, Absorption, and Scatter

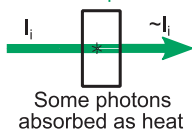
No optical component can perfectly transfer light from one state to another. Some of the light is lost or creates spurious reflections that degrade the beam quality and reduce optical power.

The most common spurious reflections are **ghost reflections**. Ghost reflections occur at every air-to-component interface where there is a large refractive index change. For normal incidence air-to-glass transitions, $\sim 4\%$ is reflected. Ghost reflections are highly undesirable because the ghost beam is often directed back down the same optical path, sometimes causing detection errors. **Antireflection** (AR) coatings can minimize ghost reflections, typically down to below 0.25% .

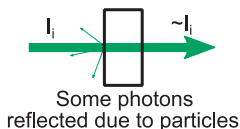
Ghost reflections



Absorption



Scatter

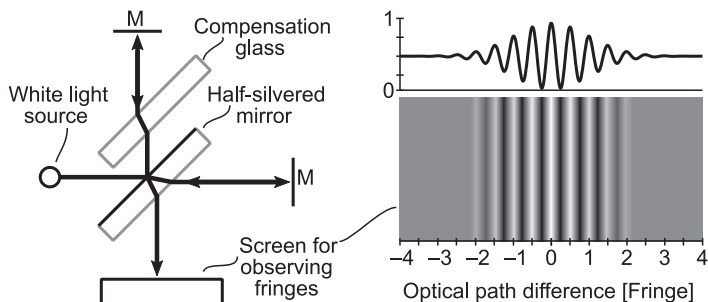


In DMIs, **absorption** and **scatter** typically reduce the available optical power. Of the two, absorption is less desirable because the absorbed optical power translates to energy absorbed by the optical component, causing the element to slightly increase in temperature. Too much component heating can cause transmitted wavefront distortion or beam misalignment. Scatter results from spurious particles on the optical surface or a void within

an optic, causing the light to follow an unintended path. Scattered light is usually ejected from the DMI, reducing the available optical power, but is not generally a significant problem.

Michelson's Interferometer

Albert Michelson demonstrated the first interferometer in 1887 using a white light source, a half-silvered mirror, compensation glass, and mirrors. The half-silvered mirror acted as a beamsplitter, and the compensation glass was used for nulling the nominal **optical path difference** between the measurement arm and the reference arm. Once the optical paths were nulled, the resulting fringe pattern contained several visible **fringes** with sharp contrast in the center, trailing off to no contrast several fringes away.



The critical aspect of **Michelson's interferometer** was that the optical path in each arm had to be identical in order to observe interference fringes. Fringes are the direct observation of constructive and destructive interference. In Michelson's original experiments, the fringe location was tracked to fractions of a fringe, enabling precise measurement.

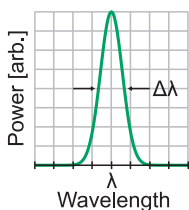
Since Michelson's time, there have been numerous advances in optics, interferometry, and supporting fields, including **long coherence** sources, polarization-manipulating components, photodetectors for converting optical power to electrical current, and measurement electronics. Twyman and Green modified Michelson's interferometer using collimated light, which is how most DMIs are used today. Nevertheless, DMIs are often described as **Michelson interferometers** rather than **Twyman-Green interferometers**.

Temporal Coherence

Michelson used **white light** to perform his interferometry experiments, allowing him to observe that the optical paths between both measurement and reference arms were equal. However, Michelson aligned his system using light from a yellow sodium flame because the fringes had a longer **temporal coherence**. The **spectral linewidth** of the sodium flame was narrower than that of the white light source, meaning that the fringes could be visible without having nulled the optical paths.

A long **coherence length** L_c (or short spectral linewidth $\Delta\lambda$) source enables interferometry over large optical path differences without sacrificing **fringe visibility**.

Spectral linewidth

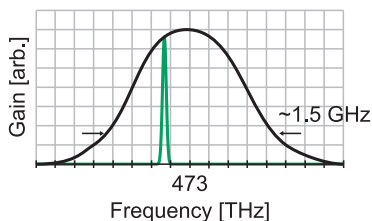


$$L_c = \frac{2 \ln(2)}{\pi n} \frac{\lambda^2}{\Delta\lambda} \approx 0.44 \frac{\lambda^2}{\Delta\lambda} \text{ [in air]}$$

The spectral width is measured at **full-width at half-maximum (FWHM)**.

It is often more convenient to determine the coherence length based on the laser frequency spectrum than on the linewidth. In DMI, typically, red light from a HeNe laser source with a wavelength of 633 nm (473 THz) is used. Frequency stabilizing the laser can significantly increase the coherence length, allowing for measurements of long optical path differences. While the actual HeNe frequency spectrum can vary within the 1.5-GHz frequency spectrum, the linewidth is much narrower.

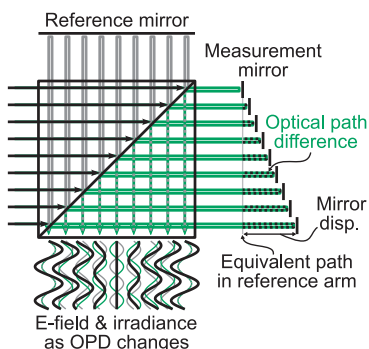
HeNe gain spectrum



$$L_c \approx 0.44 \frac{c}{\Delta f} \text{ [in air]}$$

Displacement from Phase Change

In DMI, narrow-linewidth sources are used, ensuring that interference occurs even when there are long **optical path differences** (OPDs) between the **measurement arm** and **reference arm**. The reference arm of the interferometer is the optical path that the light takes after the main splitting surface until it interferes with the light from the measurement arm. Similarly, the measurement arm is the optical path of the light after the main splitting surface that travels to and from the measurement target before interfering with the light from the reference arm.



$$\theta = \frac{2\pi z_o}{\lambda} = \frac{2\pi nNz_p}{\lambda} = \frac{2\pi nNz_p f}{c}$$

When the OPD is $m\lambda$ (for $m = 0, 1, 2, \dots$), the arms constructively interfere because both optical beams are in phase. As the OPD changes to fractions of wavelengths, the corresponding interference phase changes proportionally. These **phase changes** are directly proportional to the change in OPD.

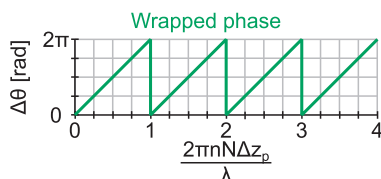
Since the measured phase is a modulo- 2π signal, the absolute phase is unknown, and only phase changes can be measured.

$$\Delta\theta = \frac{2\pi nN\Delta z_p}{\lambda} \rightarrow \Delta z_p = \frac{\lambda \Delta\theta}{2\pi nN}$$

When light reflects N times from a moving target, the optical path is twice the physical displacement, scaled by the refractive index. Thus, N is twice the number of passes:

$$z_o = nNz_p$$

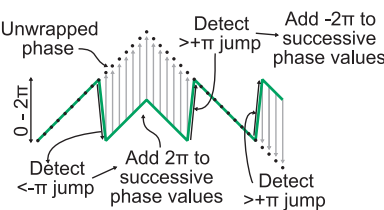
When the OPD is $m\lambda$ (for $m = 0, 1, 2, \dots$), the arms constructively interfere because both optical beams are in phase. As the OPD changes to fractions of wavelengths, the corresponding interference phase changes proportionally. These **phase changes** are directly proportional to the change in OPD.



Displacements larger than λ/nN result in a wrapped measurement phase signal.

Unwrapping and Folding

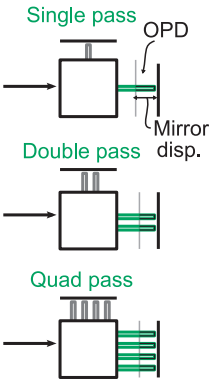
When the moving target is displaced in the same direction, the phase continues to change proportionately until the measured phase jumps 2π . Then, the measured phase continues to change again as the stage displaces until the next 2π -phase jump occurs, and so on. The actual stage displacement is determined after **unwrapping** the phase signal.



A basic unwrapping algorithm detects phase changes greater than $\pm\pi$. When that jump occurs, 2π with the opposite sign as the jump direction must be added

to successive phase values. At least four points per fringe are needed to ensure that the direction does not flip while unwrapping during high accelerations.

One method to increase phase resolution in DMIs is to increase the number of passes to the measurement target. The **interferometer fold constant** N determines the scaling factor between the measured phase and the target displacement. The phase resolution increases N times, making more-sensitive measurements possible. The interferometer type is often referred to as the number of passes or trips the measurement arm beam makes to the target; e.g., a double-pass interferometer.



The interferometer fold constant determines the measurement target needed for either a retro-reflector or a mirror; both have tradeoffs.

Pass	N	Target
Single	2	Retro
Double	4	Mirror
Quad	8	Mirror

Interferometry Systems

Interferometers consist of several basic optical components designed to split and direct the input beam(s) such that light from one optical path can be interfered with light from another optical path. **Interferometry systems** are generally classified as either **homodyne** (single-frequency) or **heterodyne** (two-frequency) systems. In many cases, the optical layout for both homodyne and heterodyne systems is very similar, if not the same.

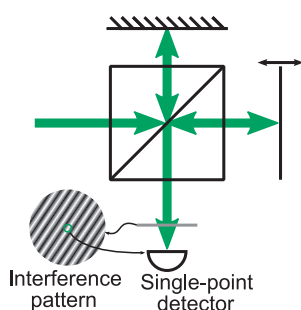
The major differences between the two systems are:

- Although both systems require a stabilized laser source, heterodyne systems require an additional method to generate two optical frequencies.
- Commercial homodyne interferometers generally obtain phase information by phase quadrature signals, whereas heterodyne interferometers use frequency modulation.
- Velocity is limited in heterodyne interferometers by the **split frequency**. (Note that this velocity limit can still be several meters per second). Homodyne systems are limited by the phase-measuring electronics.
- Homodyne interferometers can be fiber delivered with fewer problems than heterodyne interferometers.
- Heterodyne interferometers can be split to multiple axes with fewer detectors than homodyne interferometers.

The following pages first detail homodyne interferometers, followed by heterodyne interferometers. In most cases, the interferometer configuration is readily adaptable between homodyne and heterodyne variants. The chronology of this discussion illustrates basic concepts in a simple manner and then progressively adds components and concepts to eventually arrive at typical commercial layouts. In some cases, the described layout is impractical and is simply used to illustrate a concept.

Homodyne Interferometer

The basic **homodyne interferometer** consists of a single-frequency beam, a beamsplitter, two mirrors, and a detector. The beamsplitter equally splits the incoming beam where one arm travels to a fixed mirror and back, while the other arm travels to a moving mirror and back.



The two electric fields constructively (or destructively) interfere when they overlap, depending on the relative path lengths of the two arms. Changing the relative path lengths of the arms causes a relative phase change, which is detected by the measured irradiance (optical power at the detector).

Because the measurement mirror can both displace and tilt, the interference signal is sensitive to both motions. The interference pattern should be aligned to reduce the number of tilt fringes. During measurement, the single-point detector then tracks the irradiance changes in one spatial location within the interference pattern.

Basic homodyne interferometer advantages:

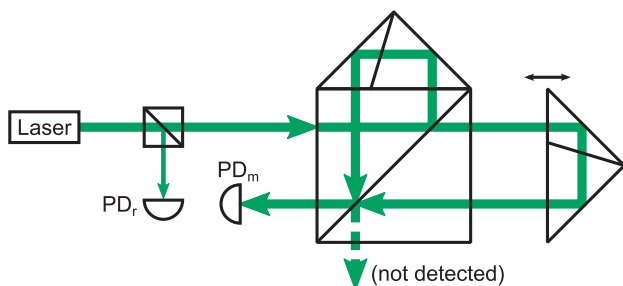
- System has few components and is easy to align.
- Plane mirror target means it can be used for multiaxis systems.
- Single-point detector enables faster processing than a CCD array.

Basic homodyne interferometer disadvantages:

- System is sensitive to intensity fluctuations and stray light, measured as false length changes; **fringe contrast** is highly significant.
- System is sensitive to both mirror displacements and tilting.
- The lack of directional sensitivity means that it cannot determine whether the mirror moved forward or backward, only that the mirror moved.

Retroreflector Homodyne Interferometer

A more common system than the homodyne or heterodyne is the **retroreflector homodyne interferometer**, which uses two retroreflectors as reference and measurement targets. Retroreflectors reflect light back to the source, parallel to the incident beam but laterally displaced if the input beam is offset from the retroreflector center. This makes both the reference and measurement arms largely insensitive to tilting effects. Linear displacement can be more easily measured, even when the target rotates during motion. Lateral displacement errors of the target (**straightness**) are not a factor if both arms interfere at the detector.



A separate beamsplitter and detector (PD_r) can measure the laser power fluctuations and can be used for correcting errors by normalizing the optical power seen at PD_m .

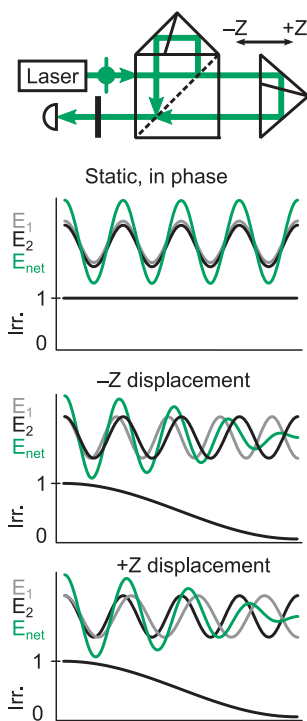
Retroreflector homodyne interferometer advantages:

- Reference and measurement targets are tilt insensitive.
- System is insensitive to straightness errors if sufficient beam overlap occurs at the detector.
- System is insensitive to laser power fluctuations if irradiance is normalized.

Retroreflector homodyne interferometer disadvantages:

- System is sensitive to stray light, even if irradiance is normalized.
- System lacks directional sensitivity.
- Irradiance normalization requires additional optical and detector components and additional signal processing.
- Use of optical power is inefficient.

Directional Sensitivity



Homodyne interferometers are sensitive to stray light and laser power fluctuations, which cause displacement errors. However, their biggest disadvantage is their lack of **directional sensitivity**.

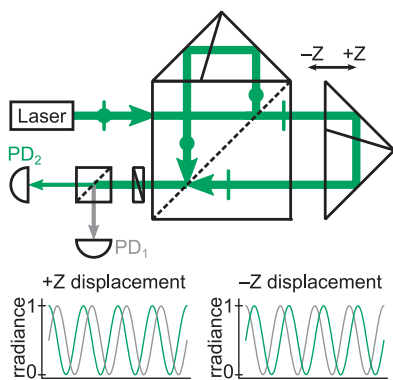
When the two electric fields constructively interfere, the measured irradiance is at its maximum. As one electric field (E_1 , in this case) **Doppler shifts** 180 deg out of phase from target retroreflector displacements, the two electric fields destructively interfere, leaving the measured irradiance at its minimum.

Because only the irradiance is measured, positive Doppler shifts cannot be distinguished from negative Doppler shifts; the net effect on the measured irradiance is the same in either case.

Two methods to determine directional sensitivity are:

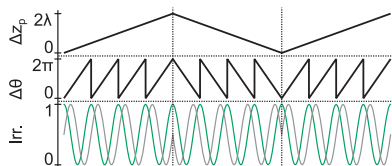
1. Generate quadrature signals with a known phase shift, a so-called **phase quadrature** measurement. This is the common method for most commercial systems. Phase quadrature measurements can be made mostly insensitive to stray light because both signals are equally affected.
2. Implement **amplitude demodulation**. This is achieved by modulating the laser intensity with a known carrier frequency and demodulating with respect to the carrier frequency. The carrier frequency is determined using the drive signal for the modulation or a separate detected reference signal.

Direction-Sensitive Homodyne Interferometer



Directional sensitivity can be implemented by using **polarization manipulation**. Once the measurement and reference arms interfere at the polarizer, they can be split again, and a QWP can be used to delay one beam by 90 deg. Two detectors are then used to determine the phase and direction of the phase change. This is called a **phase quadrature measurement**.

The phase shift means that the two measured signals can be compared relative to each other to determine the direction. For instance, the non-phase-shifted signal (PD₁) reaches its maximum value before the phase-shifted signal (PD₂), while moving in the positive Z direction. This flips for the opposite displacement direction.



Direction-sensitive homodyne advantages:

- Laser power fluctuations and stray light are mostly common mode between both detectors (reduced errors).
- Interferometer has directional sensitivity.
- System uses simple detector and signal processing to measure displacement.
- Source can be fiber delivered with minimal problems.

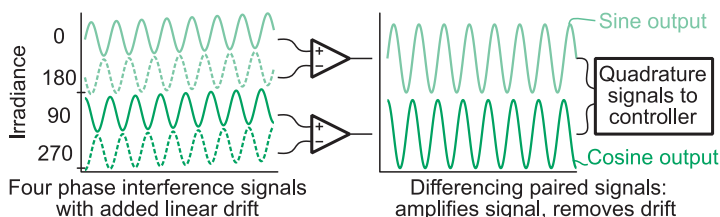
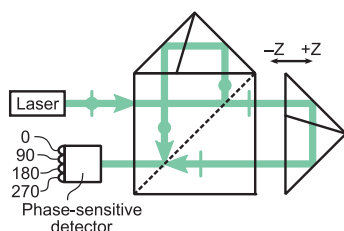
Direction-sensitive homodyne disadvantages:

- Additional optical components are needed prior to detection.
- Polarization axis misalignment can cause nanometer-level errors.
- System requires two detectors per single measurement axis.

Homodyne Laser Encoder

Commercial homodyne systems are often called **homodyne laser encoders** due to their similarity to line-scale or rotary encoders. The key component in a homodyne laser encoder is the **phase-sensitive detector**, which is actually a series of photodetectors that typically measure four different phases of the interference signal. A series of beamsplitters and waveplates or a special detector can be used to generate the four needed phases.

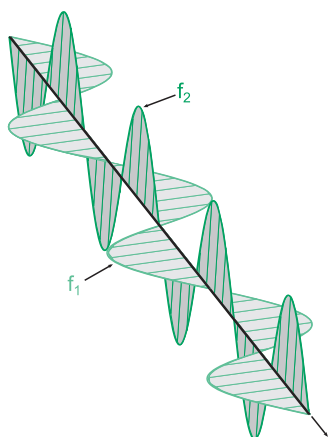
Four separate phases of the interference signal are used for three reasons: (1) to provide directional sensitivity, (2) to limit the effects of stray light, and (3) to have a common phase quadrature signal output that is commonly used in stage feedback systems.



The four measured phases are 0, 90, 180, and 270 deg. The 0- and 180-deg phases and the 90- and 270-deg phases are separated into pairs and differenced. The purpose of differencing the opposite phase signals is to cause common mode fluctuations such as stray light to drop out and to increase the signal amplitude. This produces two signals with a 90-deg phase shift used for phase quadrature measurements. The main advantage of this system is that fiber-delivered laser sources can be used; the main disadvantage is that it requires four detection channels and accurate phase shifting.

Heterodyne Interferometry Systems

Heterodyne interferometers are generally similar to their homodyne counterparts. However, they are directionally sensitive, largely immune to stray light power fluctuations, and have higher optical power efficiency for multipass and multi-axis systems.



Typically, the laser source contains two distinct optical frequencies with a known frequency difference f_s (also called the split frequency) and orthogonally polarized states. The collinear beams mean that propagation effects prior to the interferometer are common mode. The two optical frequencies can be separated because orthogonal polarization states do not interfere.

One optical frequency is used in the reference arm, and the other is used in the measurement arm. Interference is created by passing the collinear, orthogonal beams through a polarizer aligned at 45 deg. Then, the interference is measured using a photodetector.

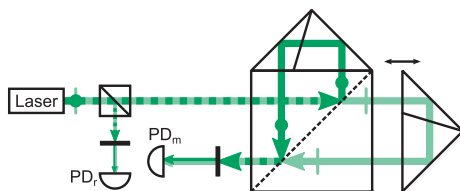
The critical difference between heterodyne and homodyne interferometry is that in the former, the phase information is carried at the split frequency instead of measuring DC-level fluctuations. This means that changes in OPD manifest as positive and negative phase shifts.

$$\begin{aligned}
 I &= \frac{c\epsilon_0}{2} \left(\underbrace{|\vec{E}_1|^2 + |\vec{E}_2|^2}_{\text{DC terms}} + \underbrace{2\vec{E}_1 \cdot \vec{E}_2}_{\text{Interference term}} \right) \\
 &\quad \text{has the form} \quad \underbrace{2 \cos f_1 \cos f_2}_{\text{too fast to process (ignore)}} = \underbrace{\cos(f_1 + f_2)}_{\text{main signal}} + \underbrace{\cos(f_1 - f_2)}_{\text{main signal}} \\
 I &\propto A \cos(2\pi f_s t + \theta)
 \end{aligned}$$

Basic Heterodyne Interferometer

The basic **heterodyne interferometer** is similar to the polarization retroreflector homodyne interferometer, except that a two-frequency optical source is used instead of a single-frequency laser. An initial beamsplitter splits part of the laser output, and a polarizer interferes the two beams. The resulting interference is detected at PD_r , generating an **optical reference**. An electronic reference can be used if the optical reference is from a stable source.

The main optical beams travel to the PBS, where one optical beam f_2 reflects at the splitting surface, while the other beam f_1 transmits. Both beams reflect from reference and measurement retroreflectors before combining again within the PBS. A polarizer then interferes the combined beams, and PD_m is used to measure the irradiance.



Heterodyne interferometer advantages:

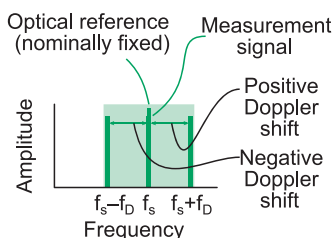
- System has inherent directional sensitivity (no added manipulation).
- One optical reference is used for many interferometers (multiaxis).
- System is insensitive to laser power fluctuations and stray light.
- System can measure fast-moving targets more easily.
- System is easily adaptable for multipass configurations (resolution enhancement and tilt-insensitive plane mirror targets).

Heterodyne interferometer disadvantages:

- Hetrodyne source with a known split frequency is required.
- Detection and signal processing at high speeds are needed.
- Polarization manipulation leads to longer alignment procedures and more-costly polarization components.

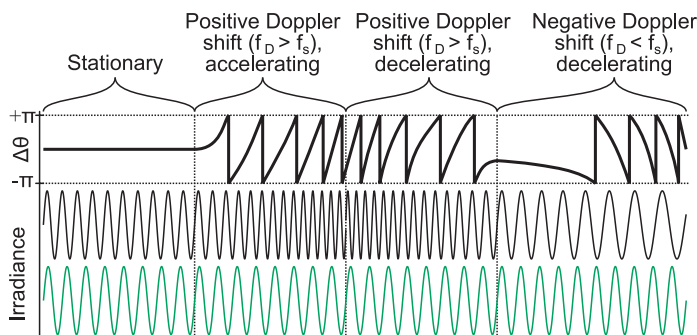
Heterodyne Directional Sensitivity

Directional sensitivity in heterodyne interferometry is obtained based on the frequency difference between the reference interference signal and the measurement interference signal. The reference interference signal (or **optical reference**) is typically constant at a known frequency f_s based on the heterodyne laser source. When the measurement target is stationary, the measurement interference signal is constant and equal to the optical reference. When the measurement target moves, a Doppler shift occurs in the measurement interference signal, causing the frequency to increase or decrease.



In the **Fourier spectrum**, the optical reference is fixed. When the measurement signal has a frequency lower than the optical reference, the target is moving away from the interferometer because the signal is undergoing a negative Doppler shift.

Similarly, measurement signals with a higher frequency than the optical reference undergo a positive Doppler shift.



Because the phase change is measured relative to a signal with a defined frequency, there is no directional ambiguity. As long as the phase is correctly unwrapped or fringes are counted, heterodyne interferometers are inherently sensitive to direction.

Homodyne and Heterodyne Comparison

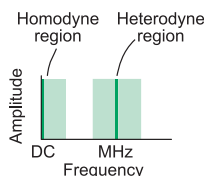
Homodyne and heterodyne systems can be compared based on their typical subsystems. The following table gives a general overview; however, specific systems that have capabilities not listed here might be available.

Subsystem	Homodyne	Heterodyne
Stabilized laser	Needed	Needed
Heterodyne frequency	Not needed	Needed
Optical reference	Not needed	Needed
Fiber delivery	Possible	Causes errors, or special interferometers needed
Interferometer	Variety of configurations	Variety of configurations
Detection	Multiphase photodetector, or special detection needed	One measurement photodetector needed
Detection bandwidth needed	DC-level baseline	Megahertz detection bandwidth needed
Electronics	DC level subject to $1/f$ noise	Can use bandpass filter at desired frequencies

One special consideration—**multiaxis systems**—is not easily summarized in a table. Homodyne systems can use a common laser source, but everything else (interferometer, detection, and signal processing) must be duplicated per axis. Heterodyne systems, conversely, can use a common laser source, optical reference, and signal processing electronics for multiple axes. Also, the megahertz-level baseline for heterodyne interferometry enables the filtering of electrical DC drift, generally providing the highest precision measurements.

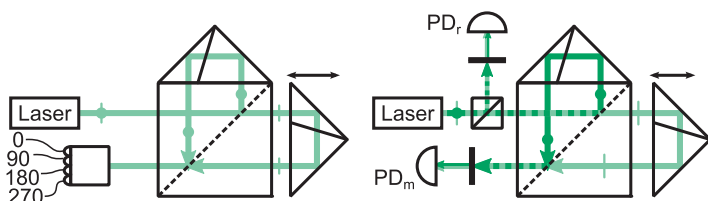
Homodyne and Heterodyne Comparison (cont.)

The detection frequencies are different in homodyne and heterodyne systems. Homodyne interferometers have a **DC-level baseline** frequency that increases as the target **Doppler shift** increases. Even with very high **Doppler shifts**, detection bandwidths up to only a few megahertz are needed. Heterodyne interferometers use frequency modulation, where the target displacement causes an instantaneous frequency change (phase) in the carrier signal. Otherwise, when the target is stationary, only the nominal carrier frequency is detected. Phase changes relative to the carrier frequency determine the direction.



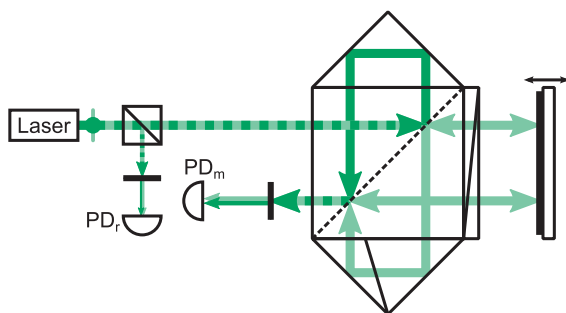
Heterodyne interferometers typically have a **heterodyne frequency** in the megahertz regime. This difference means that very high detection bandwidths are needed for heterodyne systems, but DC-level noise can be filtered from the signal, providing very sensitive measurements. Heterodyne systems tend to be more complex and costly because the laser source requires two optical frequencies, and high-speed detection and signal processing are needed.

In this *Field Guide*, homodyne and heterodyne layouts can be interchanged by several methods: switching to a heterodyne laser, adding an optical reference, or changing the measurement. The heterodyne layouts use two shades of green to clearly illustrate beam paths; however, homodyne variants can be used if minor changes are made. These two retroreflector interferometers are essentially equivalent, with homodyne and heterodyne variants.



Unequal Plane Mirror Interferometer

The two distinct disadvantages of using a retroreflector as the measurement target are: (1) the target motion can only be linear (i.e., no planar stages) and (2) the retroreflector has a large footprint (size, mass, or both). Interferometers accommodating **plane mirror targets** increase the versatility of the interferometer.



The measurement arm of the **unequal plane mirror interferometer** has its polarization state manipulated with a 45-deg QWP and retroreflector to enable two passes to the measurement mirror. This increases the sensitivity by creating a **double-pass configuration** but also increases the thermal sensitivity of the interferometer because the nominal optical path lengths between the reference and measurement arms are not equal.

Unequal plane mirror interferometer advantages:

- Plane mirror target is smaller than a retroreflector.
- Target can have motion in orthogonal directions.
- Double-pass interferometer configuration doubles the phase-change-to-displacement resolution.
- Retroreflector at the interferometer makes the interferometer insensitive to tilt.

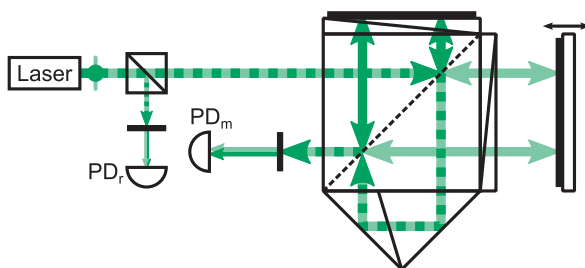
Unequal plane mirror interferometer disadvantages:

- Nominal OPD between interferometer arms is not equal.
- Beam-mixing errors increase due to multiple passes.
- Thermal sensitivity increases in the interferometer.

Plane Mirror Interferometer (PMI)

Due to thermal expansion of the glass, the unequal plane mirror interferometer often has a large thermal sensitivity, reaching 100 nm/°C or more. This thermal sensitivity is prohibitively high in many precision applications.

The solution to removing this sensitivity is to create an equal double-pass configuration to the reference mirror using another 45-deg QWP. The only OPD is then the distance to the measurement mirror position.



The added QWPs in both arms increase the sensitivity to polarization alignment. Slight polarization misalignments can increase **frequency mixing** from the source and lead to **periodic error** in the phase measurement.

Plane mirror interferometer advantages:

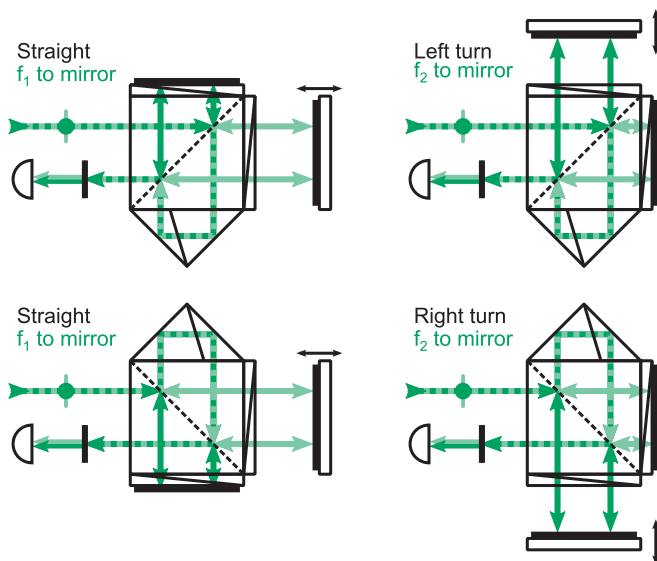
- Plane mirror target is smaller than a retroreflector.
- Target can have motion in orthogonal directions.
- Double-pass interferometer configuration doubles the phase-change-to-displacement resolution.
- Retroreflector at the interferometer makes the interferometer insensitive to tilt.
- Equal nominal paths exist between measurement and reference arms.
- Thermal sensitivity is minimal.

Plane mirror interferometer disadvantages:

- Beam-mixing errors increase due to multiple passes, increasing periodic error.
- Increased components and alignment are required.

PMI Variants

Various **plane mirror interferometers** can be designed with slightly different optical layouts. Because the measurement and reference arms are orthogonally and arbitrarily designated, either beam can be sent to the measurement target. Thus, the input beam can be parallel or orthogonal to the normal measurement direction. This allows for flexibility in building the optical layout, especially for multiaxis interferometry systems. In particular, different configurations are useful for reducing the number of steering mirrors, a reduction that saves optical power and can reduce complexity.

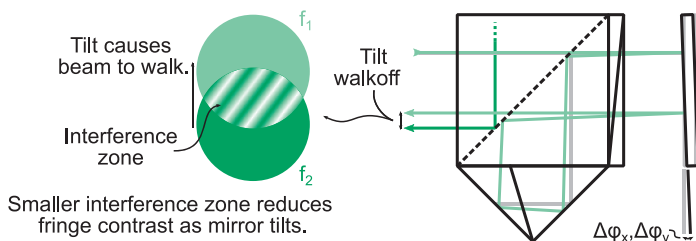


One aspect to consider in heterodyne interferometers is the wavelength of the beam traveling to the target. This is a potential source of error if the incorrect wavelength beam is used when calculating the displacement.

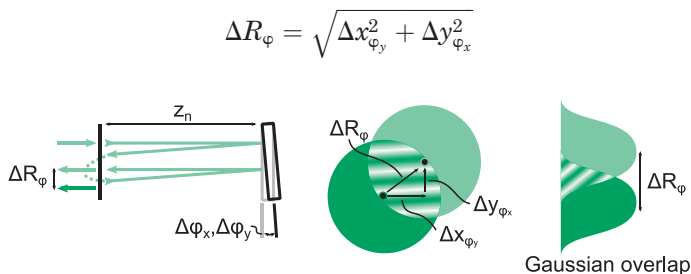
Interferometers comprising modular components can readily switch between configurations. However, some specialized interferometers have directly bonded components, where the coating acts as the fixed mirror. In these cases, the direction is fixed.

Beam Walkoff

PMIs are largely insensitive to small target mirror tip-and-tilt motion due to the retroreflector in the interferometer. Small mirror tip-and-tilt motions do lead to lateral displacements between measurement and reference arms in PMIs. This lateral displacement, or **beam walkoff**, reduces the achievable fringe contrast because a smaller overlapping zone is created that generates the interference signal.



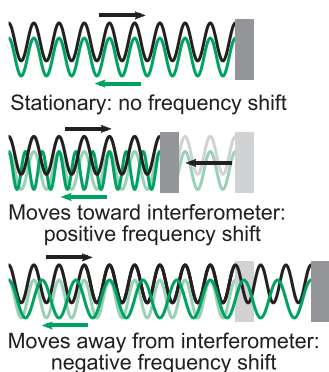
The amount of walkoff scales based on the distance z_n between the interferometer and the target. Even for small rotations, the walkoff can be significant if the distance to the target is large. For small angles, the walkoff is $\sim 2\Delta\phi/z_n$, which discounts the additional walkoff that will occur in the beamsplitter and retroreflector. Both tip and tilt will generate walkoff, so the total beam overlap shifts by ΔR_ϕ .



In many cases, the interfering beams have a Gaussian profile. Small walkoff changes cause the overlapping area, and thus the fringe contrast, to significantly decrease.

Doppler Velocity

One of the benefits of displacement measuring interferometry is the ability to measure high-speed **Doppler velocities**. The **Doppler shift** f_D is the frequency shift induced in the measurement optical beam resulting from target velocity. The frequency shift can be measured as the phase derivative or temporal phase change in a specified period, provided that sufficiently high sampling parameters are met and that the 2π -phase wrapping is successfully unwrapped.

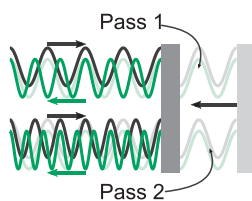


When the target is stationary, no Doppler shift takes place. When the target moves toward the interferometer, a **positive Doppler shift** occurs, causing the measurement optical beam to increase in frequency. Likewise, targets moving away from the interferometer cause a **negative Doppler shift** and a decrease in the optical frequency.

The Doppler frequency shift is proportional to the Doppler velocity v_D , which is the velocity of the moving target. Each pass to the target doubles the optical resolution and also doubles the Doppler frequency shift.

$$f_D = \frac{nNv_D}{\lambda}$$

Each pass to mirror doubles the frequency shift.



Second pass input beam has same frequency as output beam from first pass.

Generally, the Doppler frequency shift should be less than the heterodyne frequency: $f_D \ll f_s$. This ensures that the measurement interference signal is always positive and does not pass through zero frequency.

Dynamic Range and Acceleration Limitations

Displacement interferometry has a high **dynamic range**, higher than that of many other sensing technologies. Using long-coherence lasers, displacement interferometers can operate over very long distances, provided that nothing obstructs the beam. This is particularly useful in space applications, where the refractive index, the dominant error source in many applications, is negligible. For example, the LISA (Laser Interferometer Space Antenna) gravitational wave space mission has proposed interferometer arms as long as 5×10^6 km.

Additionally, modern signal processing technology with **field-programmable gate arrays** (FPGAs) or **digital signal processors** (DSPs) makes phase meter calculations and **fringe interpolation** relatively straightforward. Commercial systems readily achieve a fringe interpolation of 1 part in 4096, or approximately 0.04-nm resolution for a standard PMI. Custom systems have been shown to demonstrate even higher fringe-interpolation rates.

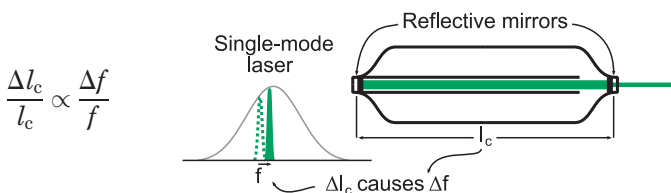
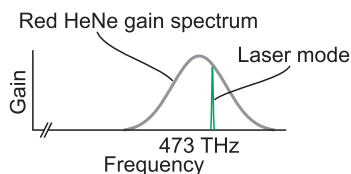
Provided that fringes can be successfully unwrapped and counted, large displacements can be measured. Similarly, as long as the heterodyne frequency is greater than the largest expected Doppler shift ($f_D \ll f_s$), high velocities can be measured. Homodyne interferometers do not have that velocity limit. High accelerations do not pose a fundamental limit on the displacement interferometer measurement but are limited based on the **phase meter electronics**.

The **acceleration limitation** for DMI measurements using both homodyne and heterodyne systems is driven by the sampling frequency, processing time, and unwrap algorithm. Manufacturers specify an acceleration limit based on their systems' capabilities.

Laser Sources

The typical **laser source** for DMI is a red HeNe laser with a 633-nm wavelength. Laser sources have three desirable traits: high frequency stability, high output power, and single TEM₀₀ mode of operation. The red

HeNe gain spectrum is approximately 1.5 GHz wide with a nominal frequency f of 473 THz. The light is generated in a laser cavity of length l_c that will change Δl_c largely from thermal expansion of the laser tube. Changes in cavity length are directly proportional to absolute frequency changes.



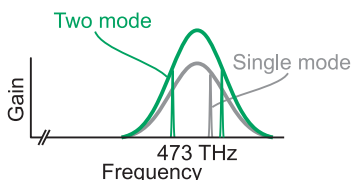
High **frequency stability** is desired for two reasons: (1) narrow-linewidth and stable-frequency sources have long coherence and (2) absolute frequency fluctuations can appear as a false length change, even if the target is stationary. Long coherence means that interference can occur even with a long OPD between interferometer measurement and reference arms.

The measurement (length) error ΔL is directly related to the ratio of the frequency fluctuations to absolute frequency and the total optical path length difference, i.e., $\Delta L = L \cdot (\Delta f)/f$. For instance, if a 633-nm HeNe laser has an absolute frequency around 473 THz and is stable to ± 2 MHz, then the expected length error from frequency fluctuations is 10 ppb or 1 part in 10^8 . For a 1-m OPD, this manifests as a 10-nm error.

Optical Power and Laser Modes

Interference signals with approximately 1 to 5 μW of heterodyne interference power can be successfully processed with most commercial phase meter systems. Higher **optical power** at the detector reduces noise from fundamental detection limits (so-called **shot noise**) and is needed for measurements requiring high bandwidth. Multiaxis systems also require a laser source with a higher optical power to ease their implementation. Inefficient optical splitting and losses at air-to-glass transitions and reflecting surfaces can significantly reduce the amount of power available for detection. Also, beam walkoff in commonly used PMIs further reduces available optical power.

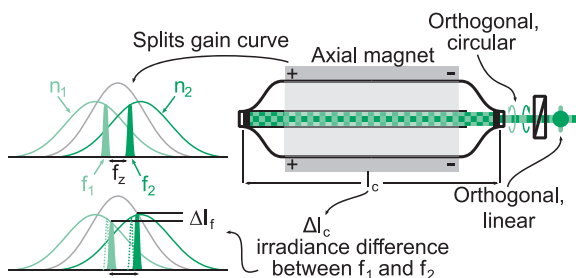
One method to increase optical power is to use a longer laser tube that can support two or more modes.



Single-mode lasers have lower power but can be **Zeeman stabilized**, which also generates an inherent 1- to 4-MHz heterodyne frequency. Longer HeNe laser tubes generate more modes and more power but require different stabilization techniques, such as intensity balancing and separate frequency shifting, to generate two collinear, orthogonally polarized optical beams with differing frequencies for heterodyne interferometry. Most commercially available stabilized lasers output between 300 μW and <2 mW.

The HeNe laser type, the number of modes supported, the method for stabilizing the frequency, and the method for generating the heterodyne frequency are essentially linked. This *Field Guide* outlines two common, commercially available laser sources and one arbitrary heterodyne frequency generation method as examples but is by no means a complete compendium.

Zeeman-Stabilized Laser



The base laser for a **Zeeman-stabilized laser** contains a single-mode HeNe laser tube with ~ 1 mW of available optical power. When the laser is placed in an axial magnetic field, the **Zeeman effect** causes the refractive index of the HeNe gas mixture to split into two different refractive indices and induces orthogonal, circularly polarized states. The refractive index difference splits the nominal HeNe gain curve into two separate curves, each with a slightly different frequency. This frequency difference is caused by the refractive index difference because the physical path length of both states is the same.

Changes in the cavity length cause the absolute frequency and, thus, the frequency difference between the two states to change proportionally. This also causes slight power fluctuations between the two states. The power difference or frequency difference between the two states can be used as a feedback signal to maintain a constant laser cavity length. A quarter waveplate then generates two heterodyne collinear output beams with linear, orthogonally polarized states.

Zeeman-stabilized laser advantages:

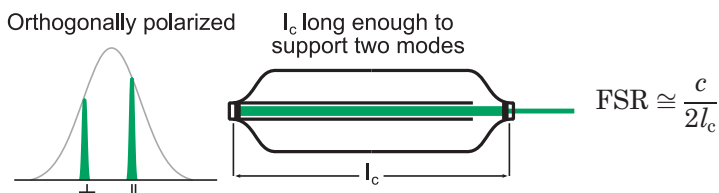
- Compact, stable source with inherent heterodyne frequency generation.
- Long-term fractional frequency stability of $\sim 1 \times 10^{-7}$.

Zeeman-stabilized laser disadvantages:

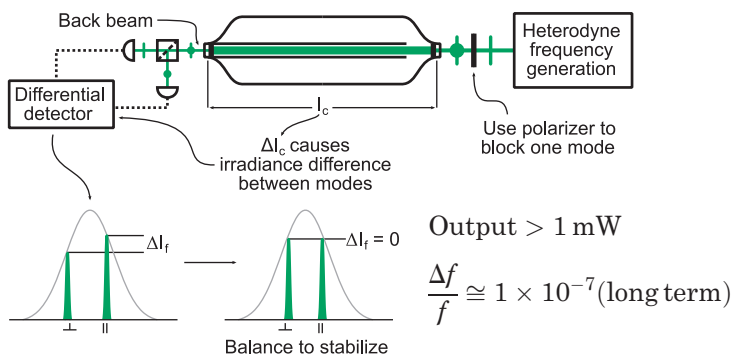
- Low output power; limited to single-mode lasers.
- Slight frequency mixing in the source.
- Susceptible to stray magnetic fields.
- Speed limitations due to < 4 -MHz split frequency.

Two-Mode Intensity-Balanced Laser

Two-mode intensity-balanced lasers provide an alternative frequency-stabilization technique with higher optical power. The number of lasing modes supported by the HeNe laser is proportional to the cavity length. The laser **free spectral range** (FSR) determines the frequency difference between successive laser modes. When the FSR is smaller than the gain spectrum, multiple modes arise with alternating polarization states.

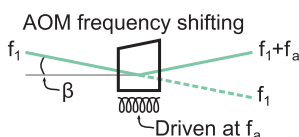


When the HeNe laser outputs two modes nominally centered in the gain spectrum, the two output modes have similar intensities. The **back beam** from the laser can be split by polarization (and thus **laser mode**) and used to stabilize the cavity length by detecting the difference in optical power between the laser modes. The optical frequencies of the two modes are stabilized by balancing the laser modes. One main polarization state is kept for homodyne systems, and the other is blocked using a polarizer. A secondary system is needed to generate the two frequencies required for heterodyne interferometry.



Heterodyne Frequency Generation

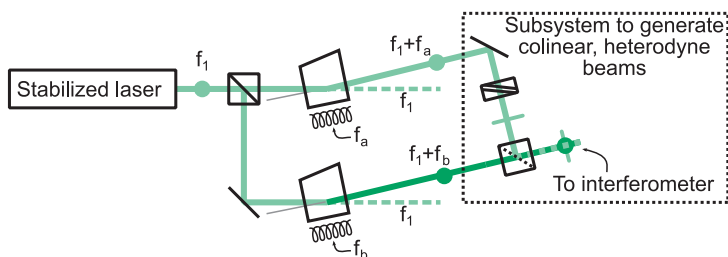
When the stabilized laser does not output two optical frequencies, a secondary system is needed for **heterodyne frequency generation** in heterodyne interferometers. One method for shifting an optical frequency by a known, precise amount is to use an **acousto-optic modulator** (AOM). AOMs are optical elements driven by a modulation frequency that **upshifts** or **downshifts** the input optical frequency by that amount. Typical frequency shifts are in the 20- to 80-MHz range with deflection angles below 10 mrad.



Output > 1 mW

$$\frac{\Delta f}{f} \cong 1 \times 10^{-7} (\text{long term})$$

The input beam is typically aligned at the **Bragg angle** with respect to the surface normal. This results in the first-order-shifted beam having the highest signal strength at an output angle of twice the Bragg angle with respect to the zeroth-order beam.



It is sometimes beneficial to use a lower heterodyne frequency in the kilohertz range rather than the megahertz range. Two common instances are when lock-in amplifiers are used for phase detection and when the velocity of the moving target is slow (<1 mm/s). In both cases, two AOMs are typically used, with different drive frequencies f_a and f_b . The heterodyne frequency is then the difference ($f_a - f_b$) between the two driving frequencies. A mirror, half waveplate, and polarizing beamsplitter can then be used to generate coaxial, orthogonally polarized beams.

Phase Measurements

Phase measurements require two key components: (1) an **interference detection** system to convert optical signals to electrical signals and (2) a processing unit to extract the phase from the measurement signals.

Most interference detection systems have filtering and amplification circuits prior to ADC for processing the phase. This is called **signal preconditioning**. Depending on three parameters: (1) the interferometer configuration (whether it is homodyne or heterodyne), (2) the anticipated measurement conditions (velocity, acceleration, range), and (3) the desired resolution, the interference detection system can have different attributes that require tradeoffs for specific performance.

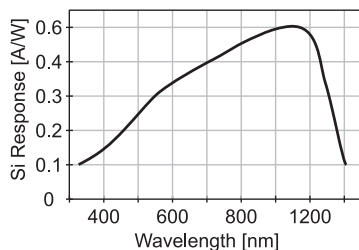
Once the optical signal has been converted to an electrical signal and preconditioned, the phase is typically computed using a **digital processor**. The signals then typically undergo further digital processing to condition and extract the phase information. Depending on the application, different processing techniques can be used to obtain the phase information. Homodyne interferometers typically employ phase quadrature algorithms to extract the phase. Heterodyne interferometers typically use lock-in detection or discrete Fourier transform methods. **Time interval analysis** can be used for both homodyne and heterodyne systems.

Homodyne interferometers have DC-level detection bandwidths, while heterodyne interferometers have frequency-modulated signals at 1 MHz or greater.

Displacement interferometers with a large optical fold factor increase both the optical resolution and the Doppler shift. While it may be beneficial to have a higher optical resolution, the increased requirements on detection and signal processing can offset those gains.

Interference Detection

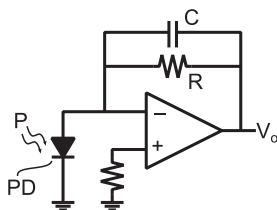
Displacement interferometers in the visible spectrum use **silicon photodiodes** to detect interference. The photodiode converts incident optical power into an electrical current. Photodiodes behave in a manner similar to a low-pass filter, based on the photodiode area. Smaller photodiodes have a faster response but cannot convert as much optical power as a larger photodiode.



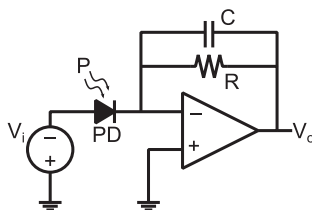
Si Sensitivity

$$\eta_{633} \approx 0.4 \text{ [A/W]}$$

Photovoltaic



Photoconductive

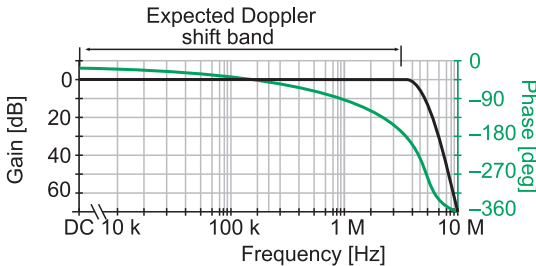


$$v_o = \eta_{633} P R \text{ [V]}$$

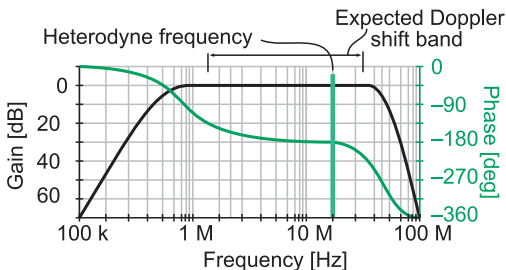
The current produced by a photodiode is converted to a voltage signal using a **transimpedance amplifier**. Two different amplifiers are used: **photovoltaic** and **photoconductive**. Photovoltaic transimpedance amplifiers have no voltage across the diode, a feature that improves the sensitivity by eliminating dark current. Photoconductive transimpedance amplifiers are reverse biased with an offset voltage to increase the response but generally have higher noise due to dark current. The voltage gain scales with R , and the noise in the amplifier scales with \sqrt{R} ; thus, feedback resistor R should be high to reduce electrical noise. Feedback capacitor C is used to prevent gain peaking and is typically small so that it does not reduce the overall response bandwidth.

Detection Bandwidth

Homodyne interferometry systems have a nominal detection frequency at DC level plus any Doppler frequency from the moving target. Both positive and negative Doppler shifts are detected as positive Doppler frequencies. The maximum **detection bandwidth** needed is a few megahertz for Doppler velocities at 1 m/s.



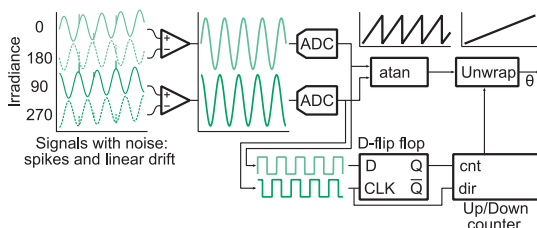
Heterodyne interferometry systems usually have a heterodyne frequency in the 1+ MHz regime, which means that the detection and signal processing system must accommodate signals in this frequency regime. The measurement optical frequency will change due to target Doppler shifts; thus, the detection system should have a nominally uniform response to signals within the $f_s \pm f_D$ **frequency band**. Signals outside of this band are filtered to reduce the noise.



Because of the heterodyne frequency, heterodyne interferometers require a significantly higher detection bandwidth than homodyne systems. Both systems require a flat phase response in the detection band to limit phase measurement errors due to changing Doppler velocities.

Phase Quadrature Measurements

Phase quadrature measurements are used to generate a matched pair of signals with a 90-deg phase shift whose absolute phase angle is proportional to the target displacement. The four phase input signals are used to compensate for noise and drift by differencing 180 deg out of phase pairs. This generates a matched sine and cosine pair that is used for processing the phase. Several methods can be used to determine the phase. One method uses a high-speed arctangent (atan) function to determine the wrapped phase. The most significant bits from the two ADCs are used to generate 1-bit digital signals. A D-flip flop and an up/down counter are used to detect 2π -phase changes for unwrapping.



One disadvantage of this system is the four-phase detection. Differences in operational amplifier (op-amp) performance, such as bias current and voltage offsets, can create slight, noncommon mode errors between the voltages. These errors do not cancel in the difference amplifiers. Additionally, the four phases must have exactly 90-deg phase differences; otherwise, periodic error will occur in the signals.

Phase quadrature measurement advantages:

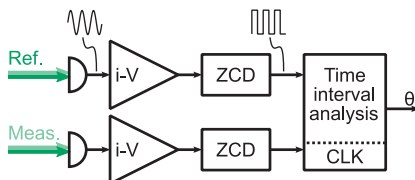
- DC-level baseline; lower frequency components needed.
- Simple signal processing; can be cost effective.
- Common mode errors such as optical drift and stray light inherently removed.
- Provides a direct interface to most machine controllers.

Phase quadrature measurement disadvantages:

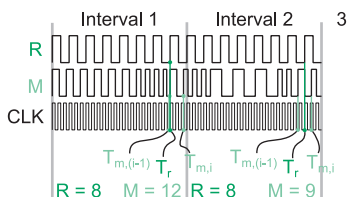
- Four matched phases needed; otherwise, errors occur at the nanometer level.
- Low-frequency errors in the op-amps cause errors.

Time Interval Analysis

Time interval analysis is a relatively simple method to measure the phase in heterodyne interferometry. Its origins stem from when microprocessor options for fixed- or floating-point calculations were limited. Both interference signals are detected, converted to a voltage using a transimpedance amplifier, and then converted to a square wave using a **zero-crossing detector** (ZCD). The two square waves then behave as digital 1-bit signals that can be compared to a fast clock (CLK).



The timestamp triggered by zero crossing is then recorded using two counters, one for the reference and one for the measurement. During a specific measurement interval, the numbers of zero crossings and timestamps are recorded. The number of displaced fringes is determined by the difference in zero crossings between the measurement and reference signals. Fractions of a fringe can be interpolated by analyzing the timing of the last two measurement crossings and the last reference crossing.



$$\frac{\theta}{2\pi} = R - M + \left(\frac{T_{m,i} - T_r}{T_{m,i} - T_{m,(i-1)}} \right)$$

Time interval analysis advantages:

- Relatively simple electronics processing.
- No unwrapping algorithm needed.

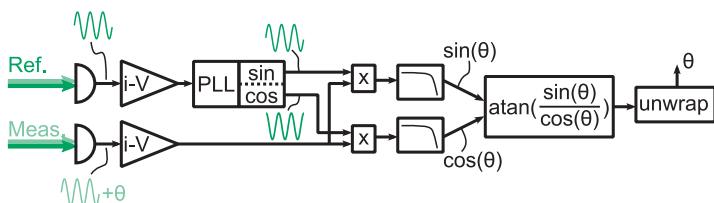
Time interval analysis disadvantages:

- Jitter in signals can cause false zero crossings.
- Signals are essentially averaged over an interval.

Lock-In Detection

Displacement interferometry signals are continuously time-varying phase shifts. **Lock-in detection** is specifically designed to generate matched sine and cosine signals of the phase difference and then compute an arctangent function to determine the phase θ using the trigonometric identity $\theta = \arctan(\sin \theta \cos^{-1} \theta)$.

The interference signals are detected and converted into electrical signals. The reference signal, which is stable at the heterodyne frequency with little deviation, is then used to generate a **phase-locked loop** (PLL), where the voltage-controlled oscillator in the PLL is designed to output complimentary sine and cosine signals of the locked phase. This generates a matched pair of signals with a stable 90-deg phase shift between them, in phase with the reference signal. The sine and cosine reference signals are multiplied with the measurement signal and filtered. Then, the arctangent is computed after dividing the two. Finally, the phase is unwrapped and converted to displacement.



The mathematical processing for the in-phase I and quadrature Q signals is as follows:

$$I = \cos(f_s t) \cos(f_s t + \theta) = \cos(\theta) + \cos(2f_s t + \theta)$$

$$Q = \sin(f_s t) \cos(f_s t + \theta) = \sin(\theta) + \sin(2f_s t + \theta)$$

Removed from low-pass filter

Lock-in detection advantages:

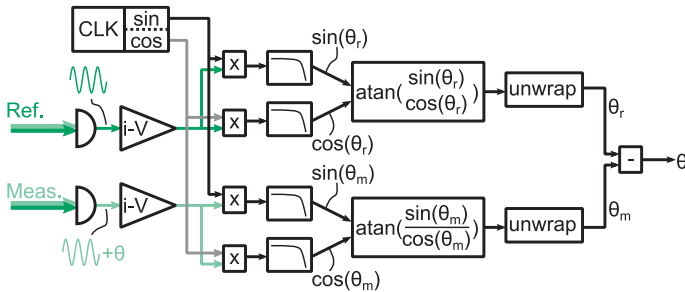
- Can be implemented in analog or digital electronics.
- Can perform at high speeds using FPGAs and DSPs.

Lock-in detection disadvantages:

- PLL must be stable to ensure signal fidelity.
- The phase must be unwrapped to prevent loss of fringe counts.

Discrete Fourier Transform

Using a **discrete Fourier transform** (DFT) algorithm to measure the phase between interference signals is similar to using lock-in detection. A matched pair of sine and cosine signals are generated and multiplied with the reference and measurement signals. After filtering, this generates matched pairs of sine and cosine signals at frequencies $(f_s - f_{\text{clk}} - \theta_m)$ and $(f_s - f_{\text{clk}} - \theta_r)$. Two arctangent functions are then used to compute the phase of each. Then, both signals are unwrapped from modulo- 2π signals. Finally, the difference between the two signals is computed, resulting in the measurement phase.



Typically, clock frequency f_{clk} is chosen such that the separation between $(f_s - f_{\text{clk}})$ and $(f_s + f_{\text{clk}})$ is sufficiently wide to filter the higher frequency. This effectively establishes an **intermediate frequency** in the DFT that is transformed into a continuously phase-shifting value with the arctangent and unwrap functions.

DFT advantages:

- Highly adaptable with different clock frequencies.
- Can be implemented in analog or digital electronics.
- Can perform at high speeds using FPGAs and DSPs.

DFT disadvantages:

- Two channels of high-speed arctangent computation and unwrapping are needed.
- Shifting the signals to intermediate DFT frequency can limit the Doppler velocity range.
- Typically, more digital resource space is required.

Special Interferometer Configurations

While the retroreflector single-pass and plane mirror double-pass interferometers represent the most common interferometers, other configurations exist for different types of measurements. These can be loosely collected into the following two groups:

1. Interferometers with different configurations

The traditional configurations are generally used for the majority of applications. However, in some cases, modified interferometer architectures can be used to enhance the measurement. This can include:

- enhancing optical resolution
- performing differential measurements

With modern signal processing techniques, enhancing optical resolution is generally not needed because **electronic phase interpolation** is more readily used to enhance resolution. Differential measurements can be advantageous because the reference datum can be more readily defined.

2. Interferometers measuring other degrees of freedom

DMIs measure phase changes in optical paths between measurement and reference arms in an interferometer. In most cases, the displacement is then inferred from the measured phase change. However, interferometers can be reconfigured to use the optical path change to signify a mechanism other than displacement. Some examples of these various mechanisms are

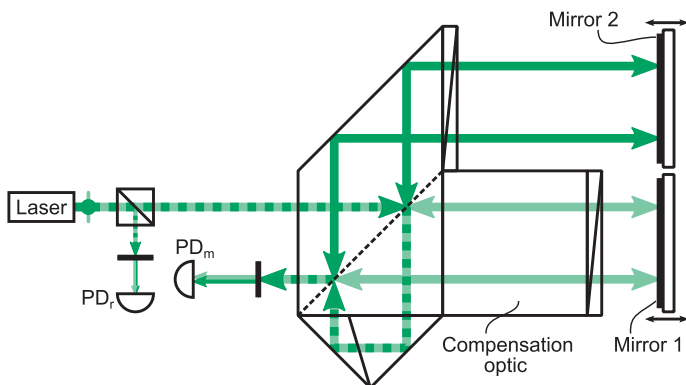
- angle measurements
- straightness measurements
- multiaxis and multi-DOF measurements
- refractive index changes

Either the measurement target is altered to make the measurement insensitive to displacement changes but sensitive to the particular DOF of interest, or the relative displacement of two points is measured, and the angle is computed by knowing the point spacing.

Differential Interferometer

Differential interferometers (also called **column reference interferometers**) are used when the displacement measurement must be made relative to another target. This is a common interferometer configuration used in lithography, where the displacement of interest is between the wafer stage and the lens column. A differential interferometer is essentially a PMI with two added components: an extra fold mirror and a compensation optic. A differential interferometer is essentially a PMI with two added components: an extra fold mirror and a compensation optic.

The compensation optic is used for nulling the OPD (between the measurement and reference arms) that is created by the additional glass path in the reference arm. Additionally, nonparallelism between the mirror-1- and mirror-2-surface normal vectors can be corrected using the compensation optic. Typically, two **Risley prisms** are used to change the angle between the measurement and reference arms, providing better overall alignment.



Differential interferometer advantages:

- Defined measurement and reference surfaces.
- Can compensate for initial misalignments.
- Used in multiaxis systems (plane mirror target).

Differential interferometer disadvantages:

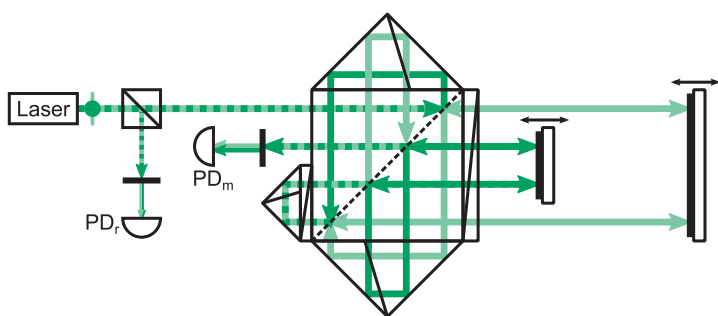
- Must account for angular misalignment between measurement and reference arms.
- Nonuniform refractive index changes increases noise.

Coaxial Differential Interferometer

In some systems, such as wavelength trackers, it is beneficial to have a **coaxial differential interferometer**, where the reference arm is coaxial with the measurement arm.

The measurement arm transmits through the PBS and passes through a QWP. It then reflects from the measurement surface (outside mirror) and passes back through the QWP, where a retroreflector (RR) is used to generate a second pass. After the second pass, instead of exiting the interferometer, a smaller RR and second QWP are used to laterally shift the beam and change the polarization. The measurement beam then reflects from the top RR and is directed out of the interferometer.

The reference arm initially reflects at the PBS, passes through the top RR, and is laterally shifted and rotated in the second QWP and smaller RR. The reference arm then makes two passes to the inside mirror, before overlapping with the measurement arm while exiting the interferometer. The two beams then interfere and are detected.

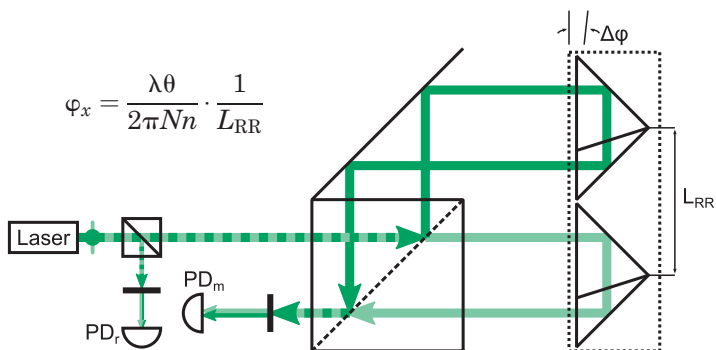


The top RR is used to ensure that the optical paths between the measurement and reference arms are nominally the same. This reduces the thermal sensitivity of the interferometer. The extra RR reflections and extra passes through the QWP can lead to more frequency mixing.

Angle Interferometer

Differential interferometers can be modified using a pair of RRs. This creates an **angle interferometer**, which measures angles instead of displacements. The simplest configuration uses the same configuration as a traditional single-pass interferometer except that a mirror directs the reference arm to the reference RR, which is housed with the measurement RR.

If both RRs (also called **angle optics**) displace, the net difference between the optical paths is zero. If the angle optics tilt in plane, then one optical path becomes shorter while the other becomes longer. When the measured phase is converted to physical displacement, the angle is determined by dividing by the spacing between RRs (small angle).



Wider spacing between RRs increases the angle sensitivity but also increases the spatial separation between beams. This leads to increased noise from refractive index fluctuations.

Angle interferometer advantages:

- System is insensitive to displacement and off-axis tilts.
- System has high angular sensitivity (nanoradian levels) with high angle range (hundreds of microradians).

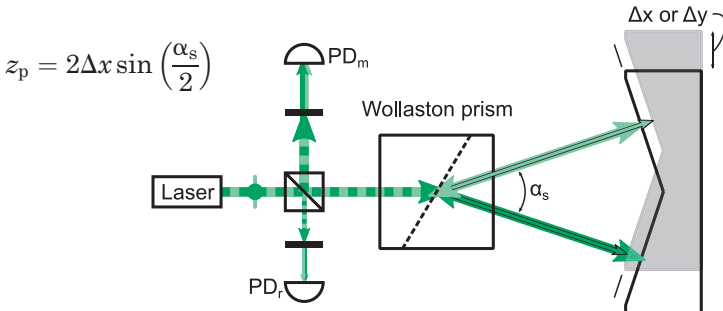
Angle interferometer disadvantages:

- System cannot be used in multiaxis systems.
- Large separation L_{RR} is needed for high sensitivity.
- Angle optics are large and heavy, affecting dynamic performance.

Straightness Interferometer

The displacement interferometer can be reconfigured as a **straightness interferometer** to measure straightness errors. Straightness errors are lateral changes in the position of a target in the directions mutually orthogonal to the translation direction.

The typical straightness interferometer uses a **Wollaston prism** and **straightness optics** at the interferometer and target. The Wollaston prism splits input light based on polarization with a nominal separation angle α_s between beams. The straightness optics then consists of two mirrors configured in a $180-\alpha_s$ -deg angle. If the straightness optics displaces, both optical paths change equally. If the straightness optics laterally shifts, one interferometer arm gets longer, while the other gets shorter. This optical path change is then detected and converted to straightness.



The output angle in the Wollaston prism is typically small, between 0.1 and 2 deg, leading to a straightness sensitivity of between $\sim 0.005\Delta x$ and $\sim 0.035\Delta x$.

Straightness interferometer advantage:

- Insensitive to displacement changes.

Straightness interferometer disadvantages:

- Low-sensitivity measurement, often dominated by refractive index fluctuations.
- Large straightness optics needed for longer distances.
- Straightness reference determined by mirror flatness symmetry deviation amplified by $1/\text{sensitivity}$.

Refractometry

Displacement interferometers are sensitive to target motion, laser frequency perturbations, and environmental fluctuations. **Environmental fluctuations** can cause errors in both the physical interferometer and in the optical signal. Changes in environmental parameters will affect the refractive index and appear as an error in the phase measurement. **Refractometry**, which is the study of measuring the refractive index of materials, is used to quantify the refractive index of the transient medium (air in most cases for DMI).

Methods for quantifying the refractive index:

- Monitor the temperature, pressure, and humidity during a measurement; typically, perform data post-corrections offline.
- Track refractive index changes using a separate instrument; tracking can be performed in real time.

Air refractive index calculations:

Temperature T and pressure P are large contributors to the refractive index of air, with smaller contributions from relative humidity (RH) and CO_2 concentration.

The **NIST Shop Floor** refractive index calculation is a simplified version of more complex versions and is intended to be used within two specific environmental parameter ranges. It can be used to obtain precise values of the refractive index of air, with low refractive index uncertainty $u(n)$.

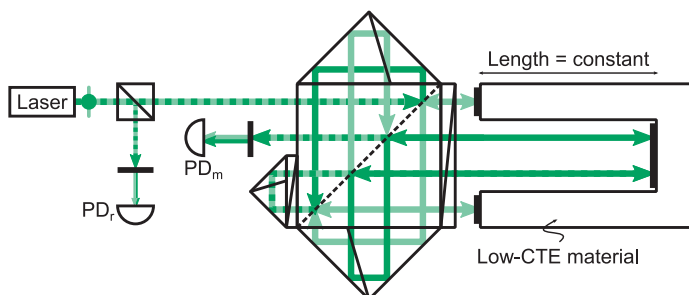
$$n = 1 + \frac{7.86 \times 10^{-4}P}{273 + T} - 1.5 \times 10^{-11}RH(T^2 + 160)$$

Parameter	Range 1	Range 2
T [°C]	0–35	19.5–20.5
P [kPa]	50–120	90–110
RH [%]	0–100	0–70
CO_2 [ppm]	300–600	350–500
$u(n)$	1.5×10^{-7}	5×10^{-8}

Wavelength Tracking

Using equations for measuring refractive index errors limits options for realtime correction due to sensor integration time and sampling bandwidth. If the initial refractive index is known, wavelength or refractive index trackers can be used to measure the relative change in refractive index.

A common **wavelength tracker** uses a coaxial differential interferometer configuration that has a fixed, defined distance between the measurement and reference arms. The arms measure a fixed cavity made from low-coefficient-of-thermal-expansion (CTE) materials. If the length is constant between measurement arms, then changes in the interference are driven by changes in refractive index.



As the cavity length L_c is increased, the change in refractive index becomes more sensitive. However, no material has zero CTE nor is infinitely stiff. Temperature and pressure changes can cause L_c to change, although specific materials can be chosen to mitigate these errors.

$$\theta = \frac{2\pi n N L_c}{\lambda} \rightarrow \Delta n = \frac{\Delta \theta \lambda}{2\pi N L_c}$$

Wavelength tracking advantages:

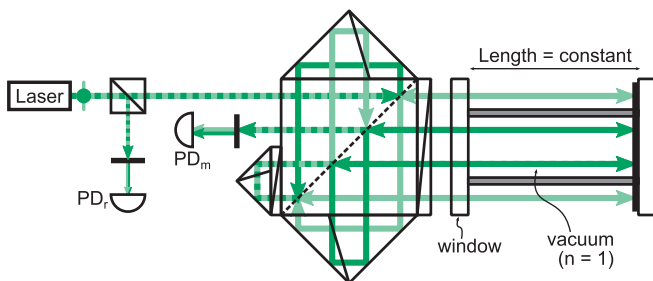
- Can measure high-speed refractive index change.
- Can measure and correct refractive index in real time.

Wavelength tracking disadvantages:

- Separate measurement needed for absolute refractive index.
- Longer cavity needed for higher sensitivity; more susceptible to environmental changes.

Refractive Index Tracker

Another interferometer variant for tracking changes in refractive index is a **refractive index tracker**. Like the wavelength tracker, it also uses a coaxial differential interferometer in which the center beams travel through a fixed cavity in vacuum, while the outside beams travel along the same cavity but in air. This interferometer is intended to have all four beams pass through a common window and reflect from the same mirror surface. Provided that the cavity is stable, the difference between interferometer arms is the refractive index.



Refractive index trackers are different from wavelength trackers in two ways: (1) the measurement is compared to vacuum, where $n \equiv 1$, and (2) the cavity length stability is less critical when calculating the measurement uncertainty. This latter distinction arises from the 1×10^{-4} difference between air and vacuum refractive indices. The measurement uncertainty can be lower because the refractive index is compared to a defined value.

$$\theta = \frac{2\pi(n-1)NL_c}{\lambda} \rightarrow (n-1) = \frac{\theta\lambda}{2\pi NL_c} \rightarrow \Delta n = \frac{\Delta\theta\lambda}{2\pi NL_c}$$

Refractive index tracking advantages:

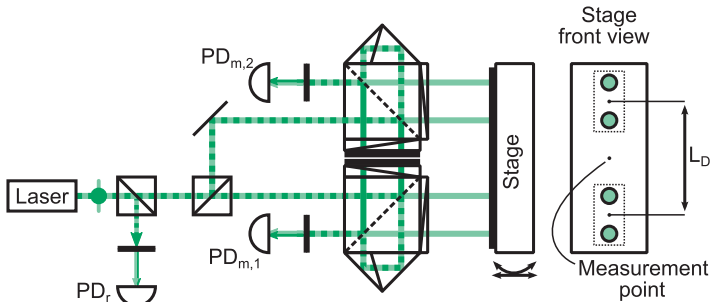
- Uses direct comparison with defined refractive index value.
- Has lower measurement uncertainty than wavelength trackers using the same materials/parameters.

Refractive index tracker disadvantages:

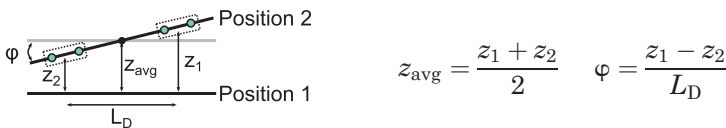
- Uses separate measurement for absolute refractive index.
- Inaccuracies in window geometry can cause errors.

Multiaxis Systems

Multiple single-axis interferometers can also be used to create **multiaxis systems**, which measure multiple DOFs of a stage. A simple example is two PMIs measuring the same stage with a known, constant spacing L_D between the centers of the two interferometers. Using this configuration, both stage displacement and changes in angle can be measured.



Additional **beam-steering optics** are needed prior to the interferometers to split and direct the input beam into the interferometers. Although multiple axes are measured, only one reference signal must be generated from the laser. Typically, the overall displacement is determined by the average of the two interferometer signals, while the angle is determined by the difference divided by the separation length.



$$z_{avg} = \frac{z_1 + z_2}{2} \quad \phi = \frac{z_1 - z_2}{L_D}$$

Multiaxis interferometer advantages:

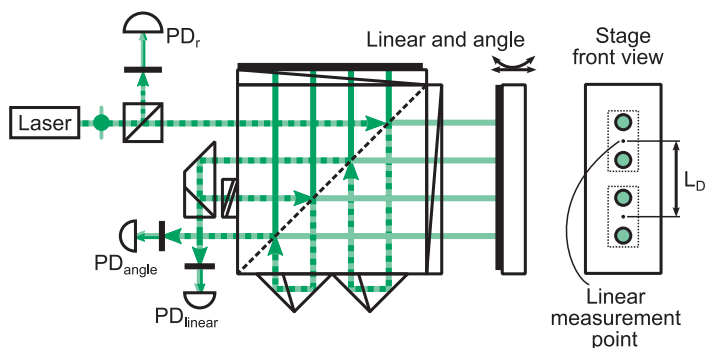
- Can measure multiple DOFs of a moving target.
- Has a single laser and optical reference for all axes.

Multiaxis interferometer disadvantages:

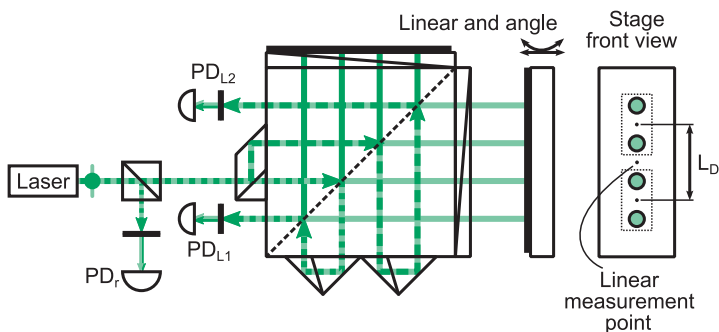
- Target mirror surface must accommodate more beams.
- Coupled alignment between axes makes it subject to beam-steering optical misalignments and drift.

Multi-DOF Interferometers

Multi-DOF interferometers can be used to measure several DOFs in one system. Typically, these systems are designed such that only a single input beam is needed to supply several interferometer arms. Examples of multi-DOF interferometers are: combined linear–angular interferometers (shown directly below) or linear–straightness interferometers. Some configurations are a compact version of several single-axis PMIs. These behave similarly to two individual interferometers.



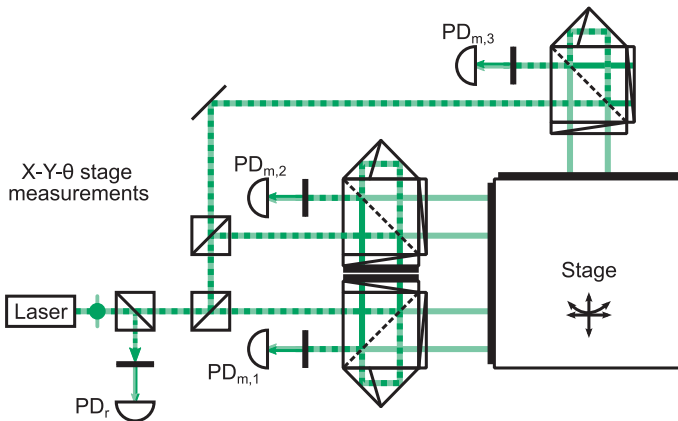
Other interferometer layouts can be a modified configuration. In these cases, one axis generally measures the main linear translation, and the other axis measures deviations from that axis, as in the interferometer shown below. For these interferometers, it is critical to know the location of the linear axis measurement point because this must be aligned with the translation axis through the **functional point** to reduce **Abbé errors**.



X-Y-Theta System

A common configuration for precision systems is a planar stage that has large motions in two DOFs and small rotations about the mutually orthogonal axis. These systems are sometimes referred to as **X-Y-theta systems**, which is not the same coordinate system as the beam coordinate system.

For systems with planar motion, PMIs are preferred because they are (nominally) insensitive to orthogonal motion. The interference from $PD_{m,1}$ and $PD_{m,2}$ is averaged to determine the X displacement, and $PD_{m,3}$ determines the Y displacement. The ideal measurement point coincides with the center of the stage, which is the location of the **functional point** on most stages. This alignment detail helps reduce **Abbé errors**.

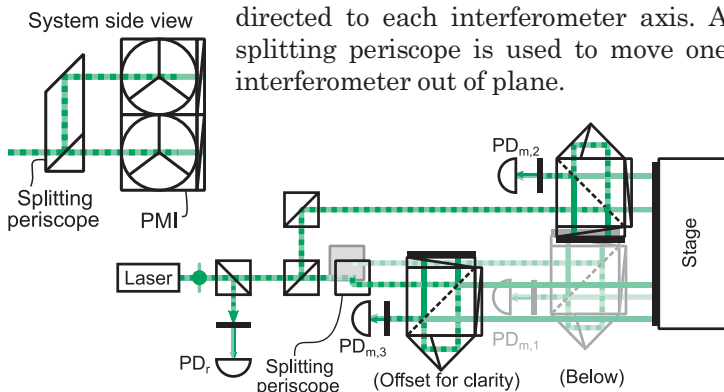


In this configuration, care must be taken to normalize the same power into each interferometer axis. The first BS after the reference should transmit 33% and reflect 67%. The second BS should then transmit 50% and reflect 50%. This ensures that one-third of the input light enters each interferometer axis.

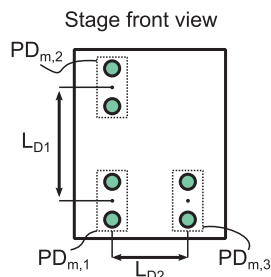
Non-orthogonality between the $PD_{m,1}$ and $PD_{m,2}$ axes with $PD_{m,3}$ will lead to **crosstalk**, which is a potential error.

Tip-Tilt-Z System

Another common three-interferometer configuration is used to measure one linear displacement and two angular rotations and is commonly called a **tip-tilt-Z system**. Like the X-Y-Theta system, correct splitting ratios are needed with the BSs to ensure that sufficient power is directed to each interferometer axis. A splitting periscope is used to move one interferometer out of plane.



The location of the center point for the Z measurement can be arbitrary, depending on whether multiple interferometer measurements are averaged. This location can be tailored to minimize Abbé errors. If one interferometer measures the main Z displacement, then differential measurements between the other two interferometers and the main interferometer are used to measure the angles. If multiple interferometers are used, then the centroid location between the geometrical centers is used as the Z displacement. The configuration here has the beams positioned in an “L” shape, but that can be changed depending on the desired measurement locations.



If there are no other orthogonal motions, then PMIs do not need to be used. In this case, the number of interferometer components can be reduced.

Setup and Alignment Techniques

Interferometers can be difficult to align if proper care is not taken to address potential error sources, such as polarization alignment, beam pointing, spurious reflections, cosine error, hitting edges on components, edges on retroreflectors, etc. Several tools can aid with alignment, even though they are not used in the final system. Additional spare components (mirrors, retroreflectors, waveplates, posts, etc.) can also be useful, depending on the interferometer configuration.

Irises (or **apertures**) are used when needing to block light or to establish an aperture. Employing vector alignment, several irises can be used for aligning two beams to be coaxial. Typically, two to three irises are needed for alignment.

Polarizers are typically mounted on a rotation stage to rotate the polarization through the azimuthal angle. They are used to selectively block different polarizations and check for beam leakage.

An optical **power meter** is useful for determining the minimum or maximum intensity of a beam. It is used for aligning waveplates, polarizers, and fiber components. Power measurements are more sensitive when minimizing the optical power than when maximizing the optical power.

A **photodetector** is commonly used to measure the amount of fringe contrast, beam leakage, and ghost reflection.

A **bubble level** helps to nominally align platform mounts for beamsplitters and prisms.

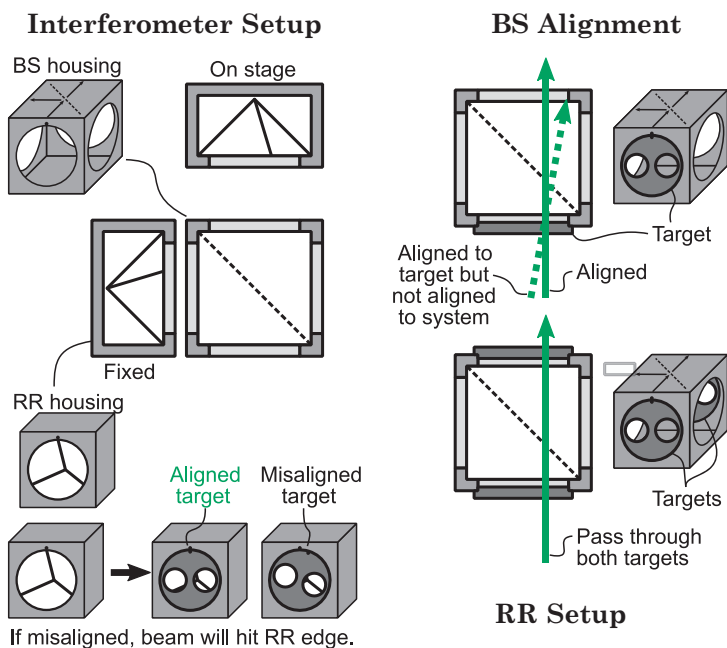
For very precise alignment, a **CCD camera** or **position-sensitive detector** (PSD) can be used to measure beam positions and calculate their offset. This is useful for ensuring coaxial beams and limiting cosine error.

Commercial Interferometer Alignment

Commercial interferometer systems usually have dedicated alignment instructions, depending on the interferometer configurations. These instructions often include alignment markers to assist in the process. Targets provide **point alignment**. Two markers are needed to ensure **vector alignment**.

Commercial interferometers typically house optical components in a metal cage for the following reasons:

- Metal housing protects the delicate optics.
- A metal cage provides holes for assembling optical interferometers.
- Alignment targets can be fixed to the housing.

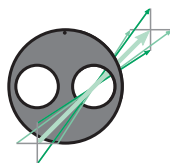


Targets usually have a marker on the edge for aligning the rotational (or azimuthal) angle of the beam. This marker helps to keep beams from hitting the edges of retro-reflectors and right angle prisms. Targets can have multiple markers that correspond to different interferometer configurations.

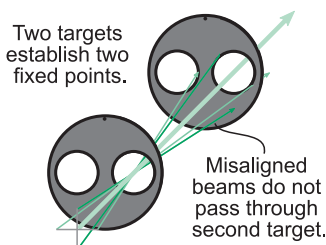
Vector Alignment and Breadboard Alignment

Targets on commercial interferometer optics establish a point through which the beam passes. Beams that are not aligned to the interferometer can still pass through the target. Two points (from two targets) are needed to align a beam along a spatial vector. Only those optical beams that pass through both targets are coaxial.

Point alignment



Vector alignment



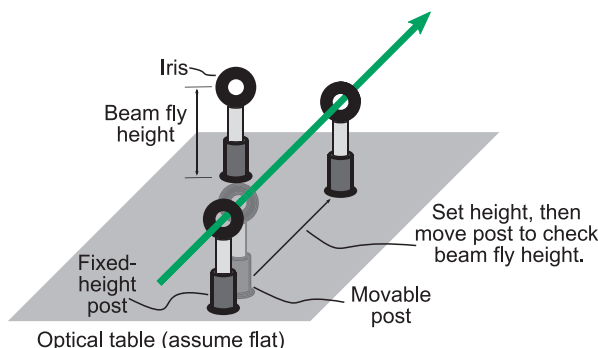
Optical breadboards are commonly used for research applications, where either custom configurations are needed or a simple test is required to verify a principle. Aligning on an optical breadboard is often more challenging than aligning commercial interferometers because many more factors must be considered, such as:

- Optical components typically must be mounted on rotation mounts to provide sufficient DOFs to align the component.
- Improper mounting can cause **stress birefringence**, which adversely affects polarization components.
- Improper mounting can cause unwanted deformations, adding to **wavefront distortion** and increasing crosstalk errors.

A series of common, repetitive techniques can be used to aid in alignment. Typically, these are employed iteratively, until sufficient alignment is achieved.

Beam Fly Height

Breadboard interferometers use the optical table as a reference surface where the beam is aligned at a fixed height above the table. An iris mounted on a post can be set at the desired **fly height**. A second iris mounted on a magnetic post is adjusted to match the fixed iris' fly height. Then, this movable iris can be placed anywhere on the breadboard and continuously used to correct and adjust the beam fly height after the beam transmits through components or reflects from mirrors. The movable iris is sometimes referred to as the **height reference**.



It is useful to establish two height references that can be independently placed, especially for beamsplitters. The input beam and output beam should be aligned at the same height; otherwise, the component will be tilted.

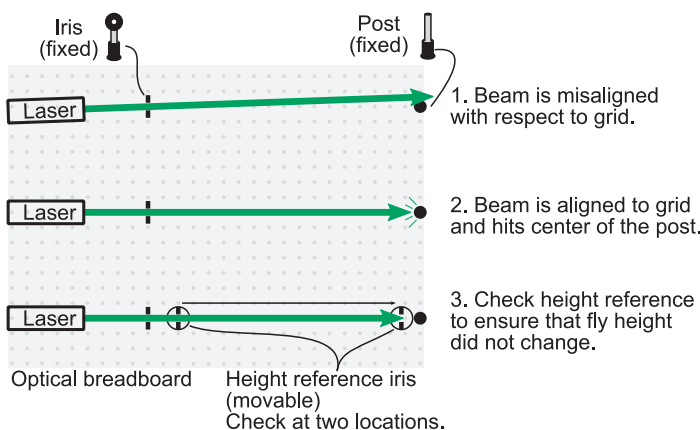
Orthogonal alignment is critical to minimizing polarization errors in interferometers. Mirrors are typically specified for 0- or 45-deg alignment. When not used at these angles, mirrors can rotate and mix polarization states. The optical breadboard creates one datum surface. The purpose of the beam fly height is to establish an offset, parallel datum that coincides with the stage/component to be measured. The hole grid on the breadboard is used to generate the second and third datums. This is accomplished by aligning beams at the fly height along the grid, thus ensuring that beams are nominally orthogonal.

Grid Alignment

Whenever possible, optical beams should be aligned to the **breadboard hole grid** at the same fly height to reduce **polarization scrambling**. Simple techniques can be used to align optical beams to the breadboard grid.

A collimated laser beam is aligned to the grid using a fixed iris, a fixed post, and the height reference. The grid line is selected, and the iris is fixed at the input end, with the post at the farthest distance. A longer distance between the iris and post increases the angular sensitivity. The following steps can be taken to achieve the desired grid-to-beam alignment:

- (1) Align the laser beam through the iris that is directed toward that post.
- (2) Rotate and laterally shift the laser until the input beam passes through the iris and reflects from the center of the fixed post.
- (3) Check the beam fly height using the height reference iris. Iteratively adjust the laser's height, position, and orientation until the beam passes through the iris, reflects off of the fixed post, and passes through the height reference near the fixed iris and near the fixed post.

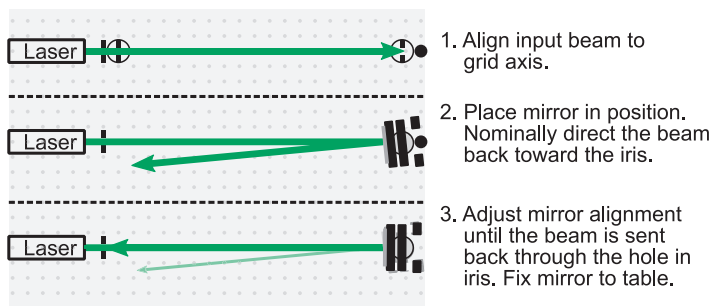


This **alignment technique** is a common base for many other alignment techniques. Most alignment processes are a combination of iteratively applied techniques.

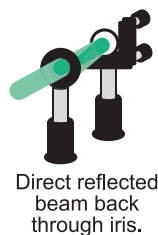
Normal Mirror Alignment

Mirrors are often aligned with their surface normal vector collinear with the optical beam in the displacement interferometer. This could be a mirror on the target or a mirror in the reference arm. Mirrors at an angle can cause measurement errors in polarization, beam orientation, and fringe contrast.

After establishing the fly height of the optical beam, the mirror should be placed in the desired location, leaving the initial iris in place. The mirror should then be adjusted until the reflected beam is directed back through the center of the iris. Even if the input beam is not aligned to the center of the iris, the mirror can still be aligned, as long as the reflected beam hits the center of the iris.



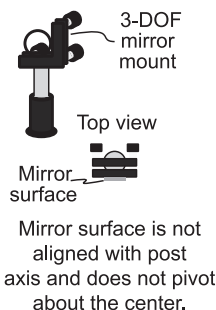
Retroreflectors and prisms that add a **lateral offset** to the reflected beam can still be aligned using this method. For those components, there is typically a low-power **ghost reflection** from the first surface that will reflect some light.



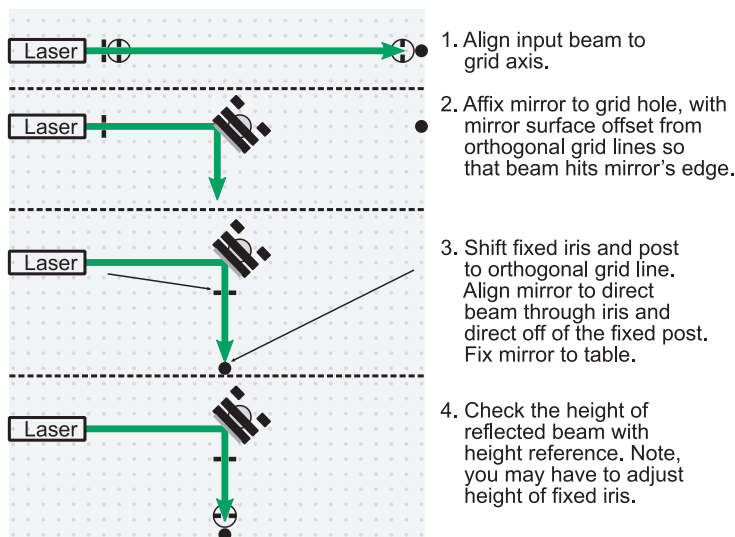
Depending on the situation, it may be desirable to use this technique to ensure that ghost reflections do not reflect back down the beam line. These ghost reflections can potentially destabilize the laser, causing frequency drift in the output optical beam.

45-deg Mirror Alignment

Mirrors are used to direct the optical beams on the breadboard. Common **mirror mounts** have either two or three fine-pitch screws for adjusting in two or three DOFs. On these mounts, the mirror surface is often offset from the central mounting post. This means that the reflected beam will not align to the orthogonal breadboard grid. Extra steps are required to align the reflected beam to the grid.



The following steps can be taken to align an **offset mirror** at 45 deg in order to direct the beam in an orthogonal direction:

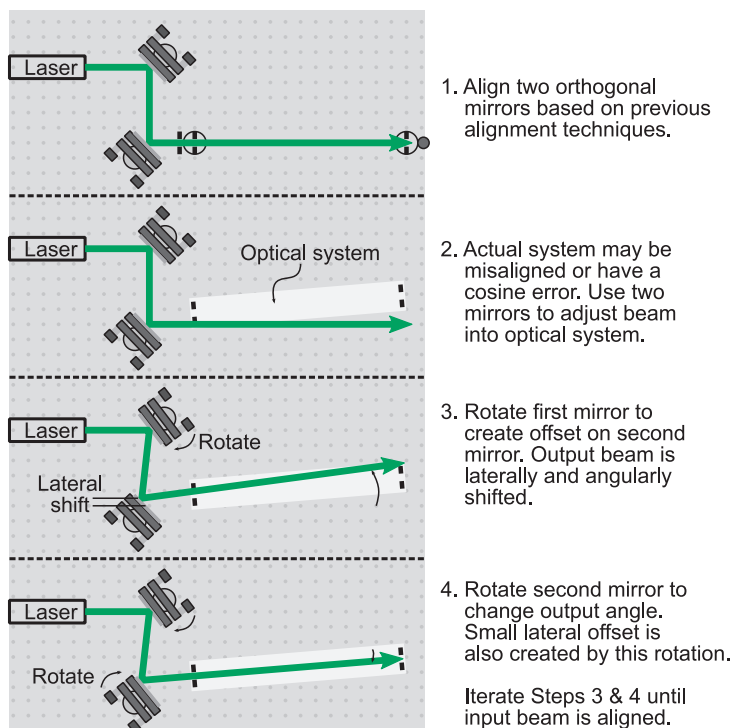


Generally, a combination of lateral motion and rotation is needed to align the input beam off of the mirror, through the iris, and off of the post. Mirror mounts with 3-DOF adjustments (tip, tilt, and Z) have the additional lateral DOF needed to avoid shifting the entire mirror and mount. If the mirror is aligned at 45 deg to within a few degrees, the polarization mixing and rotation effects should be minimal.

Mirror Steering

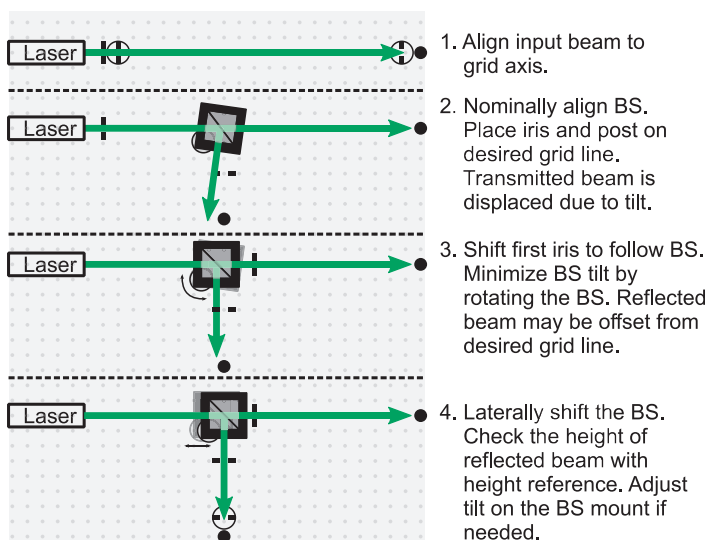
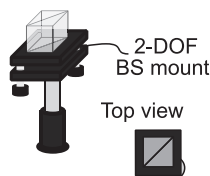
Four degrees of freedom and two mirrors are generally needed to direct a collimated optical beam into an optical system. The fifth degree of freedom, rotation about the beam axis, is usually manipulated with polarization optics. The sixth degree of freedom is the position along the beam path and has minimal importance for beam steering with collimated beams.

Fine adjustments to an optical beam can be performed with two mirrors, each on a **2-DOF tip-tilt mount**. The first mirror is used to change the location at which the incident beam reflects on the second mirror. The second mirror is used to adjust the output angle. The first mirror is used to align to the first iris, and the second mirror to align to the second iris.



Beamsplitter Alignment

Aligning a beamsplitter is similar to aligning a mirror at 45 deg on the breadboard. Beamsplitters should be aligned with the splitting face at 45 deg relative to the input beam, ensuring an orthogonal output beam. This is especially important for a PBS because misalignments can cause mixing between the polarization states. The following steps can be used to align the beamsplitter:

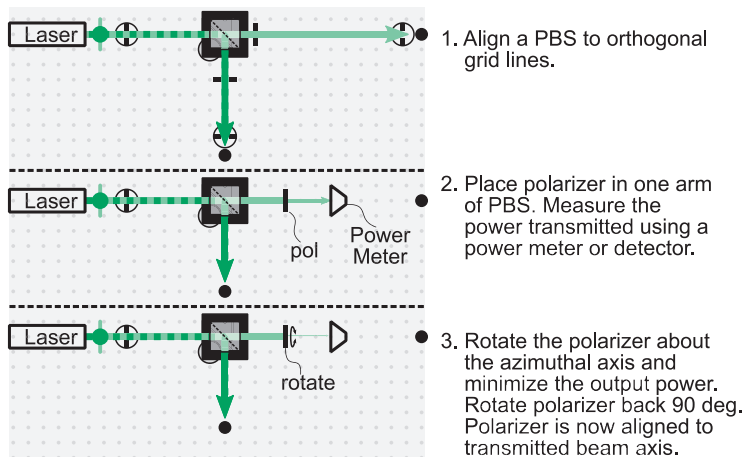


Iterate Steps 3 & 4 until BS is aligned.

PBS alignment is slightly different from **BS alignment** because, in the former, the efficacy of the polarization separation is dependent on the alignment with the splitting surface. Changes in the mount roll axis (with respect to the input beam) cause changes in the output beam height. The bottom surface of the PBS might not be orthogonally aligned to the desired splitting axis. This means that the ideal height alignment does not necessarily coincide with the ideal alignment for polarization splitting. For precise applications, a **polarimeter** can be used to measure the output beam when aligning the system.

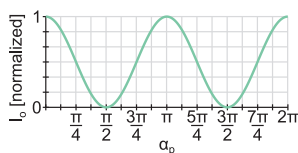
Polarizer Alignment

The simplest method for **aligning a polarizer** uses a PBS as the base component. First, align the PBS with the splitting surface at 45 deg relative to the input beam. Next, place the polarizer in one arm of the PBS outputs and measure the optical power. Rotate the polarizer in the azimuthal direction to minimize the optical power on the detector. When the light is completely blocked, the polarization axis is aligned to the arm that is opposite to the arm that was blocked. The polarizer can then be rotated on a rotation mount to the desired angle.



Linearly polarized light that is blocked by a polarizer obeys Malus' law:

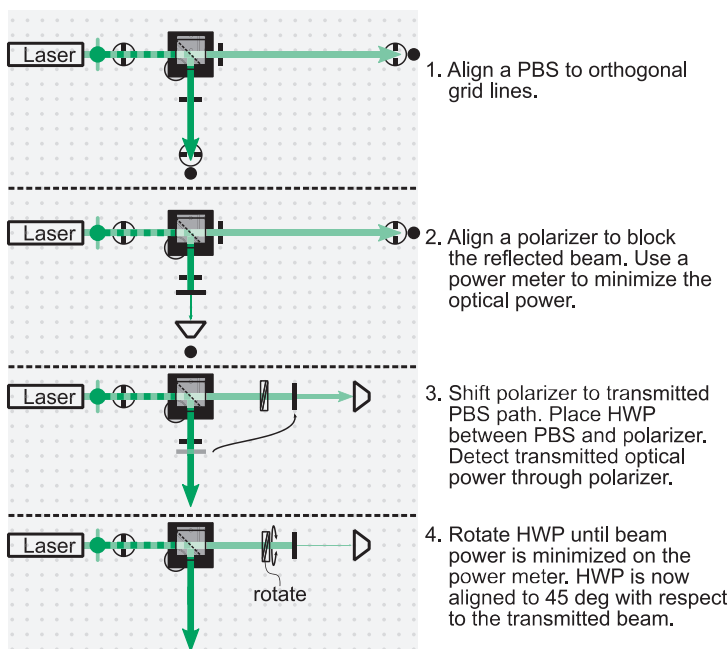
$$I_o = I_i \cos^2(\alpha_p)$$



When aligning and using a power meter as feedback, the measurement is more sensitive to light that is almost blocked compared to this same sensitivity when maximizing the optical power. It is easier to measure a 10-nW change when the nominal power is almost zero than to sense a 100-nW change on tens or hundreds of microwatts.

45-deg HWP Alignment

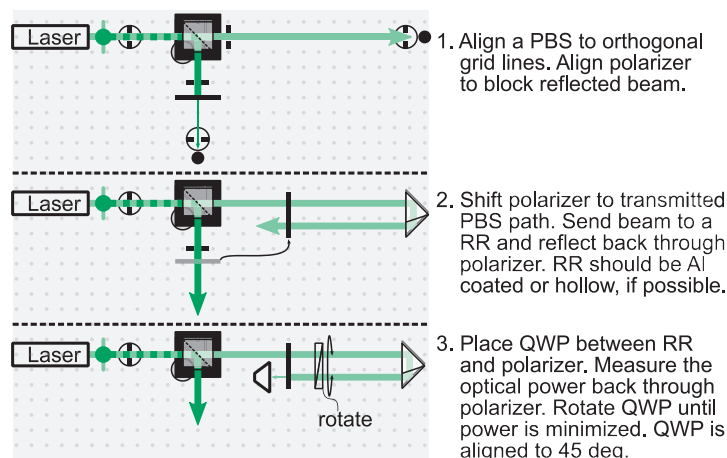
Half-waveplate alignment uses a PBS, a polarizer, and a power meter to align the HWP to 45 deg with respect to a linearly polarized input beam. First, align a PBS to the breadboard; then, align a polarizer to block the reflected beam. Add the HWP in the transmitted PBS arm, then move the polarizer to block the light after the HWP. When the optical power is minimized after the HWP, the output beam will have rotated 90 deg from the input beam. Because HWPs rotate light based on twice the difference angle between their fast axis and input light's axis, a 90-deg rotation in polarization means that the HWP's fast axis is aligned at 45 deg.



Waveplates are generally slightly thinner than a quarter or half wave. An oversized waveplate can never retard the light exactly. An undersized waveplate can be tilted to change the apparent thickness, enabling better alignment.

45-deg QWP Alignment

Quarter waveplates are commonly used in displacement interferometry to rotate the polarization of a beam by 90 deg after reflecting from a mirror or retroreflector. A PBS, polarizer, power meter, and a retroreflector or right angle prism are needed. A slightly tilted mirror can be used, but the tilt will impart some polarization rotation.



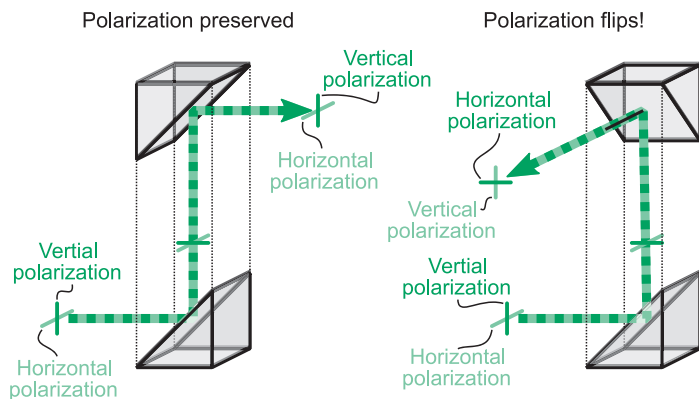
As with HWP's, the QWP thickness is typically undersized by a small amount, so that it can be tilted to achieve better alignment. Tilting a HWP or QWP has the added benefit of reducing ghost reflections that would otherwise propagate back along the beam path. Tilting causes the ghost reflections to be reflected at an angle, limiting their impact on interference signals and laser stability.

A coated or hollow RR is preferable to a total internal reflection (TIR) RR. A TIR RR has non-normal reflections that cause unwanted polarization rotations and mixing. Even perfectly linearly polarized input light will exit with some ellipticity, causing errors in the aligned QWP. The polarization rotation in an RR is strongly dependent on the imaginary component of the reflecting surfaces' refractive index, which is higher in coated and hollow RRs.

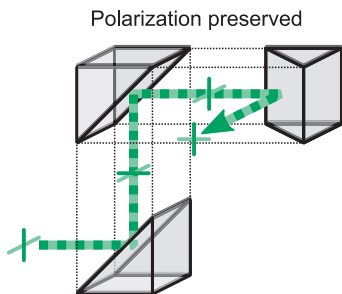
Polarization Flipping

The number and alignment of the mirrors used to direct the source beam into the displacement interferometer can cause polarization flipping. **Polarization flipping** occurs when the polarization of the desired optical frequency is unintentionally aligned to its orthogonal counterpart.

When a beam is directed in the same plane using two successive orthogonal mirrors, the input polarization is preserved. If the beam is directed in three orthogonal directions using only two mirrors, the vertical and horizontal optical frequencies swap polarization states.



When the desired optical frequency is in the wrong polarization state, the optical frequency sent to the moving mirror is incorrect, leading to an error that scales at a fractional displacement of $f_s/f_1 \approx 1 \times 10^{-8}$. For long displacements, this error can be significant.



Polarization flipping can be corrected by adding a **steering mirror**. The added mirror creates two pairs of in-plane motions rather than steering along three orthogonal directions in one pair.

In-line Beam Steering

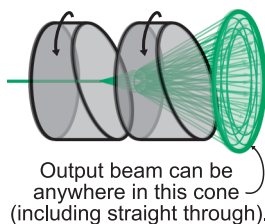
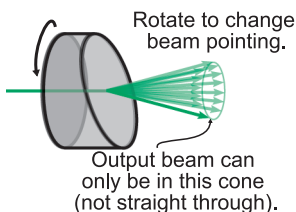
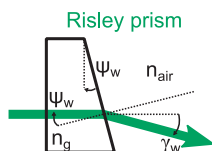
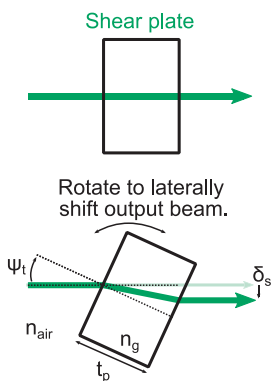
Directing the input beam into an interferometer using a series of mirrors is not always possible due to spatial constraints. **In-line beam steering** is often used to save space. **Shear plates** and **Risley prisms** are used to make small adjustments to the beam pointing direction. These can be used in line, minimizing the space needed to adjust a beam. This method is useful in multiaxis systems, where the alignment into several interferometers is coupled.

Snell's law:

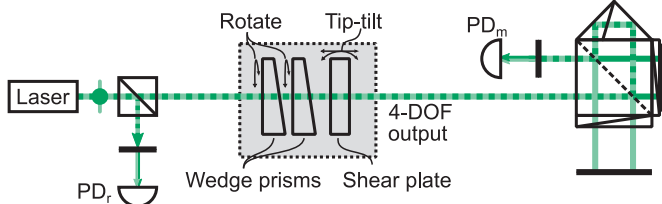
$$n_i \sin(\psi_i) = n_o(\psi_o)$$

$$\gamma_w = \sin^{-1} \left(\frac{n_g}{n_{\text{air}}} \sin \gamma_w \right) - \psi_w$$

$$\delta_s = t_p \sin \psi_t - \frac{t_p n_{\text{air}} \sin 2\psi_t}{2n_g \sqrt{1 - \left(\frac{n_{\text{air}}}{n_g} \right)^2 \sin^2 \psi_t}}$$



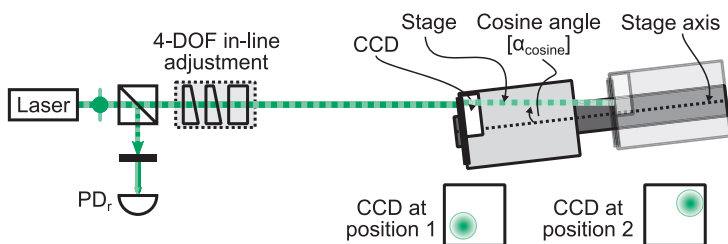
4-DOF In-line alignment system



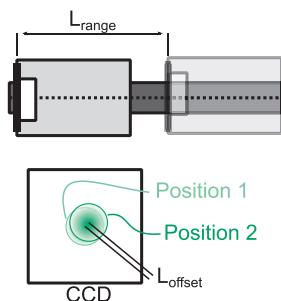
Cosine Error

Displacement interferometers can measure accurate displacement information while still inaccurately measuring the displacement of their intended target. This discrepancy results from a misalignment between the target motion axis and the interferometer measurement axis, commonly called **cosine error**. Cosine errors always cause the interferometer to measure a shorter displacement than the actual target displacement.

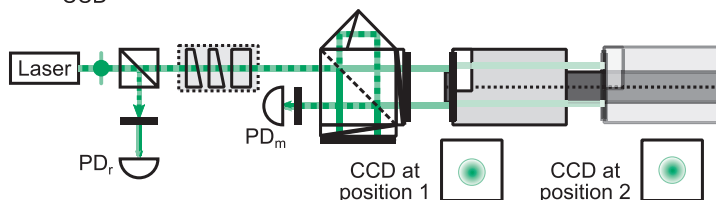
Cosine error is measured using a CCD camera or PSD on the target. The cosine error is determined by measuring the lateral shift on the CCD/PSD over the range of the target.



$$\alpha_{\text{cosine}} = \cos^{-1} \left(\frac{L_{\text{offset}}}{L_{\text{range}}} \right)$$

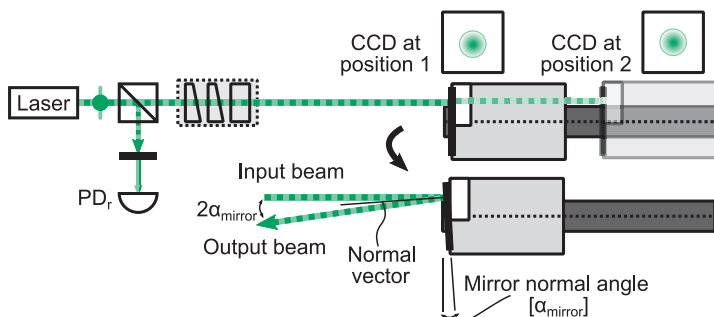


Adjustment of the target or mirrors, or a 4-DOF in-line adjustment system is used to minimize the cosine error of the main source beam to the target. Then, the interferometer is placed in the path of the source beam and is nominally aligned to the stage.

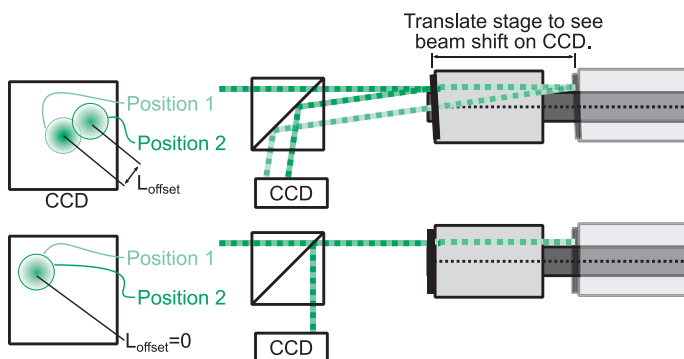


Cosine Mirror Alignment

For plane mirror targets, even when the beam alignment cosine error is minimized, a **cosine error** may still be present from the **mirror alignment**. This error occurs when the normal vector of the mirror is not parallel to the input beam axis. The beam reflecting from the stage returns at an angle, causing it to travel farther than it would if the beam were aligned.



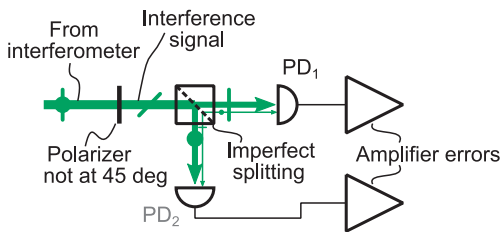
The mirror normal vector can also be determined using a CCD or PSD. This alignment procedure is dependent on the initial input beam alignment and should be performed after the cosine error is minimized. By directing the beam back through a BS and using a CCD or PSD, the beam will displace as the stage is translated. The reference can be tilted, and the stage translated to reduce offset. Once the offset is minimized, the mirror's normal vector will be nominally aligned. Increasing the distance between the mirror and the CCD increases the sensitivity.



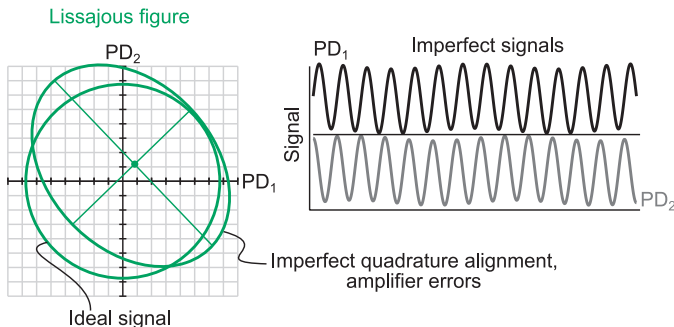
Lissajous Figure

Homodyne interferometers often have errors from imperfect **quadrature detection**. The sources of these errors can be from several components and can potentially change over time from drift and other temporal effects. The common sources of this type of error are:

- Interference polarizer being misaligned.
- Imperfect splitting and beam leakage in components.
- Different photodiode characteristics.
- Transimpedance amplifier errors such as gain, noise, and drift.

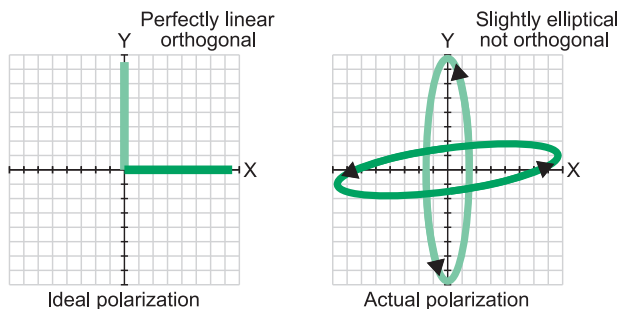


Plotting quadrature outputs with respect to each other should result in a so-called **Lissajous figure**. If the signals are perfect, the plot should appear as a circle. If errors are present, the Lissajous figure will appear as an ellipse. These errors can be corrected by fitting the ellipse and performing a **Heydemann correction**. Typically, the ellipse is fitted with a least-squares routine, and a correction factor is applied to both PD₁ and PD₂ to account for these errors. Not correcting these errors will lead to errors on the scale of nanometers to tens of nanometers, similar to periodic errors in heterodyne systems.



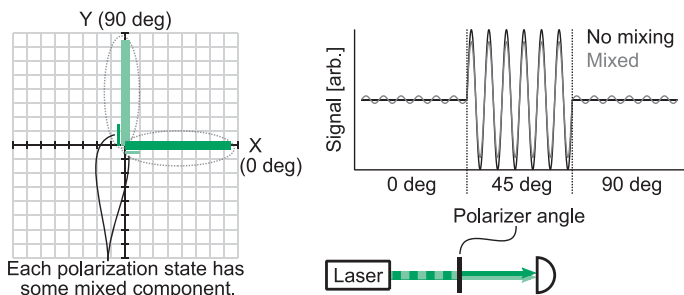
Source Mixing

Heterodyne laser sources typically do not output perfectly linear and orthogonal polarization states. **Source mixing** results from the output of each beam being slightly elliptical and not mutually orthogonal. The sources of this effect are imperfect optics and imperfect alignment.



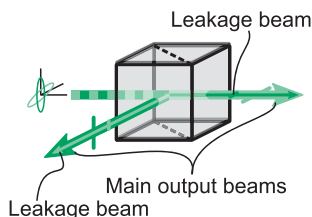
Source mixing has the following impact on DMI systems:

- It is impossible to perfectly split the two polarization states using polarization optics, due to their inherent inaccuracy (even near-perfect components).
- There is always a small part of one optical frequency aligned to the same polarization state as the other optical frequency. This means that a small interference signal will exist, even when the other polarization state is blocked.
- Source mixing leads to **periodic error** in the measurement. Periodic error is a cyclical error as a function of target position on the (typically) 1- to 5-nm level.

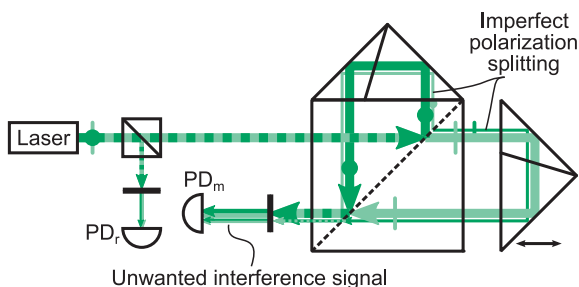


Beam Leakage

Beam leakage is a further consequence of source mixing in displacement interferometry. When a beam with source mixing passes through a PBS, the transmitted beam contains mostly the intended optical frequency, with a small amount of the other optical frequency. Likewise, the reflected beam contains a small component of its unintended optical frequency. In addition, the non-orthogonality of a source-mixed beam combined with imperfect splitting ratios between polarization states means that there is usually a slight difference in the amount of leakage to the transmitted and reflected arms.



When beam leakage occurs in an interferometer, the leaked optical frequencies still propagate coaxially with the main beams. These beams then interfere with the main beams and each other at the main polarizer before the detector, generating two additional signals.



The two extra interference signals are **first-order periodic error**, which results from interference between a leakage beam and a main propagating beam, and **second-order periodic error**, which results from interference between the two leakage beams.

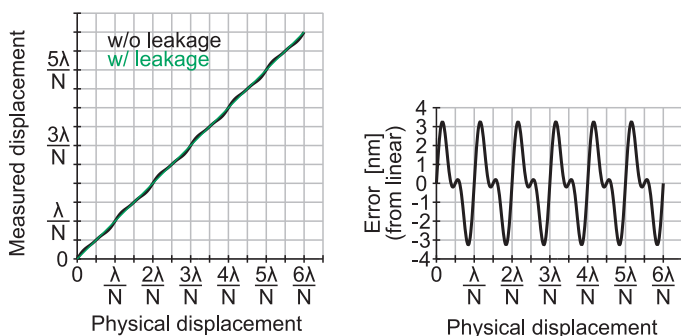
Periodic Error

Periodic error is a signal processing error in which the assumed phase relationship with physical displacement is linear. In practice, the **leakage beams** cause this assumption to be incorrect because the relationship becomes nonlinear. The measurement interference signal has two additional terms, driven by γ_1 and γ_2 , the amplitudes of first- and second-order mixing.

$$I_m \propto \cos(2\pi f_s t + \theta_m)$$

↓

$$I_m \propto \cos(2\pi f_s t + \theta_m) + \gamma_1 \cos(2\pi f_s t) + \gamma_2 \cos(2\pi f_s t - \theta_m)$$



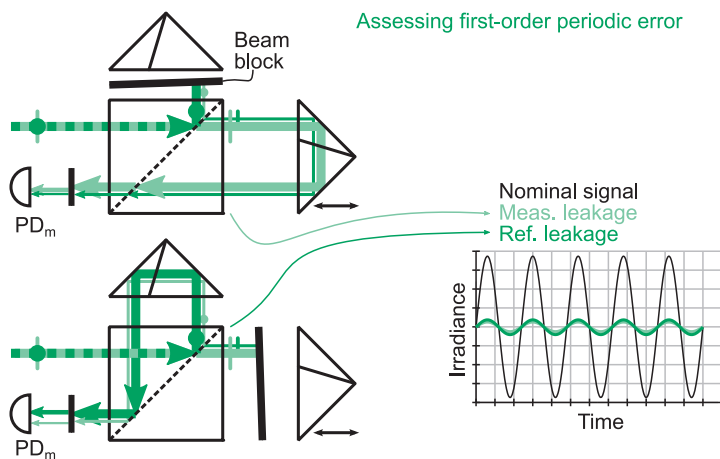
Periodic error attributes are described below:

- Periodic error does not scale with measured displacement. It is a function of source mixing and alignment that causes a predictable error superimposed over the nominal displacement.
- Periodic error is a function of interferometer geometry and the source wavelength, appearing at the first and second spatial harmonics as the target displaces. For example, if $\lambda = 632.8$ nm and $N = 2$, then the first harmonic appears every 316.4 nm displaced, and the second harmonic every 158.2 nm.
- Each periodic error component (first or second) is caused by different mixing errors and alignment.

Assessing Periodic Error

Source mixing, beam leakage, and alignment all play a critical role in contributing to periodic error. Slight changes from one interferometer to another can cause several nanometers of difference in the amplitude of the periodic error.

Periodic error can be assessed by selectively blocking one arm of the interferometer and measuring the interference on the detector. Then, if possible, the other arm is blocked and the interference is measured again. If interference is detected in either case, this interferometer will have periodic error. The amount of interference when one arm is blocked (leakage interference) determines the amount of first-order periodic error.



Leakage interference can be used to adjust the interferometer and beam alignment in order to minimize periodic error. This method cannot be used to directly measure second-order error. However, reducing the first-order error generally reduces the second-order error.

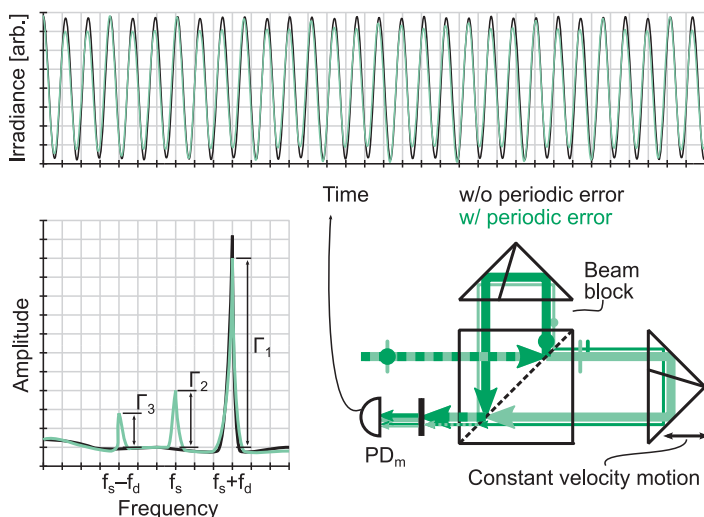
This method can also be used to determine whether ghost reflections are affecting the measurement. Blocking the beam at selective points can isolate the origins of unwanted ghost reflections.

Quantifying Periodic Error

Two simple methods are used for **quantifying periodic error**: The first method uses spectral data of the measurement interference signal during a constant velocity motion. The second method uses spectral analysis based on the spatial data during a constant velocity motion. Both methods use the periodic nature of the error during a constant velocity motion to determine the amount of periodic error.

Direct spectral analysis involves performing a constant velocity motion and analyzing the measurement interference signal in the Fourier domain. Two additional peaks appear in the Fourier domain when periodic error is present. The amplitude of the three peaks can be used to quantify the periodic error.

Measurement interference signal during constant Doppler velocity scan



$$I_m \propto \cos(2\pi f_s t + \theta_m) + \gamma_1 \cos(2\pi f_s t) + \gamma_2 \cos(2\pi f_s t - \theta_m)$$

$$\gamma_1 = \frac{\Gamma_2}{\Gamma_1}, \quad \gamma_2 = \frac{\Gamma_3}{\Gamma_1}$$

Amplitude sensitivities:

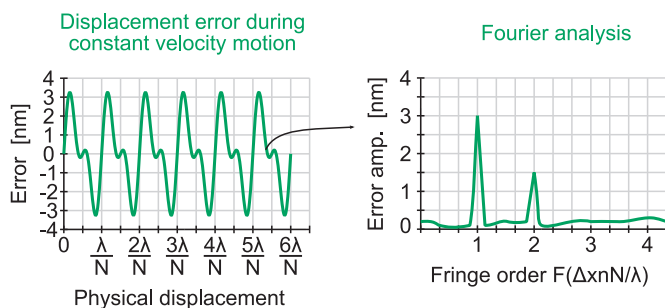
First order: $\sim 25\gamma_1$ [nm]

Second order: $\sim 20\gamma_2$ [nm]

Spatial Fourier Analysis

Another method for measuring periodic error uses the displacement measured during a **constant velocity motion**. The target must displace at least several fringes; otherwise, there is insufficient data for the **spatial Fourier analysis**.

The nominal displacement is first fit with a low-order polynomial. The deviation from the fit contains the periodic error. This error is processed in the Fourier domain based on the **spatial sampling frequency**.



The spatial sampling frequency is determined using the fitted data, scaled to the displacement in fringes. This is the frequency of the data sampling based on the spatial displacement and is used to scale the frequency axis in the Fourier spectrum.

Peaks that appear at the first or second **fringe order** are the periodic error amplitudes from beam leakage.

Several measurements at different velocities should be taken to distinguish periodic error from vibration.

As with all spectral analyses, the data presented in the Fourier domain is based on averaging over many cycles. Periodic error changes and other signal errors can decrease the fidelity of these techniques.

Measurement Uncertainty

DMIs are used to make accurate measurements of a target's displacement. Many error sources can affect the measurement accuracy, thus leading to uncertainty in the measured value. A thorough analysis can be performed to estimate the uncertainty in the measured value with a specified confidence interval.

The **measurand** Y is the quantity to be measured and is a function of **input estimates** x_1, x_2, \dots, x_n , which are quantities that can contribute uncertainty to the measured value of Y . The **output estimate** y is the measured value of Y based on the input estimates and a **measurement model** of the system:

$$y = f(x_1, x_2, \dots, x_n)$$

The uncertainty $u(x_i)$ in input estimates contributes to uncertainty in the measurement of Y . These uncertainties are derived from Type-A or Type-B methods, typically represented by the standard deviation (or **standard uncertainty**) u_i .

In **Type-A** methods, the uncertainty is determined via statistical techniques from measured observations. The standard uncertainty is determined by the standard deviation of the mean of m number of observations.

$$u(x_i) = \sqrt{\frac{1}{m(m-1)} \sum_{j=1}^m (x_{i,j} - \bar{x}_i)^2} \quad \text{for } j = 1, 2, \dots, m$$

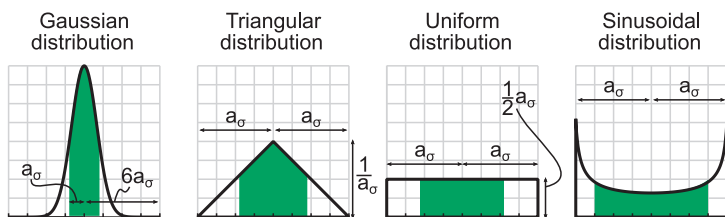
In **Type-B** methods, the uncertainty is determined via assessments other than statistical analyses. The standard uncertainty is determined by an approximated value that corresponds to the estimated standard deviation based on an estimated probability distribution.

The standard deviation of the mean is principally different from the standard deviation. It takes into account the sample size.

Probability Distributions

Type-B uncertainties are determined by methods other than direct observation during the measurement of the measurand. These methods can be based on:

- previous data or calibration data
- reference data from handbook, manufacturer, etc.
- general performance knowledge gained from previous experience



The estimated uncertainty is assigned based on the underlying **probability distribution**.

Gaussian (normal): $u(x_i) = \alpha_\sigma$ (one standard deviation)

Triangular: $u(x_i) = \frac{\alpha_\sigma}{\sqrt{6}} \approx 0.4\alpha_\sigma$

Uniform: $u(x_i) = \frac{\alpha_\sigma}{\sqrt{3}} \approx 0.58\alpha_\sigma$, where $2\alpha_\sigma$ is the width

Sinusoidal: $u(x_i) = \frac{\alpha_\sigma}{\sqrt{2}} \approx 0.71\alpha_\sigma$, where α_σ is the amplitude

The values for $u(x_i)$ are determined such that standard uncertainty values from different parameters can be combined. These values represent a **confidence interval** of 1, meaning that the likelihood of the value being within the stated bounds is 68% for a Gaussian distribution.

Combined Uncertainty

The combined uncertainty u_c of measurand y is the estimated square root of the variance. The **law of propagation of uncertainty** is

$$u_c^2(y) = \sum_{i=1}^n \left(\frac{\partial f}{\partial x_i} \right)^2 u^2(x_i) + 2 \sum_{i=1}^{n-1} \sum_{j=i+1}^n \frac{\partial f}{\partial x_i} \frac{\partial f}{\partial x_j} u(x_i, x_j)$$

Uncertainty in individual parameters combine in quadrature. If there is a correlation, then the covariance $u(x_i, x_j)$ between parameters must be considered. The partial derivatives $\partial f / \partial x_i$ are called the **sensitivity coefficients**.

With **uncorrelated uncertainties**, the covariance term is zero, reducing the combined uncertainty equation.

$$u_c^2(y) = \sum_{i=1}^n \left(\frac{\partial f}{\partial x_i} \right)^2 u^2(x_i)$$

The **combined uncertainty** means that $u_c(y)$ is the standard deviation of measured y , and the likelihood of the true value of measurand Y is between $y - u_c(y)$ and $y + u_c(y)$ with $\sim 68\%$ confidence.

The **expanded uncertainty** U is the combined uncertainty of y multiplied by a **coverage factor**. The coverage factor k is generally 2 or 3 for precision measurements. This represents a 95% (99%) confidence interval for $k = 2$ ($k = 3$). The combined uncertainty with the coverage factor included is

$$U = k u_c(x_i)$$

The uncertainty of measurand Y is then quoted as

$$Y = y \pm U \quad (k = 2)$$

Uncertainty Sources

Measurement uncertainty can be attributed to several sources. The following categories are general classifications of uncertainty sources (note that an uncertainty source can be in multiple categories):

Displacement-dependent sources: These are uncertainties that increase as the desired displacement range increases. They are often described as a fractional value “ x parts in 10^y ,” where this number is multiplied by the displacement range.

Alignment and setup sources: These are uncertainty sources that arise based on the physical setup required to perform a measurement. They are one of the principal reasons that different interferometers can measure the same system with different uncertainties.

Environmental sources: Environmental fluctuations such as temperature drift and pressure changes can alter the optical paths of the light, causing different lengths to be traveled or stress in the optics. These uncertainties are dependent on environmental variables.

Bandwidth sources: Static/quasi-static measurements are generally performed with lower uncertainty values than those used in dynamic measurements. Dynamic measurements require more attention, specifically, for signal processing at high bandwidths or with a change in frequency bands.

Measurement uncertainty is a metric given to a particular measurement and is not specific to the interferometer. Two different interferometers can be used to measure the same target with vastly different measurement uncertainties. Likewise, the same interferometer can measure two different targets with two different measurement uncertainties.

DMI Measurement Model

A **measurement model** is the function that best describes the output estimate of the measurand based on the input estimates. The output estimate d is determined by evaluating the measurement model using the **expected values** for each parameter.

A common **DMI measurement model** is

$$y = f(x_1, x_2, \dots, x_n) \rightarrow d = \frac{1}{2\pi N} \frac{\lambda}{n\psi} \Delta\theta + \sum_i d_i$$

Parameter	Symbol	Contribution
Wavelength	λ	proportional
Refractive index	n	proportional
Scaling factor (cosine)	ψ	proportional
Fold constant	N	none
Phase change	$\Delta\theta$	direct
Additional contributions	d_i	direct

Proportional errors can cause large uncertainties as the measured displacement increases. These uncertainties are quoted as fractional uncertainties. Direct errors contribute an uncertainty regardless of whether the measured displacement was, e.g., 10 μm or 10 m.

Proportional contributions

Wavelength	$u_\lambda(d)$
Refractive index	$u_n(d)$
Scaling factor (cosine)	$u_\psi(d)$

Direct contributions

Phase change	$\Delta\theta$	$u_{\Delta\theta}(d)$
Abbé error	d_A	$u_A(d)$
Thermal drift	d_{TD}	$u_{TD}(d)$
Deadpath	d_{DP}	$u_{DP}(d)$
Periodic error	d_{PE}	$u_{PE}(d)$
Surface figure	d_{SF}	$u_{SF}(d)$
Date age	d_{DA}	$u_{DA}(d)$

Source Vacuum Wavelength

The **vacuum wavelength** λ (along with the refractive index) is responsible for the traceability of interferometric displacement measurements to the unit of length. Any associated uncertainty $u(\lambda)$ directly contributes to the calculated displacement. The uncertainty in the displacement $u_\lambda(d)$ due to uncertainty in the vacuum wavelength is proportional to the displacement z :

$$u_\lambda(d) = \frac{u(\lambda)}{\lambda} z$$

The wavelength uncertainty $u(\lambda)$ has multiple contributors:

- Uncertainty in the determination of the vacuum wavelength.
- Short-term and long-term stability.

The net uncertainty is a quadrature combination of these contributors. The short-term stability is typically quoted on the timescale of hours, whereas long-term stability is a day or more. Also, most lasers have a warmup time period before they are sufficiently stabilized. Different types of heterodyne lasers can have different stabilities, and even similar lasers can have slightly different stability due to construction, alignment, and drift. Stability values are generally specified in the manufacturer's manual.

Frequency-standard lasers, such as an iodine-stabilized HeNe laser at 633 nm, can be used to monitor the wavelength of the source when low uncertainty is required.

In heterodyne lasers, each output beam has a slightly different optical frequency (and wavelength). The correct wavelength should be used based on the manufacturer's specification. If the unintended arm is sent to the measurement target, a systematic scaling factor error in the measurement will result. This is often due to polarization flipping during beam alignment.

Refractive Index Uncertainty

The dominant uncertainty in displacement measurements in air is typically the uncertainty in the refractive index. The uncertainty contribution $u_n(z)$ arises because the light is propagating in a constantly changing refractive index. The uncertainty in absolute refractive index leads to an error in the scaling factor from phase change to physical displacement.

Refractive index uncertainty: $u_n(d) = \frac{u(n)}{n} z$

Air refractive index: For interferometry in air, the uncertainty in the refractive index $u(n_{\text{air}})$ is from changes in temperature, pressure, humidity, and composition. The sensitivity of n_{air} at 633 nm to environmental parameters is:

Temperature T : $K_T \cong -0.93 \times 10^{-6}$ per Kelvin

Pressure P : $K_P \cong +2.68 \times 10^{-9}$ per Pascal

Humidity H : $K_H \cong -1 \times 10^{-8}$ per %RH

These values are based on the modified **Edlén equation** for nominal values at standard conditions. Standard conditions are: $T = 293.15$ K, $P = 101,325$ Pa, and $H = 50\%$.

The air refractive index uncertainty at 633 nm is

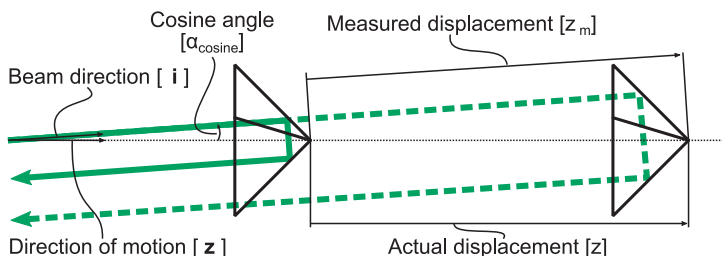
$$u(n_{\text{air}}) = \sqrt{K_T^2 u^2(T) + K_P^2 u^2(P) + K_H^2 u^2(H)}$$

The uncertainties in environmental parameters represent the uncertainty associated with the measurement of those values.

The coefficients of the Edlén equation also have a minor source of uncertainty based on the empirical nature from which they were derived. This equation has an uncertainty contribution of $\sim 1 \times 10^{-8}$ and is typically much smaller than other contributions for all but the most precise measurements.

Cosine Error: Retroreflector Target

Cosine error in an interferometer with a **cube corner target** is the result of an angular misalignment between the vectors representing the beam direction \mathbf{i} and the average line of motion \mathbf{z} of the target.



The relationship between measured and actual displacements (z_m and z , respectively) and the associated error d_ψ are given by

$$z_m = \mathbf{z} \cdot \mathbf{i} = z \cos \alpha_{\cosine} \quad d_\psi = z[\cos(\alpha_{\cosine}) - 1] \approx -z \frac{\alpha_{\cosine}^2}{2}$$

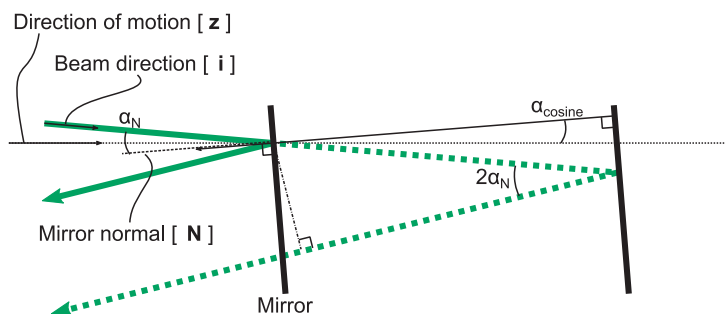
Uncertainty contribution: $u_\psi(d) \approx z \left(\frac{M}{2} \right)^{1/2} u(\alpha_{\cosine})$

When the misalignment is constrained to a plane, M is 1. In this case, planar angles can assume both positive and negative values. For 3D misalignments, M is 2. The misalignment angles are now solid angles and can only assume positive values. An underlying zero-centered normal distribution is assumed for the angles, and the uncertainty represents the standard uncertainty of the distribution.

Larger displacements have larger uncertainty for the same cosine uncertainty. However, larger displacements enable more sensitivity for limiting cosine misalignments, generally leading to lower uncertainty.

Cosine Error: Plane Mirror Target

Cosine error in a **PMI** is the result of angular misalignment α_N between the vectors representing the direction of the incident beam **i** and the mirror normal **N** and the misalignment α_{cosine} between the vectors representing the average line of motion of the target **z** and the mirror normal **N**.



Cosine error can occur even when the mirror normal is collinear with the direction of motion if the beam direction is misaligned. Likewise, even when the beam direction is collinear with the direction of motion, cosine error occurs if the mirror normal is not collinear with the direction of motion.

The relationship between measured and actual displacements (z_m and z , respectively) and the associated error d_ψ are given by

$$z_m = z(\mathbf{N} \cdot \mathbf{i})(\mathbf{z} \cdot \mathbf{N}) = z \cos(\alpha_N) \cos(\alpha_{\text{cosine}})$$

$$d_\psi = z[\cos(\alpha_N) \cos(\alpha_{\text{cosine}}) - 1] \approx -\frac{z}{2}(\alpha_N^2 + \alpha_{\text{cosine}}^2)$$

Uncertainty contribution: $u_\psi(d) = z \left(\frac{M}{2} [u^2(\alpha_N) + u^2(\alpha_{\text{cosine}})] \right)^{1/2}$

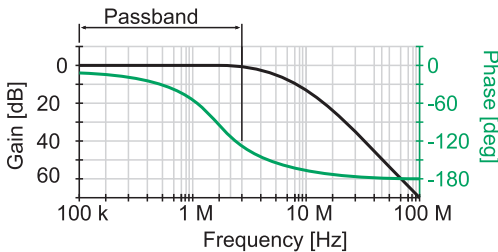
Once again, M is 1 when the error is constrained to a plane. In 3D angles, M is 2.

Phase Change Uncertainty

Uncertainty in the measurement of the phase change $\Delta\theta$ is a direct uncertainty contributor to the measurand. The uncertainty in the measured phase $u(\Delta\theta)$ directly contributes to uncertainty in the measured displacement $u_{\Delta\theta}(d)$.

Phase change uncertainty: $u_{\Delta\varphi}(d) = \frac{u(\Delta\theta)}{\Delta\theta} d$

The phase change uncertainty is rarely specified. Typically, manufacturers state the static/quasi-static accuracy and dynamic accuracy. Static/quasi-static accuracy is generally quoted as the electronic noise floor. Dynamic accuracy is based on the phase meter performance at specified target velocities. Dynamic accuracy is a larger value, as nonlinearities from filtering, etc. are frequency dependent. These nonlinearities result from additional phase lag in the processing electronics and appear as an interferometric phase change.

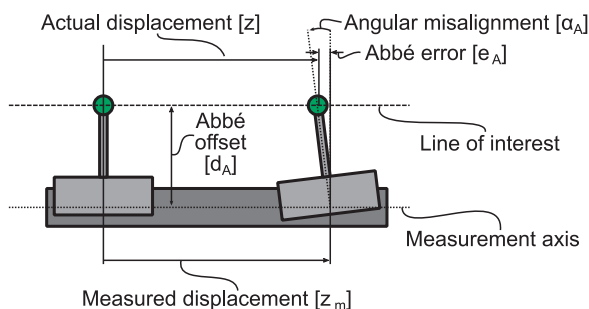


For example, the optical reference is at a constant 1 MHz, but the measurement interference signal changes from 1 MHz to 2 MHz due to target Doppler shifts. The electronics has an additional phase delay due to the higher frequency, causing a phase error and a source of uncertainty. This phase delay is typically not specified by the manufacturer but rather is encompassed in the dynamic accuracy.

Without any other information, a reasonable estimate for $u(\Delta\theta)$ is a uniform noise spectrum with a half-width a_σ equal to the specified static/quasi-static or dynamic accuracy based on the measurement situation.

Abbé Uncertainty

The **Abbé principle** involves arranging the measurement system to be collinear with the measured line of interest. Unintended angular errors α_A of the linear motion cause an offset error e_A when the measurement axis and line of interest are not collinear. Larger Abbé offsets d_A lead to larger errors between the measurement and the actual motion on the line of interest.



$$\text{Abbé error: } d_A = z_m - z = d_A \tan(\alpha_A) \approx d_A \alpha_A$$

Abbé error is typically calculated assuming small angle approximations, reducing the error to the product of the Abbé offset and angular misalignment.

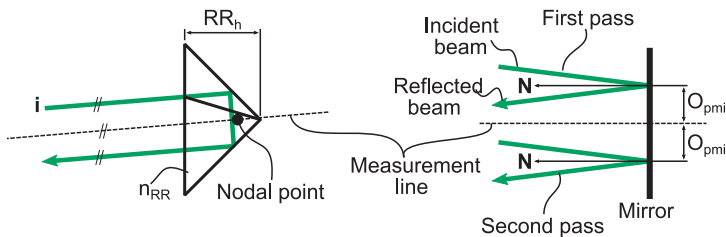
There are two mutually orthogonal directions based on directions perpendicular to the Abbé offset vector. Each of these directions can have an associated angular misalignment that contributes to Abbé error.

$$\text{Abbé uncertainty: } u_A^2(d) = \alpha_A^2 u^2(d_A) + d_A^2 u^2(\alpha_A)$$

In the simplest case, the angular motions are uncorrelated, and the resulting uncertainties combine in quadrature. In practice, the error motions typically have some correlation that requires extra terms to account for the correlation.

Measurement Axis Location

The interferometer target determines the measurement line in the interferometer. The measurement line in a **retroreflector target** is the line that passes through the nodal point and is parallel to the beam direction \mathbf{i} . The nodal point for a solid retroreflector is located within the retroreflector at RR_h/n_{RR} from the front face, where RR_h is the retroreflector height and n_{RR} is the refractive index of the retroreflector. The nodal point for a hollow retroreflector is located at the apex.

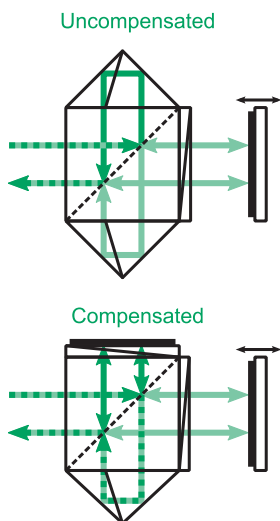


The measurement line for a **plane mirror target** is parallel to the mirror normal \mathbf{N} and is located midway between the incident beams on the mirror surface. The mirror normal sets the direction, while the beams constrain the location of the measurement line.

The uncertainty from offsets in setting the measurement line is an additional Abbé error to consider. Retroreflectors can exhibit lower uncertainty because the nodal point can be accessed via the apex. For plane mirrors, the uncertainty is larger because it is a virtual point, and errors in mirror flatness and beam pointing between the first pass and second pass can create slight errors in the measurement location during mirror translation.

Interferometer Thermal Drift

Interferometer thermal drift occurs when thermal changes within the interferometer optics cause apparent displacements in the measurement, even when the target is stationary. This thermal drift is indistinguishable from the intended displacement measurements. The thermal drift leads to uncertainty in the measured displacement based on uncertainty in the temperature change of the interferometer.



The OPD between the measurement and reference arms in an interferometer is balanced when the difference is zero. If the paths are not balanced, the additional optical path in one arm will see a greater effect from thermal expansion than the shorter arm. Interferometers that are not compensated for differences in **optical path length** (OPL) have a higher thermal drift coefficient C_T than **balanced interferometers**, which are compensated with balanced OPLs.

Manufacturers will specify C_T based on the configuration, material, and mechanical tolerances of the manufactured components. C_T can range from nanometers/Kelvin to micrometers/Kelvin.

Thermal drift error: $d_{TD} = C_T \Delta T$

Thermal drift uncertainty:

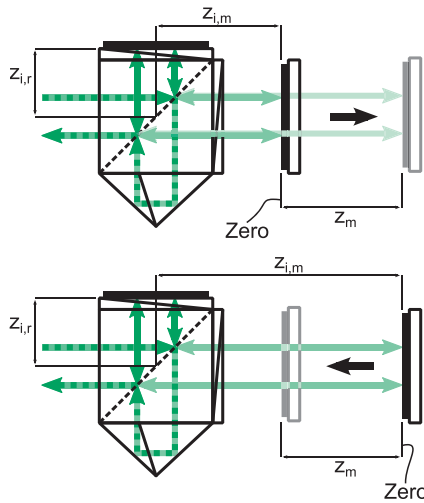
$$u_{TD}^2(d) = C_T^2 u^2(\Delta T) + \Delta T^2 u^2(C_T)$$

The procedure that involves these equations is also used for determining thermal drift in the target and metrology loop between the interferometer and the target.

Deadpath Uncertainty

The **interferometer deadpath** is the difference in OPL $z_{DP} = z_{i,m} - z_{i,r}$ between the measurement and reference arms when the interferometer electronics are zeroed. Often, the deadpath value is not the position closest to the interferometer.

The arm length imbalance ($z_{i,m} \neq z_{i,r}$) increases the sensitivity to source wavelength changes $\Delta\lambda$ and refractive index changes Δn . This shifts the location of the zero position. Global changes in source wavelength and refractive index cause changes in the OPL. Even when correcting for these changes, this correction only applies when the target is at the zero position, as the interferometer is insensitive to its initial imbalance.



Deadpath error:

$$d_{DP} = \frac{z_{DP}\Delta\lambda}{\lambda_i} - \frac{z_{DP}\Delta n}{n_f}$$

The subscripts *i* and *f* denote *initial* and *final*, respectively. The wavelength and refractive index must be tracked to correct for deadpath errors.

Deadpath uncertainty:

$$u_{DP}^2(d) = \Delta z_{DP}^2 \left(\frac{u(\Delta n)}{n} \right)^2 + \Delta z_{DP}^2 \left(\frac{u(\Delta\lambda)}{\lambda} \right)^2$$

This equation neglects the uncertainty contribution from the nominal deadpath value, which is typically much smaller than some of the other errors that are, technically, still present. The uncertainties $u(\Delta n)$ and $u(\Delta\lambda)$ are uncertainties for the duration of the measurement period.

Periodic Error Uncertainty

Periodic error (also called **cyclic error**) is a noncumulative error in the measured displacement from spurious interference signals arising from source mixing and beam leakage. The phase-to-displacement relationship is assumed to be linear, but these spurious signals create a cyclic deviation. Periodic error occurs at predictable intervals.

First-order errors have one harmonic per every 2π -phase change. The amplitude of the error is A_1 .

Second-order errors have two harmonics per every 2π -phase change. The amplitude of the error is A_2 .

Other harmonics may appear due to beam shear, ghost reflections, and phase measurement electronics. These amplitudes are often lower than the second-order error amplitude.

Uncertainty from periodic error has an underlying sinusoidal distribution. This means that the likelihood of the value is weighted away from the mean. The half-width of the distribution a_σ is the periodic error amplitude. The uncertainty of a sinusoidal distribution is approximately 70% of a_σ .

The **periodic error uncertainty** is expressed as

$$u_{\text{PE}}^2(d) = u^2(A_1) + u^2(A_2) \cong (0.71A_1)^2 + (0.71A_2)^2$$

If the mixing amplitudes γ_1 and γ_2 from the measurement interference signal are known, the uncertainty (in nanometers) from periodic error can be estimated using the following:

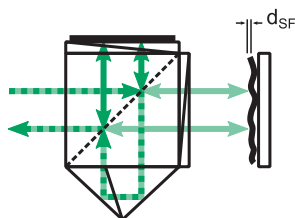
$$I_m \propto \cos(2\pi f_s t + \theta_m) + \gamma_1 \cos(2\pi f_s t) + \gamma_2 \cos(2\pi f_s t - \theta_m)$$

$$u_{\text{PE}}^2(d) \cong (17.7\gamma_1)^2 + (13.1\gamma_2)^2$$

Surface Figure Error

Measurement targets ideally have perfectly flat surfaces. For retroreflector targets, this means that no wavefront distortion is imparted on the measurement beam from the transmission surface nor from the three reflecting surfaces. For plane mirror targets, the measurement surface should be perfectly flat.

Deviations from the target **surface figure** have little effect on beam pointing but directly contribute to measurement errors. Uncertainty in the surface figure is a direct contributor to uncertainty.



Surface figure uncertainty is expressed as

$$u_{SF}(d) = u(d_{SF})$$

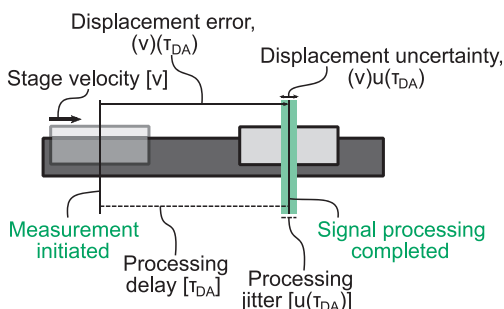
Surface figure errors arise from two sources:

- Cosine errors between the target and beam pointing, leading to the beam shifting as a function of displacement. Errors from this source can be mitigated by minimizing cosine errors and by specifying tight tolerances at the beam locations on a target surface.
- Out-of-plane target motions from the main target direction. For retroreflector targets, this is generally from straightness errors where slight lateral motions of the target occur as a function of displacement. In plane mirror targets, this is a problem for multiaxis stages that have a long stroke motion in orthogonal axes.

Surface figure errors can be **error mapped**, a method in which a lookup table is generated to correct the measurement, even in realtime applications. Error mapping is used in many multiaxis applications, where planar stage motion is measured with displacement interferometry. Error mapping can be performed with surface interferometry to determine the deviations.

Data Age Uncertainty

Dynamic measurements pose another problem in displacement interferometry due to the processing time needed to compute the phase. Even when the delay is known, modern signal processing techniques with FPGAs and DSPs will still have some inherent jitter. Data age uncertainty is critical at higher Doppler velocities.



In a **quasi-static example**, if the delay τ_{DA} is 1 μs and jitter $u(\tau_{DA})$ is 10 ns, then a stage moving with a 1- $\mu\text{m/s}$ velocity v must account for a 1-pm displacement error from the delay and a $1 \times 10^{-16}\text{m}$ position uncertainty from the jitter.

In a **dynamic example**, if the same delay and jitter are used but the stage is moving at 1 m/s, then the displacement error from the delay is 1 μm , and the displacement uncertainty from the jitter is 10 nm. The error from the delay can be compensated by knowing the delay, but the error from jitter leads to uncertainty.

Data age error is expressed as

$$d_{DA} = \tau_{DA}v$$

Data age uncertainty is expressed as

$$u_{DA}(z) = u(\tau_{DA})v$$

The uncertainty in displacement from data age uncertainty is the velocity times the jitter, typically with an assumed uniform distribution with half-width a_σ equal to $u(\tau_{DA})$.

Error Corrections

Many uncertainties in DMI measurements can be attributed to specific error contributions. In many cases, applied **error corrections** can reduce the measurement error, thus reducing the measurement uncertainty.

Error corrections should be applied using the correct sign (positive or negative) of the error. Otherwise, the corrective term will double the existing error in the measurement.

The **displacement measurement model** contains the parameters needed to correct measurement, provided that the error is known. The corrective terms are often determined by additional measurements, such as alignment, environmental parameters, and setup parameters. These additional measurements and parameters can lead to more complicated measurements but may be necessary depending on the desired accuracy. The process for correcting errors in displacement measurements begins with the DMI measurement model:

$$d = \frac{1}{2\pi N} \frac{\lambda}{n\psi} \Delta\theta + \sum_i d_i$$

where the errors can be included in the calculation, provided that the values are known. In general, the largest errors tend to be from refractive index errors (for measurement in air), cosine errors, and Abbé errors. These errors can be especially significant if the target displaces a long distance. The next grouping of contributors tends to be from periodic error, thermal drift errors, deadpath, and target surface figure error. For measurements performed over a short duration, the thermal errors tend to be mitigated, and periodic error is usually limited to the 1- to 5-nm range. If the measurement duration is longer, thermal drift and target surface figure errors can become significant. When using a stabilized laser, the laser frequency error tends to not be a problem unless there is significant uncertainty in the vacuum wavelength.

Air Refractive Index Compensation

The refractive index of air can be compensated for using three methods: (1) equation-based procedures, (2) absolute refractometry, and (3) wavelength tracking, each of which is explained below.

In **equation-based compensation** methods, the environmental parameters are precisely measured. Equations such as the modified Edlén or the Ciddor, and the *NIST Shop Floor* refractive index calculations can be used to postcorrect interferometry measurements. Limitations of these methods include:

- Bandwidth is limited, as environmental parameter measurements need sufficient integration time.
- Empirical uncertainty is limited for high-accuracy measurements.
- It is difficult to correct measurements in process.

Absolute **refractometry**, where one arm of an interferometer is in vacuum and the other is in air, is a method for both measuring the absolute refractive index and, subsequently, tracking refractive index changes. Absolute refractive index values can be determined, but imperfections in the measurement can still generate uncertainties on the order of a few parts in 10^8 .

Wavelength tracking is a method in which the difference between two interferometer arms is a fixed cavity with low thermal expansion. Measured changes are due to refractive index changes. Note that this method requires another method (typically equation-based) to determine the absolute refractive index value at the start of the measurement.

Vertical interferometers suffer from refractive index changes due to variations in air density from altitude changes. This sensitivity to **altitude effects** is approximately 3.5×10^{-8} per meter of altitude gain.

Error Budget

An **error budget** is commonly used for estimating the performance of a displacement interferometer when measuring a target. Error budgets are useful for identifying the largest errors and determining which errors can be neglected. Then, if needed, correction methods can be devised to mitigate the largest error sources, improving the overall estimate.

An error budget is not the same as a measurement uncertainty estimate. Error budgets are typically generated assuming that errors are uncorrelated and that the total error is determined by the quadrature sum of all of the errors. For a basic estimate, errors that are an order of magnitude lower than the largest-error magnitude can be ignored. For example,

$$\sqrt{(10\text{ nm})^2 + (1\text{ nm})^2} \cong 10.05\text{ nm} \approx 10\text{ nm}$$

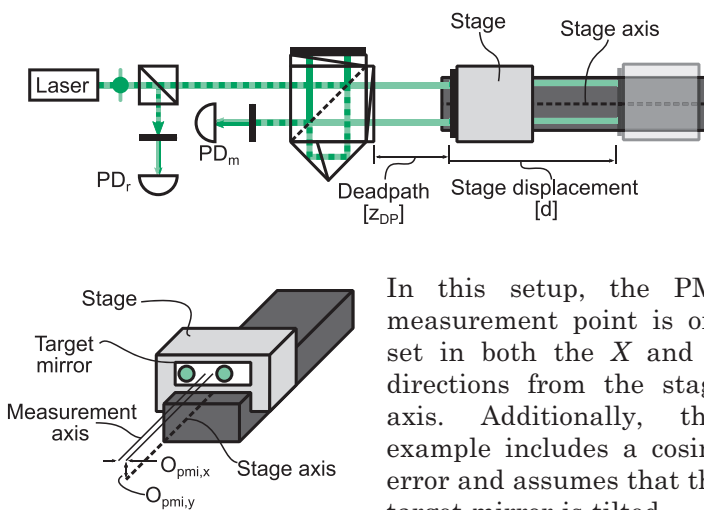
The 1-nm error contributes significantly less than the 10-nm error and can be ignored.

Refractive index errors can be estimated based on the temperature and pressure fluctuations of the surrounding environment. Temperature fluctuations can also be used for calculating any thermal drift in the interferometer or system. Generally, the thermal drift error will be low due to the thermal time constant of the components. The wavelength, phase error, and data age error can be estimated from the manufacturer's specification and the anticipated target velocity.

The alignment and setup errors are determined based on the particular system configuration. The cosine error can be determined by placing a CCD or PSD on the moving target and minimizing the beam offset at different points. For a plane mirror, the surface normal can be aligned using the same CCD or PSD in a reflecting configuration, after the mirror trajectory and beam vector are adjusted to be collinear.

Stage Measurement Uncertainty Example

This is an example of using a PMI to measure the displacement of a stage to, e.g., compare the measured result to the stage's onboard linescale. This is a generic depiction of one method to calibrate the linescale on a linear stage. In this example, the measurand is the **stage displacement** d located on the stage axis that is collinear with its internal linescale.



In this setup, the PMI measurement point is off-set in both the X and Y directions from the stage axis. Additionally, this example includes a cosine error and assumes that the target mirror is tilted.

“Although this guide provides a framework for assessing uncertainty, it cannot substitute for critical thinking, intellectual honesty, and professional skill. The evaluation of uncertainty is neither a routine task nor a purely mathematical one; it depends on detailed knowledge of the nature of the measurand and of the measurement. The quality and utility of the uncertainty quoted for the result of a measurement therefore ultimately depend on the understanding, critical analysis, and integrity of those who contribute to the assignment of its value.”

- ANSI/NCSL Z540-2-1997, Section 3.4.8

Example Uncertainty Parameters

Several **parameters** are needed to begin developing an **error budget** and **uncertainty estimate**. For this example, a short measurement duration is assumed in order to minimize refractive index and thermal errors.

- The stage travel is 400 mm with a 50-mm deadpath.
- The Abbé offsets are: $d_{A,y} = 20$ mm and $d_{A,x} = 5$ mm.
- The cosine alignment is better than 0.5 mrad.
- The input beam is aligned to be better than 100 μ rad with respect to the mirror surface normal.
- The nominal source wavelength and stability are specified by the laser manufacturer.
- The phase resolution is specified by the manufacturer.
- Stage-error motions are based on the stage manufacturer's specification.
- The environment normally has a stability of 0.1 K, 250 Pa, and 5% RH for a one-hour duration.
- The mirror surface is specified to $\lambda/10$ over the full surface and better than $\lambda/50$ over any 1-mm-diameter aperture on the surface.
- The stage is measured in a quasi-static configuration.
- Periodic error is not considered in this estimate.

The example **measurement model** is expressed as

$$d = \frac{1}{8\pi} \frac{\lambda}{n\psi} \Delta\theta - d_{A,y}\varphi_x - d_{A,x}\varphi_y + \frac{\Delta n}{n_f} z_{DP} - \frac{\Delta\lambda}{\lambda_i} z_{DP} + d_{SF}$$

This model is used for the uncertainty estimate. Only parameters that are measured concurrently with the DMI system can have applied corrections. The sign of the error should be considered when applying corrections.

These parameters are representative examples of specifications. In practice, they will vary depending on the components used, the manufacturer, and the specific configuration.

Example Uncertainty Propagation

This example assumes that the uncertainties between parameters are uncorrelated, simplifying the **law of propagation of uncertainty** to

$$u_c^2(y) = \sum_{i=1}^n \left(\frac{\partial f}{\partial x_i} \right)^2 u^2(x_i)$$

Applying this to the example measurement model yields

$$\begin{aligned} u_c^2(d) = & \left(\frac{u(\lambda)}{\lambda} \right)^2 d^2 + \left(\frac{u(n)}{n} \right)^2 d^2 + \left(\frac{u(\psi)}{d} \right)^2 d^2 \\ & + \left(\frac{\lambda}{8\pi n} \right)^2 u^2(\Delta\theta) + \varphi_x^2 u^2(d_{A,y}) + d_{A,y}^2 u^2(\varphi_x) \\ & + \varphi_y^2 u^2(d_{A,x}) + d_{A,x}^2 u^2(\varphi_y) + z_{DP}^2 u^2\left(\frac{\Delta n}{n_f}\right) \\ & + \left(\frac{\Delta n}{n_f}\right)^2 u^2(z_{DP}) + z_{DP}^2 u^2\left(\frac{\Delta\lambda}{\lambda_i}\right) + \left(\frac{\Delta\lambda}{\lambda_i}\right)^2 u^2(z_{DP}) \end{aligned}$$

Each of these terms can be addressed individually and then combined in quadrature to determine the combined uncertainty estimate.

The nominal source wavelength and stability are specified by the laser manufacturer. These are assumed to be normal distributions when determining **wavelength uncertainty**.

Nominal source wavelength: $u(\lambda_{\text{nom}})/\lambda = 2 \times 10^{-8}$

One-hour stability: $u(\lambda_{\text{stab}})/\lambda = 5 \times 10^{-9}$

$$\frac{u(\lambda)}{\lambda} = \sqrt{\left(\frac{u(\lambda_{\text{nom}})}{\lambda} \right)^2 + \left(\frac{u(\lambda_{\text{stab}})}{\lambda} \right)^2} \cong 2 \times 10^{-8}$$

$$u_\lambda(d) = \frac{u(\lambda)}{\lambda} d = (2 \times 10^{-8})(0.45 \text{ m}) \cong 9.3 \text{ nm}$$

Example Uncertainty Propagation (cont.)

The environment normally has a stability of 0.1 K, 250 Pa, and 5% RH at standard atmospheric conditions for a one-hour duration, all of which are suitable for this example. In the absence of other information, these values, which drive the **refractive index variation**, are assumed to be the maximum range of the error.

Temperature controllers typically lead to a sinusoidal distribution in the temperature profile. If $\alpha_{\sigma,T}$ is one-half of the range, then $u(T) = 0.05 \text{ C}/\sqrt{2} \cong 0.035 \text{ C}$. Pressure and humidity can be assumed to have rectangular distributions, where $\alpha_{\sigma,P}$ and $\alpha_{\sigma,H}$ are the half-ranges. The pressure uncertainty is then $u(P) = 125 \text{ Pa}/\sqrt{3} \cong 72.2 \text{ Pa}$, and the humidity uncertainty is $u(H) = 2.5\%/\sqrt{3} \cong 1.44\%$.

$$\begin{aligned} u^2(n_{\text{air}}) &= K_T^2 u^2(T) + K_P^2 u^2(P) + K_H^2 u^2(H) + u_{\text{Edlen}}^2 \\ &= K_T^2 (0.035)^2 + K_P^2 (72.2)^2 + K_H^2 (1.44)^2 + (3 \times 10^{-8})^2 \\ u(n_{\text{air}}) &\cong 2 \times 10^{-7} \end{aligned}$$

$$K_T \cong -0.93 \times 10^{-6}/\text{K} \quad K_P \cong +2.68 \times 10^{-9}/\text{Pa} \quad K_H \cong -1 \times 10^{-8}/\%$$

$$u_n(d) = \frac{u(n)}{n} d = (2 \times 10^{-7})(0.45 \text{ m}) \cong 90 \text{ nm}$$

The beam shift from **cosine error** is 250 μm at the full range. This is an angular error α_{cosine} of 0.5 mrad. The input beam alignment α_N is 100 μrad with respect to the mirror surface normal direction. Both are assumed to have normal distributions in 2D.

$$u(\alpha_N) = \alpha_N^2 \cong 1 \times 10^{-8} \quad u(\alpha_{\text{cosine}}) = \alpha_{\text{cosine}}^2 \cong 2.5 \times 10^{-7}$$

$$u(\psi) = \left(\frac{M}{2} [u^2(\alpha_N) + u^2(\alpha_{\text{cosine}})] \right)^{1/2} \cong 2.5 \times 10^{-7}$$

$$u_\psi(d) = (d)u(\psi) \cong 112.5 \text{ nm}$$

Example Uncertainty Propagation (cont.)

The estimated Abbé offsets are $d_{A,y} = 20$ mm and $d_{A,x} = 5$ mm. The offset length can be determined within a 1-mm range, assuming a rectangular distribution as well. As the nominal angle is assumed to be zero, this is negligible in the uncertainty analysis. The stage manufacturer specifies that the stage error motion is less than $25 \mu\text{rad}$. This is assumed in each direction with a rectangular distribution. Based on this, the angular uncertainty is $u(\varphi_y) = u(\varphi_x) = 25 \mu\text{rad}/\sqrt{3} \cong 14.4 \mu\text{rad}$.

The **Abbé uncertainty** is

$$\begin{aligned} u_A(d) &= \sqrt{\varphi_x^2 u^2(d_{A,y}) + d_{A,y}^2 u^2(\varphi_x) + \varphi_y^2 u^2(d_{A,x}) + d_{A,x}^2 u^2(\varphi_y)} \\ &= \sqrt{(20 \text{ mm})^2 (14.4 \mu\text{rad})^2 + (5 \text{ mm})^2 (14.4 \mu\text{rad})^2} \\ &= 296.9 \text{ nm} \end{aligned}$$

The deadpath is estimated at 50 mm and can be determined within a 1-mm range (rectangular). Thus, the **deadpath uncertainty** is $u(z_{\text{DP}}) = 1 \text{ mm}/2\sqrt{3} \cong 0.29 \text{ mm}$. The maximum change in refractive index is determined by the maximum change in the environmental parameters. The maximum fractional wavelength change is based on the laser stability.

$$\frac{\Delta n}{n} = |K_T \Delta T| + |K_P \Delta P| + |K_H \Delta H| \cong 2.1 \times 10^{-7} \quad \frac{\Delta \lambda_{\text{stab}}}{\lambda} = 5 \times 10^{-9}$$

$$\begin{aligned} u_{\text{DP}}^2(d) &= z_{\text{DP}}^2 \left[u^2\left(\frac{\Delta n}{n_f}\right) + u^2\left(\frac{\Delta \lambda}{\lambda_i}\right) \right] + \left[\left(\frac{\Delta \lambda}{\lambda_i}\right)^2 + \left(\frac{\Delta n}{n_f}\right)^2 \right] u^2(z_{\text{DP}}) \\ u_{\text{DP}}(d) &= 10.5 \text{ nm} \end{aligned}$$

Example Uncertainty Propagation (cont.)

The surface figure error is $\lambda/50$ over any 1-mm aperture on the surface. The beam pointing and cosine error can contribute to a maximum error of 750 μrad , leading to a beam shift of 338 μm on the surface. Assuming that the surface figure error scales linearly, the maximum **surface figure error** per beam is

$$d_{\text{SF}} = (0.338)(\lambda/50) = (0.338)(633 \text{ nm}/50) \cong 4.3 \text{ nm}$$

Two beams reflect from the target mirror because a PMI is used; this error is assumed to have a rectangular distribution.

$$u_{\text{SF}}(d) = \sqrt{2}u(d_{\text{SF}}) = \sqrt{2}\frac{d_{\text{SF}}}{\sqrt{3}} \cong 3.5 \text{ nm}$$

The phase resolution is specified by the manufacturer of the phase meter. For quasi-static measurements, phase resolution is $2\pi/2048$ for a PMI configuration. Generally, the **phase meter uncertainty** is determined by the **least significant bit** (LSB) of the phase divisor. For quasi-static measurements, this is assumed to be 1 LSB, with a rectangular distribution.

$$u(\Delta\theta) = \frac{2\pi}{2048\sqrt{3}} \cong 1.8 \text{ mrad}$$

$$u_{\Delta\varphi}(d) = \frac{\lambda}{8\pi n} u(\Delta\theta) \cong 0.05 \text{ nm}$$

Other uncertainties not considered in this example are the periodic error. For uncorrected phase meters, this can contribute several nanometers of uncertainty. Also, the thermal drift of the interferometer was not considered. Lastly, the thermal drift of the stage between the measurement mirror and the center of the stage, or functional point, was not considered. Both of these thermal drifts can also contribute several nanometers of additional uncertainty.

Example Combined Uncertainty

Each individual uncertainty contribution is combined in quadrature to determine the uncertainty estimate.

Contributor	Variable	Contribution [nm]
Wavelength	$u_{\lambda}(d)$	9.3
Refractive index	$u_n(d)$	90
Cosine	$u_{\psi}(d)$	112.5
Abbé error	$u_A(d)$	296.9
Deadpath	$u_{DP}(d)$	10.5
Surface figure	$u_{SF}(d)$	3.5
Phase change	$u_{\Delta\theta}(d)$	0.05
Combined	$u_c(d)$	330

The **combined standard uncertainty** ($k = 2$) is 660 nm, with the largest contributions from Abbé and cosine errors. These errors can be mitigated by altering the alignment or, in the case of Abbé, measuring the angular motions to correct the error in real time.

The remaining uncertainties are dominated by the refractive index, which can be improved by implementing a wavelength tracker or by monitoring the environmental parameters during the measurement.

While this is just an example, this error budget is typical of the uncertainty budget for a stage calibration. In most cases, the setup errors (cosine errors and Abbé errors) are the largest measurement uncertainty contributors. Refractive index uncertainty causes the next largest uncertainty. The remaining uncertainty sources contribute little to the overall uncertainty budget, so correcting alignment errors, Abbé errors, and refractive index errors can greatly reduce the overall uncertainty.

Equation Summary

Optical frequency:

$$f = \frac{c}{n\lambda} = \frac{\nu}{\lambda}$$

Refractive index:

$$n = \frac{c}{\nu} = \sqrt{\epsilon_r \mu_r}$$

Electric field vector:

$$\mathbf{E} = E_0 e^{i2\pi(f t \pm \frac{\mathbf{z}_p n}{\lambda})} = E_0 e^{i(\omega t \pm \varphi(\mathbf{z}_p))}$$

$$E_0 = \sqrt{\frac{2P_0}{\epsilon \nu A}}$$

$$\omega = 2\pi f$$

$$\varphi(\mathbf{z}_p) = \frac{2\pi \mathbf{z}_p n}{\lambda}$$

Irradiance:

$$\mathbf{E}_1 = E_{01} e^{i(\omega_1 t + \theta_1)}, \quad \mathbf{E}_2 = E_{02} e^{i(\omega_2 t + \theta_2)}, \quad \mathbf{E}_{\text{net}} = \mathbf{E}_1 + \mathbf{E}_2$$

$$I = \frac{c\epsilon_0}{2} \mathbf{E}_{\text{net}}^2 = \frac{c\epsilon_0}{2} \left(|\mathbf{E}_1|^2 + |\mathbf{E}_2|^2 + 2\mathbf{E}_1 \cdot \mathbf{E}_2 \right)$$

$$\mathbf{E}_1 \cdot \mathbf{E}_2 = |\mathbf{E}_1| |\mathbf{E}_2| \cos \alpha_p$$

Detected irradiance:

$$I_D = \int_{A_D} I dA_D$$

Fringe contrast:

$$I_{\text{FC}} = \frac{I_{\text{max}} - I_{\text{min}}}{I_{\text{max}} + I_{\text{min}}} = \frac{I_{\text{amp}}}{I_{\text{mean}}}$$

Malus' law:

$$I_o = I_i \cos^2(\alpha_p)$$

Equation Summary

Temporal coherence:

$$L_c = \frac{2 \ln(2)}{\pi n} \frac{\lambda^2}{\Delta \lambda} \approx 0.44 \frac{\lambda^2}{\Delta \lambda} \text{ [in air]}$$

$$L_c \approx 0.44 \frac{c}{\Delta f} \text{ [in air]}$$

Optical path difference:

$$z_o = nNz_p$$

Displacement from phase change:

$$\Delta \theta = \frac{2\pi nN \Delta z_p}{\lambda} \rightarrow \Delta z_p = \frac{\lambda \Delta \theta}{2\pi nN}$$

Doppler frequency shift:

$$f_D = \frac{nNv_D}{\lambda}$$

Laser free spectral range:

$$\text{FSR} \cong \frac{c}{2l_c}$$

Time interval analysis fringe interpolation:

$$\frac{\theta}{2\pi} = R - M + \left(\frac{T_{m,i} - T_r}{T_{m,i} - T_{m,(i-1)}} \right)$$

Equation Summary

Angle interferometer sensitivity:

$$\varphi_x = \frac{\lambda \theta}{2\pi N n} \cdot \frac{1}{L_{RR}}$$

Straightness interferometer sensitivity:

$$z_p = 2\Delta x \sin\left(\frac{\alpha_s}{2}\right)$$

NIST Shop Floor refractive index calculator over two difference ranges:

$$n = 1 + \frac{7.86 \times 10^{-4} P}{273 + T} - 1.5 \times 10^{-11} RH(T^2 + 160)$$

Parameter	Range 1	Range 2
T [°C]	0–35	19.5–20.5
P [kPa]	50–120	90–110
RH [%]	0–100	0–70
CO ₂ [ppm]	300–600	350–500
$u(n)$	1.5×10^{-7}	5×10^{-8}

Snell's law:

$$n_i \sin(\psi_i) = n_o(\psi_o)$$

Shear-plate beam displacement as a function of angle:

$$\delta_s = t_p \sin \psi_t - \frac{t_p n_{\text{air}} \sin 2\psi_t}{2n_g \sqrt{1 - \left(\frac{n_{\text{air}}}{n_g}\right)^2 \sin^2 \psi_t}}$$

Equation Summary

Beam deflection in a Risley prism (wedged plate):

$$\gamma_w = \sin^{-1} \left(\frac{n_g}{n_{\text{air}}} \sin \psi_w \right) - \psi_w$$

Heterodyne interference equation with periodic error:

$$I_m \propto \cos(2\pi f_s t + \theta_m) + \gamma_1 \cos(2\pi f_s t) + \gamma_2 \cos(2\pi f_s t - \theta_m)$$

Periodic error amplitude sensitivities:

$$\gamma_1 = \frac{\Gamma_2}{\Gamma_1}, \quad \gamma_2 = \frac{\Gamma_3}{\Gamma_1}$$

$$\begin{aligned} \text{First order: } & \sim 25\gamma_1 \text{ [nm]} \\ \text{Second order: } & \sim 20\gamma_2 \text{ [nm]} \end{aligned}$$

Standard deviation of the mean for uncertainty calculations:

$$u(x_i) = \sqrt{\frac{1}{m(m-1)} \sum_{j=1}^m (x_{i,j} - \bar{x}_i)^2} \quad \text{for } j = 1, 2, \dots, m$$

Law of propagation of uncertainty:

$$u_c^2(y) = \sum_{i=1}^n \left(\frac{\partial f}{\partial x_i} \right)^2 u^2(x_i) + 2 \sum_{i=1}^{n-1} \sum_{j=i+1}^n \frac{\partial f}{\partial x_i} \frac{\partial f}{\partial x_j} u(x_i, x_j)$$

$$u_c^2(y) = \sum_{i=1}^n \left(\frac{\partial f}{\partial x_i} \right)^2 u^2(x_i)$$

(if uncertainties are uncorrelated)

Equation Summary

Probability distributions:

$$\text{Gaussian: } u(x_i) = \alpha_\sigma$$

$$\text{Triangular: } u(x_i) = \frac{\alpha_\sigma}{\sqrt{6}} \approx 0.4\alpha_\sigma$$

$$\text{Uniform: } u(x_i) = \frac{\alpha_\sigma}{\sqrt{3}} \approx 0.58\alpha_\sigma$$

$$\text{Sinusoidal: } u(x_i) = \frac{\alpha_\sigma}{\sqrt{2}} \approx 0.71\alpha_\sigma$$

Displacement interferometer measurement model for error corrections and uncertainty calculations:

$$y = f(x_1, x_2, \dots, x_n) \quad \rightarrow \quad d = \frac{1}{2\pi N} \frac{\lambda}{n_\psi} \Delta\theta + \sum_i d_i$$

Source vacuum wavelength uncertainty:

$$u_\lambda(d) = \frac{u(\lambda)}{\lambda} z$$

Refractive index uncertainty:

$$u_n(d) = \frac{u(n)}{n} z$$

Air refractive index at 633 nm:

$$u(n_{\text{air}}) = \sqrt{K_T^2 u^2(T) + K_P^2 u^2(P) + K_H^2 u^2(H)}$$

$$K_T \cong -0.93 \times 10^{-6} \text{ per Kelvin}$$

$$K_P \cong +2.68 \times 10^{-9} \text{ per Pascal}$$

$$K_H \cong -1 \times 10^{-8} \text{ per \%RH}$$

Equation Summary

Cosine error (retroreflector target):

$$d_{\psi} = z[\cos(\alpha_{\text{cosine}}) - 1] \approx -z \frac{\alpha_{\text{cosine}}^2}{2}$$

Cosine uncertainty (retroreflector target):

$$u_{\psi}(d) \approx z \left(\frac{M}{2} \right)^{1/2} u(\alpha_{\text{cosine}})$$

Cosine error (plane mirror target):

$$d_{\psi} = z[\cos(\alpha_N) \cos(\alpha_{\text{cosine}}) - 1] \approx -\frac{z}{2} (\alpha_N^2 + \alpha_{\text{cosine}}^2)$$

Cosine uncertainty (plane mirror target):

$$u_{\psi}(d) = z \left(\frac{M}{2} [u^2(\alpha_N) + u^2(\alpha_{\text{cosine}})] \right)^{1/2}$$

Phase change uncertainty:

$$u_{\Delta\phi}(d) = \frac{u(\Delta\theta)}{\Delta\theta} d$$

Abbé error:

$$d_A = z_m - z = d_A \tan(\alpha_A) \approx d_A \alpha_A$$

Abbé uncertainty:

$$u_A^2(d) = \alpha_A^2 u^2(d_A) + d_A^2 u^2(\alpha_A)$$

Interferometer thermal drift error:

$$d_{\text{TD}} = C_T \Delta T$$

Interferometer thermal drift uncertainty:

$$u_{\text{TD}}^2(d) = C_T^2 u^2(\Delta T) + \Delta T^2 u^2(C_T)$$

Equation Summary

Interferometer deadpath error:

$$d_{\text{DP}} = \frac{z_{\text{DP}} \Delta \lambda}{\lambda_i} - \frac{z_{\text{DP}} \Delta n}{n_f}$$

Deadpath uncertainty:

$$u_{\text{DP}}^2(d) = \Delta z_{\text{DP}}^2 \left(\frac{u(\Delta n)}{n} \right)^2 + \Delta z_{\text{DP}}^2 \left(\frac{u(\Delta \lambda)}{\lambda} \right)^2$$

Periodic error uncertainty:

$$u_{\text{PE}}^2(d) = u^2(A_1) + u^2(A_2) \cong (0.71A_1)^2 + (0.71A_2)^2$$

Periodic error uncertainty estimate from amplitude coefficients:

$$u_{\text{PE}}^2(d) \cong (17.7\gamma_1)^2 + (13.1\gamma_2)^2$$

Surface figure uncertainty:

$$u_{\text{SF}}(d) = u(d_{\text{SF}})$$

Data age error:

$$d_{\text{DA}} = \tau_{\text{DA}} \nu$$

Data age uncertainty:

$$u_{\text{DA}}(z) = u(\tau_{\text{DA}}) \nu$$

Equation Summary

Trigonometric product identity:

$$2 \cos A \cos B = \cos (A + B) + \cos (A - B)$$

Euler identities:

$$e^{i\theta} = \cos(\theta) + i \sin(\theta) \quad e^{-i\theta} = \cos(\theta) - i \sin(\theta)$$

$$\cos(\theta) = \frac{e^{i\theta} + e^{-i\theta}}{2} \quad \sin(\theta) = \frac{e^{i\theta} - e^{-i\theta}}{2i}$$

Taylor series expansion:

$$\cos \theta = 1 - \frac{\theta^2}{2!} + \frac{\theta^4}{4!} \dots \quad \sin \theta = \theta - \frac{\theta^3}{3!} + \frac{\theta^5}{5!} \dots$$

Jones matrix notations:

Electric field vector, general form:

$$\mathbf{E} = \begin{bmatrix} E_{01} e^{i(\omega_1 t \pm \varphi_1)} \tilde{x}_i \\ E_{02} e^{i(\omega_2 t \pm \varphi_2)} \tilde{y}_i \end{bmatrix}$$

Ideal polarizer at horizontal (hor), vertical (vert), ± 45 deg (45), and arbitrary angle (θ):

$$\mathbf{J}_{\text{pol,hor}} = \begin{bmatrix} 1 & 0 \\ 0 & 0 \end{bmatrix} \quad \mathbf{J}_{\text{pol,vert}} = \begin{bmatrix} 0 & 0 \\ 0 & 1 \end{bmatrix} \quad \mathbf{J}_{\text{pol},\pm 45} = \frac{1}{2} \begin{bmatrix} 1 & \pm 1 \\ \pm 1 & 1 \end{bmatrix}$$

$$\mathbf{J}_{\text{pol},\theta} = \mathbf{R}(-\theta) \begin{bmatrix} 1 & 0 \\ 0 & 0 \end{bmatrix} \mathbf{R}(\theta) = \begin{bmatrix} \cos^2 \theta & \cos \theta \sin \theta \\ \cos \theta \sin \theta & \cos^2 \theta \end{bmatrix}$$

Quarter waveplate with fast axis alignment:

$$\mathbf{J}_{\text{Q,hor}} = e^{i\pi/4} \begin{bmatrix} 1 & 0 \\ 0 & i \end{bmatrix} \quad \mathbf{J}_{\text{Q,vert}} = e^{i\pi/4} \begin{bmatrix} 1 & 0 \\ 0 & -i \end{bmatrix}$$

$$\mathbf{J}_{\text{Q},\pm 45} = \frac{\sqrt{2}}{2} \begin{bmatrix} 1 & \pm i \\ \pm i & 1 \end{bmatrix} \quad \mathbf{J}_{\text{Q},\theta} = \mathbf{R}(-\theta) \begin{bmatrix} 1 & 0 \\ 0 & -i \end{bmatrix} \mathbf{R}(\theta)$$

Equation Summary

Half waveplate with respect to the horizontal axis:

$$\mathbf{J}_{H,\theta} = \begin{bmatrix} \cos 2\theta & \sin 2\theta \\ \sin 2\theta & -\cos 2\theta \end{bmatrix}$$

General rotation matrix for angle θ :

$$\mathbf{R}(\theta) = \begin{bmatrix} \cos \theta & \sin \theta \\ -\sin \theta & \cos \theta \end{bmatrix}$$

Bibliography

ANSI/NCSL Z540.2, *U.S. Guide to Expression of Uncertainty in Measurement*, R2007 (1997).

Badami, V. G., “Investigation and Compensation of Periodic Nonlinearities in Heterodyne Interferometry,” Ph.D. Thesis, University of North Carolina at Charlotte (1999).

Badami, V. G., “Uncertainty in displacement measuring interferometry (DMI),” American Society for Precision Engineering Tutorial, San Diego (2012).

Badami, V. G. and de Groot, P. J., “Displacement Measuring Interferometry,” in *Handbook of Optical Dimensional Metrology*, Harding, K., Ed., CRC Press, Boca Raton, FL (2013).

Badami, V. G. and Patterson, S. R., “A frequency domain method for the measurement of nonlinearity in heterodyne interferometry,” *Precision Engineering* **24**, 41–49 (2000).

Baer, T., Kowalski, F. V., and Hall, J. L., “Frequency stabilization of a 0.633- μ m He-Ne longitudinal Zeeman laser,” *Applied Optics* **19**, 3173–3177 (1980).

Balhorn, R., Kunzmann, H., and Lebowsky, F., “Frequency stabilization of internal-mirror helium-neon lasers,” *Applied Optics* **11**, 742–744 (1972).

Birch, K. P. and Downs, M. J., “Correction to the updated Edlén equation for the refractive index of air,” *Metrologia* **31**, 315–316 (1994).

Birch, K. P. and Downs, M. J., “An updated Edlén equation for the refractive index of air,” *Metrologia* **30**, 155–162 (1993).

Bobroff, N., “Recent advances in displacement measuring interferometry,” *Measurement Science and Technology* **4**, 907–926 (1993).

Bryan, J., “The Abbé principle revisited: an updated interpretation,” *Precision Engineering* **1**, 129–132 (1979).

Bibliography

Ciddor, P. E., “Refractive index of air: new equations for the visible and near infrared,” *Applied Optics* **35**, 1566–1573 (1996).

De Freitas, J. M. and Player, M. A., “Importance of rotational beam alignment in the generation of second harmonic errors in laser heterodyne interferometry,” *Measurement Science and Technology* **4**, 1173–1176 (1993).

De Freitas, J. M. and Player, M. A., “Polarization effects in heterodyne interferometry,” *Journal of Modern Optics* **42**, 1875–1899 (1995).

Demarest, F. C., “High-resolution, high-speed, low data age uncertainty, heterodyne displacement measuring interferometer electronics,” *Measurement Science and Technology* **9**, 1024–1030 (1998).

Edlén, B., “The refractive index of air,” *Metrologia* **2**, 71–80 (1996).

Ellis, J. D., “Optical Metrology Techniques for Dimensional Stability Measurements,” Ph.D. Thesis, Delft University of Technology, Netherlands, 2010.

Estler, W. T., “High-accuracy displacement interferometry in air,” *Applied Optics* **24**, 808–815 (1985).

Evans, C., *Precision Engineering: An Evolutionary View* Cranfield Press, Bedfordshire, UK (1989).

Evans, C., Holmes, M., Demarest, F., Newton, D., and Stein, A., “Metrology and calibration of a long travel stage,” *CIRP Annals - Manufacturing Technology* **54**, 495–498 (2005).

Gerrard, A., and Burch, J. M., *Introduction to Matrix Methods in Optics*, Dover, New York (1975).

Haitjema, H., “Achieving traceability and sub-nanometer uncertainty using interferometric techniques,” *Measurement Science and Technology* **19**, 084002 (2008).

Bibliography

Harding, K., Ed., *Handbook of Optical Dimensional Metrology*, CRC Press, Boca Raton, FL (2013).

Haycocks, J. and Jackson, K., “Traceable calibration of transfer standard for scanning probe microscopy,” *Precision Engineering* **29**, 168–175 (2005).

Hecht, E., *Optics*, Addison-Wesley, Boston (2002).

Holmes, M. L., “Analysis and Design of a Long Range Scanning Stage,” Ph.D. Thesis, University of North Carolina at Charlotte (1998).

Horowitz, P. and Hill, W., *The Art of Electronics*, Cambridge University Press, Cambridge, UK (1989).

Heydamenn, P. L. M., “Determination and correction of quadrature fringe measurement errors in interferometers,” *Applied Optics* **20**, 3382–3384 (1981).

ISO/IEC Guide 99:2007, *International Vocabulary Metrology – Basic and General Concepts and Associated Terms* (2007).

JCGM 100:2008, *Evaluation of Measurement Data – Guide to the Expression of Uncertainty in Measurement* (2008).

Jones, R. C., “A new calculus for the treatment of optical systems: Part I – Description and discussion of the calculus,” *Journal of the Optical Society of America* **31**, 488–493 (1941).

Jones, R. C., “A new calculus for the treatment of optical systems: Part II – Proof of three general equivalence theorems,” *Journal of the Optical Society of America* **31**, 493–495 (1941).

Leach, R., Haycocks, J., Jackson, K., Lewis, A., Oldfield, S., and Yacoot, A., “Advances in traceable nanometrology at the National Physical Laboratory,” *Nanotechnology* **20**, R1–R6 (2001).

Leach, R. K., *Fundamental Principles of Engineering Nanometrology*, Elsevier, London (2010).

Bibliography

Michelson, A. A., “The relative motion of the Earth and ether,” *American Journal of Science* **s4-3**, 475–478 (1897).

Morris, R. H., Ferguson, J. B., and Warniak, J. S., “Frequency stabilization of internal mirror He-Ne lasers in a transverse magnetic field,” *Applied Optics* **14**, 2808–2808 (1975).

Pedrotti, F. L. and Pedrotti, L. S., *Introduction to Optics*, Prentice Hall, Upper Saddle River, NJ (1993).

Quenelle, R. C., “Nonlinearity in interferometer measurements,” *Hewlett Packard Journal* **34**, 10 (1983).

Quinn, T. J., “Practical realization of the definition of the metre, including recommended radiations of other optical frequency standards,” *Metrologia* **30**, 103–541 (2003).

Schmitz, T. L., Evans, C. J., Davies, A., and Estler, W. T., “Displacement uncertainty in interferometric radius measurements,” *CIRP Annals-Manufacturing Technology* **51**, 451–454 (2002).

Shaddock, D., Ware, B., Halverson, P. G., Spero, R. E., and Klipstein, B., “Overview of the LISA phasemeter,” *AIP Conf. Proc.* **873**, 654–660 (2006).

Sommargren, G., “A new laser measurement system for precision metrology,” *Precision Engineering* **9**, 179–184 (1987).

Stone, J., Phillips, S. D., and Mandolfo, G. A., “Corrections for wavelength variations in precision interferometric displacement measurements” *Journal of Research of the National Institute of Standards and Technology* **101**, 671–674 (1996).

Wu, C., Lawall, J., and Deslattes, R. D., “Heterodyne interferometer with subatomic periodic nonlinearity,” *Applied Optics* **38**, 4089–4094 (1999).

Zygo Corp., “A primer on displacement measuring interferometers,” Zygo Corp. Technical Document (1999).

Index

- 2-DOF tip-tilt mount, 73
- Abbé errors, 63–64
- Abbé principle, 99
- Abbé uncertainty, 113
- absolute position, 1
- absorption, 17
- acceleration limitation, 40
- acousto-optic modulator, 45
- air refractive index, 95
- alignment and setup
 - sources, 92
- alignment technique, 70
- altitude effects, 107
- amplitude demodulation, 27
- amplitude sensitivities, 87
- angle interferometer, 57
- angle optics, 57
- antireflection, 17
- apertures, 66
- azimuthal, 6

- back beam, 44
- balanced interferometers, 101
- bandwidth sources, 92
- beam leakage, 84
- beam walkoff, 38
- beam-steering optics, 62
- Bragg angle, 45
- breadboard hole grid, 70
- beamsplitter alignment, 74
- bubble level, 66
- CCD camera, 66
- circular polarization, 7
- coaxial differential
 - interferometer, 56
- coherence length, 19
- column reference
 - interferometers, 55
- combined standard
 - uncertainty, 115
- combined uncertainty, 91
- commercial
 - interferometers, 67
- complex notation, 8
- complex polarization, 7
- confidence interval, 90
- constant velocity motion, 88
- constructive interference, 9
- cosine error, 80–81, 96–97, 112
- coverage factor, 91
- crosstalk, 64
- cube corner target, 96
- cyclic error, 103

- data age error, 105
- data age uncertainty, 105
- DC-level baseline, 34
- deadpath error, 102
- deadpath uncertainty, 102, 113
- degree of freedom, 2
- destructive interference, 9
- detected irradiance, 10
- detection bandwidth, 48
- differential
 - interferometers, 55
- digital processor, 46
- digital signal processors, 40

Index

- direct spectral analysis, 87
- directional sensitivity, 27, 32
- discrete Fourier
 - transform, 52
- displacement measurement
 - model, 106
- displacement measuring
 - interferometers, 1
- displacement-dependent
 - sources, 92
- DMI measurement model, 93
- Doppler shift, 27, 34, 39
- Doppler velocities, 39
- double-pass configuration, 35
- downshifts, 45
- dynamic example, 105
- dynamic range, 40

- Edlén equation, 95
- electric field vector, 5
- electromagnetic radiation, 4
- electronic phase
 - interpolation, 53
- environmental
 - fluctuations, 59
- environmental sources, 92
- equation-based
 - compensation, 107
- error budget, 108, 110
- error corrections, 106
- error mapping, 104
- Euler's formula, 8
- expanded uncertainty, 91
- expected values, 93

- fast axis, 15
- field-programmable gate
 - arrays, 40

- first-order errors, 103
- first-order periodic error, 84
- fly height, 69
- fold prism, 14
- Fourier spectrum, 32
- free spectral range, 44
- frequency band, 48
- frequency mixing, 36
- frequency stability, 41
- fringe contrast, 11–12, 23
- fringe interpolation, 40
- fringe order, 88
- fringe visibility, 19
- fringes, 18
- full-width at half-
 - maximum, 19
- functional point, 63–64

- Gaussian, 90
- general form, 6
- ghost reflections, 17, 71

- half waveplates, 16
- half-waveplate alignment, 76
- handedness, 16
- height reference, 69
- HeNe gain spectrum, 41
- heterodyne, 22
- heterodyne frequency, 34
- heterodyne frequency
 - generation, 45
- heterodyne
 - interferometers, 30, 31
- Heydemann correction, 82
- homodyne, 22
- homodyne interferometer, 23

Index

- homodyne laser encoders, 29
- humidity, 95
- in-line beam steering, 79
- input estimates, 89
- interference, 1, 8, 9
- interference detection, 46
- interference term, 10–11
- interferometer deadpath, 102
- interferometer fold
 - constant, 21
- interferometer thermal drift, 101
- interferometry systems, 22
- intermediate frequency, 52
- iodine-stabilized laser, 3
- irises, 66
- irradiance, 10
- Jones matrices, 6
- laser mode, 44
- laser source, 41
- lateral offset, 71
- law of propagation of
 - uncertainty, 91, 111
- leakage beams, 85
- leakage interference, 86
- least significant bit, 114
- left-hand circular, 7
- Lissajous figure, 82
- lock-in detection, 51
- long coherence, 18
- Malus' law, 15
- measurand, 89
- measurement arm, 1, 20
- measurement model, 89, 93, 110
- meter, 3
- Michelson
 - interferometers, 18
- mirror alignment, 81
- mirror mounts, 72
- multiaxis systems, 33, 62
- multi-DOF
 - interferometers, 63
- negative Doppler shift, 39
- NIST Shop Floor, 59
- nonvacuum, 4
- offset mirror, 72
- optical breadboards, 68
- optical feedback
 - destabilization, 3
- optical path, 1
- optical path difference, 18, 20
- optical path length, 101
- optical power, 42
- optical power efficiency, 25
- optical reference, 31, 32
- other uncertainties, 114
- output estimate, 89
- parameters, 110
- periodic error, 36, 83, 85–86, 103
- periodic error uncertainty, 103
- phase change uncertainty, 98
- phase changes, 20
- phase measurements, 46

Index

- phase meter electronics, 40
- phase meter uncertainty, 114
- phase quadrature, 27
- phase quadrature
 - measurement, 28, 49
- phase-locked loop, 51
- phase-sensitive detector, 29
- phasor diagram, 8
- photoconductive, 47
- photodetector, 66
- photovoltaic, 47
- pitch, 2
- plane mirror
 - interferometers, 37, 97
- plane mirror target, 35, 100
- plane waves, 10
- point alignment, 67–68
- polar coordinates, 8
- polarimeter, 74
- polarization diagram, 6
- polarization flipping, 78
- polarization manipulation, 28
- polarization overlap, 11
- polarization scrambling, 70
- polarization state, 5, 6
- polarization-sensitive
 - homodyne interferometer, 26
- polarizer alignment, 75
- polarizers, 15, 66
- polarizing beamsplitters, 15, 74
- position-sensitive detector, 66
- positive Doppler shift, 39
- power meter, 66
- p-polarized light, 15, 26
- practical standard, 3
- pressure, 95
- probability distribution, 90
- quad-pass interferometer, 54
- quadrature detection, 82
- quantifying periodic error, 87
- quarter waveplates, 16, 77
- quasi-static example, 105
- reference arm, 1, 20
- refractive index, 4
- refractive index tracker, 61
- refractive index
 - uncertainty, 95
- refractive index variation, 112
- refractometry, 59, 107
- relative position, 1
- retroreflector, 14
- retroreflector homodyne interferometer, 24
- retroreflector target, 100
- right-hand circular, 7
- Risley prisms, 55, 79
- roll, 2
- scatter, 17
- second-order errors, 103
- second-order periodic error, 84
- sensitivity coefficients, 91

Index

- shear plates, 14, 79
- shot noise, 42
- signal preconditioning, 46
- signal strengths, 11
- silicon photodiodes, 47
- single beam, 6
- single-mode lasers, 42
- sinusoidal, 90
- Snell's law, 14, 79
- source mixing, 83
- spatial Fourier analysis, 88
- spatial sampling
 - frequency, 88
- spectral linewidth, 19
- speed of light, 4
- split frequency, 22
- s-polarized light, 15, 26
- stage displacement, 109
- standard uncertainty, 89
- steering mirror, 78
- straightness, 2, 24
- straightness errors, 2
- straightness
 - interferometer, 58
- straightness optics, 58
- stress birefringence, 68
- superposition principle, 8
- surface figure, 104
- surface figure error, 104, 114
- surface figure uncertainty, 104

- temperature, 95
- temporal coherence, 19
- thermal drift error, 101
- thermal drift uncertainty, 101
- time interval analysis, 46, 50
- tip-tilt-Z system, 65
- tolerances, 25
- traceability, 3
- traceability chain, 3
- transimpedance amplifier, 47
- triangular, 90
- two-mode intensity-balanced lasers, 44
- Twyman–Green
 - interferometers, 18
- Type-A methods, 89
- Type-B methods, 89
- Type-B uncertainties, 90

- uncertainty estimate, 110
- uncorrelated
 - uncertainties, 91
- unequal plane mirror
 - interferometer, 35
- uniform, 90
- unwrapping, 21
- upshifts, 45

- vacuum, 4
- vacuum permeability, 4
- vacuum permittivity, 4
- vacuum wavelength, 4, 94
- vector alignment, 67–68

- wavefront distortion, 68
- wavelength tracking, 60, 107

Index

- | | |
|--------------------------------|-----------------------------------|
| wavelength uncertainty,
111 | yaw, 2 |
| wedged optics, 14 | Zeeman effect, 43 |
| white light, 19 | Zeeman stabilized laser,
42–43 |
| Wollaston prism, 58 | zero-crossing detector, 50 |
| X-Y-theta systems, 64 | |



Jonathan D. Ellis is currently an Assistant Professor at the University of Rochester with a joint appointment in the Department of Mechanical Engineering and the Institute of Optics. He obtained his doctorate from the Delft University of Technology in the Netherlands, and M.S. and B.S. degrees from the University of North Carolina at Charlotte, all in mechanical engineering. He actively participates in SPIE, the Optical Society of America

(OSA), and the American Society for Precision Engineering (ASPE). He currently serves as Director-at-Large and Treasurer for ASPE.

Professor Ellis' research interests are in precision engineering, interferometry, optical metrology, instrumentation for primary standards level metrology, freeform optics fabrication and metrology, and precision scanning systems.

Displacement Measuring Interferometry

Jonathan D. Ellis

This Field Guide provides a practical treatment of the fundamental theory of displacement measuring interferometry, with examples of interferometry systems and uses. It outlines alignment techniques for optical components, signal processing systems for phase measurements, and laser stabilization for homodyne and heterodyne sources. The concept of displacement measurement uncertainty is discussed with a practical example of calculating uncertainty budgets. For practicing engineers, this Field Guide will serve as a refresher manual for error sources and uncertainty budgets. For researchers, it will bring new insight to the way in which this technology can be useful in their field. For new engineers, researchers, and students, it will also serve as an introduction into basic alignment techniques for breadboard-based optical systems.

SPIE Field Guides

The aim of each *SPIE Field Guide* is to distill a major field of optical science or technology into a handy desk or briefcase reference that provides basic, essential information about optical principles, techniques, or phenomena.

Written for you—the practicing engineer or scientist—each field guide includes the key definitions, equations, illustrations, application examples, design considerations, methods, and tips that you need in the lab and in the field.

John E. Greivenkamp
Series Editor

SPIE.

P.O. Box 10
Bellingham, WA 98227-0010
ISBN: 9780819497994
SPIE Vol. No.: FG30

ISBN 978-0-8194-9799-4



9 780819 497994

www.spie.org/press/fieldguides